Magnetic Field Assisted Abrasive Polishing

by

Azeem Singh Kahlon

A thesis
presented to the University of Waterloo
in fulfillment of the
thesis requirement for the degree of
Master of Applied Science
in
Mechanical and Mechatronics Engineering

Waterloo, Ontario, Canada, 2021

Author's Declaration

I hereby declare that I am the sole author of this thesis. This is a true copy of the thesis, including any required final revisions, as accepted by my examiners.
I understand that my thesis may be made electronically available to the public.

Abstract

Surface roughness of both machined and additively manufactured components is a critical characteristic that ensures both functional requirements and efficient performance in many high-precision applications requiring precise surface morphologies such as those used in the aerospace and medical industry. Due to uncertainties and the complex nonlinear nature of hundreds of manufacturing process parameters ranging from melt pool temperature to velocity of the cutting tool, the surface roughness of the manufactured product is not controllable and hence requires post-processing.

In this study, a system to remove material and reduce the surface roughness of physically hard-to-reach external and internal surfaces of a non-magnetic workpieces is designed, developed and tested for efficacy and flexibility. Unlike conventional Magnetic Abrasive Finishing (MAF), this technique does not involve any moving parts to impart rotating motion to either the electromagnet or the workpiece. The system works on the principle of generating Rotating Magnetic Fields (RMF) to manipulate the motion of Magnetic Abrasive Particles (MAPs) on the surface of a workpiece for material removal in the form of micro and nano scale chips. An optimal configuration of stationary electromagnets is activated using an FPGA control unit coupled with digital servomotor drives and a DC power supply to generate the required magnetic flux density in the working region. The magnetic field gradient can be significantly magnified by selecting an appropriate core tip shape from a selection of eleven different tip shapes resulting in reduced leakage of magnetic flux. The modular nature of the system allows the operator to change the core tip shapes, the orientation of coils, current, amplitude, frequency, and phase difference at any instant. Moreover, the entire setup is mounted on four caster wheels that can be easily moved and safely secured at any location.

Finite element parametric optimization in Ansys Maxwell is used to design and fabricate a novel tapered electromagnet geometry optimized for maximum gradient of magnetic field on both axial and off-axial locations. The performance of the optimized geometry is validated via both analytical and experimental results with less than an average error of 10%. The novel electromagnet shape is designed to reduce the distance between adjacent coils and maintain a uniform distribution of magnetic field in the workspace.

To quantify the effectiveness of this technique, different optimal electromagnet configurations are implemented on aluminum specimens subjected to six different abrasives and tested under a Laser scanning confocal microscope. The average surface roughness (Ra) is improved from 93% to 36% depending on the input process parameters, namely current, frequency and cycle time.

Acknowledgements

This dissertation would not have been possible without the guidance and the help of several individuals who in one way or another contributed and extended their valuable assistance in the preparation and completion of this study. I would like to express my gratitude to the people in my life who made this academic journey a rich and fulfilling life experience. I would like to thank my supervisor, Prof. Behrad Khamesee, for his guidance, unfailing support, and trust throughout my master's study. Under his mentorship, I had the opportunity to truly advance my engineering design skills and scientific knowledge in electromechanical design. It has been an honor to be his student. I am indebted to him for his generous contributions of time, ideas, resources, and encouragement to make my research experience productive and stimulating.

I am very grateful to Mipox Corporation for sponsoring this project and motivating me to implement the most innovative solutions possible. I would also like to extend my deepest gratitude to Dr. Saeed Sepasy (Head of Innovation and Technology at Mipox Corporation) and Saori Nakagawa for their valuable inputs and continuous experimental feedback. I am very grateful to my thesis readers, Dr. Mihaela Vlasea and Dr. Mustafa Yavuz for taking the time to read my thesis and providing their valuable feedback.

I would like to thank all my colleagues at the Maglev Microrobotics Laboratory, I can never forget so many great memories and pleasant conversations I had with them - Heba, Pooriya, Saksham, Parichit, Daniel, Chanuphon, Yashesh, Curtis, and Dr. Moslem.

I would also like to acknowledge the financial support provided by the University of Waterloo by awarding me the University of Waterloo Graduate Scholarship, Faculty of Engineering Graduate Scholarship and Graduate Research Studentship.

I owe my gratitude to my parents, Gurinder Singh Kahlon and Virandra Kaur, and to my family Ravinder Kaur, Harjinder Singh, Arshdeep Kaur Bal and Jiffy for instilling my passion for science and engineering and for their support and sacrifice in enabling me to pursue my professional and academic goals. My father who raised me with a love of engineering and supported me in all my pursuits, and my mother whose spiritual and positive outlook towards life has been the guiding compass for me. I owe my special thanks to my friends Jagteshwar, Avnish, Tejasvi, Adit, Achint, Sameer and Neil for their cheerful encouragement throughout my academic years.

I would like to thank my Lord Sri Guru Grant Sahib for providing me with such great opportunities in life and giving me the intelligence and will-power to learn and explore endlessly.

Dedication

To my beloved Parents

Contents

List of Figures

List of Tables

Chapter 1

Introduction

Additive manufacturing is a revolutionary and transformative technology that will be at the forefront of industrial production in the coming future. It facilitates the design of complex geometries such as conformal cooling passages in turbine blades, which are either very expensive or impractical with traditional machining methods (milling, dies etc.). However, due to uncertainties and complex nonlinear nature of hundreds of parameters ranging from melt pool temperature to velocity, the surface roughness of the manufactured product is not controllable and hence requires post-processing. The average surface roughness is critical for applications requiring strict tolerance. Post-processing of additively manufactured components with hands is not an efficient option as it may raise production costs, increase deviations in surface quality and may restrict having different variations in surface roughness [1].

Conventionally available finishing processes such as bonnet polishing, vibration assisted polishing, fluid jet polishing, sandblasting, fine abrasive finishing, laser remelting etc. are some of the techniques used to achieve the desired surface roughness, alter mechanical properties (such as residual stresses) and remove excess material from machined components [2]. However, the time-consuming nature, susceptibility to quasi static errors and high sensitivity to process parameters are some of the key driving factors to initiate the search for alternate and non-conventional finishing techniques. Furthermore, conventional methods are pre-tuned for specific part characteristics and require a process overhaul if the design requirements are modified. This is where non-conventional finishing processes such as Magnetic Abrasive Finishing (MAF) come in picture.

Magnetic Abrasive Finishing (MAF) is a flexible micromachining process designed to alter the surface profile of a part based on the action of magnetic field on ferromagnetic particles by removing thin micro or nano scale layers in the form of fine chips [3]. MAF has already been used to polish various materials and geometries ranging from flat surfaces to complex shapes such as hollow and solid cylindrical tubes [2]. The surface finishing action takes place due to the relative motion between the workpiece and the abrasive mixture. Therefore, one of the most important tasks in designing a MAF setup is controlling the motion of the Magnetic Abrasive Particles (MAPs). The MAPs follow a circular path along the flux lines generated by a Rotating Magnetic Field (RMF). In conventional MAF setups, an RMF is generated by mechanically rotating permanent/electromagnets or the workpiece. Fig. 1.1 illustrates a cross-sectional view of a typical MAF process where a permanent magnet is provided with a continuous rotational feed. This limits the flexibility of the polishing process and portability of the system when variation of surface roughness is required, and complex surface profiles are used. Due to this limiting design constraint MAF is not adept for polishing complex constructs. Another fundamental limitation associated with conventional MAF systems is its applicability to only cylindrical, flat sheet or low curvature surfaces.

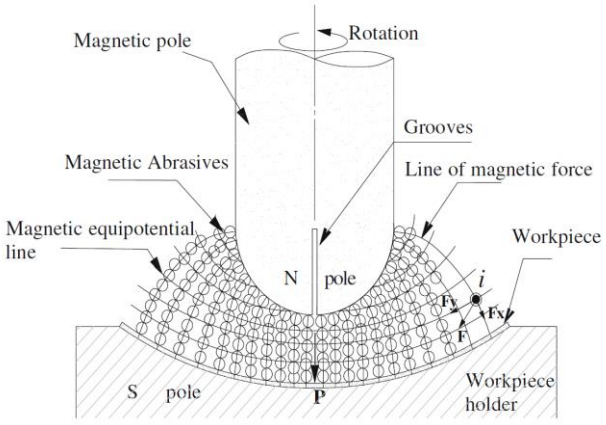

Figure 1.1 Typical Magnetic Abrasive Finishing **[4]**

1.1 Proposed Technique

It is an objective of the present disclosure to obviate or mitigate at least one limitation of conventional Magnetic Abrasive Finishing process. The present disclosure is an apparatus to reduce the surface roughness of a non-magnetic workpiece by facilitating material removal due to the relative motion between the Magnetic Abrasive Particles (MAPs) and the workpiece. The relative motion is a result of the interaction of the MAPs with dynamic magnetic fields generated via a stationary electromagnet array. More particularly, the dynamic magnetic fields are rotating in nature. Under the effect of magnetic field these particles align in the direction of the magnetic flux lines transforming them to semi solid chains [2]. The proposed design would not require any mechanically moving part and would rely on the activation of an array of coils to generate a rotating magnetic field. The abrasive mixture is composed of magnetic particles (iron grits), abrasive particles (like SiC, Al_2O_3) and a lubricant to take care of the heat generated during the process.

To achieve this, a portable apparatus was designed and fabricated by integrating an array of novel tapered electromagnets, controller, and motor drives in a custom-made chassis. Finite element analysis and experimental results confirmed the optimized coil's magnetic performance. An open loop real-time control model was developed to manipulate the magnitude and RPM of the rotating magnetic fields.

In a first aspect, the present disclosure provides a method of generating a Rotating Magnetic Field (RMF) using stationary electromagnets. The system comprises of an electromagnet array consisting of an even number of electromagnets arranged in a circular manner. Each electromagnet in the array is energized using current waveforms that can be controlled to alter the magnetic flux density

and RPM of the RMF. In a further embodiment, the MAPs are introduced to the rotating magnetic field. Due to gradient of the magnetic field, the MAPs follow the magnetic flux lines from one electromagnet pole to the adjacent. Fig. 1.2 illustrates a block diagram of the Magnetic Field Assisted Abrasive Polishing Apparatus.

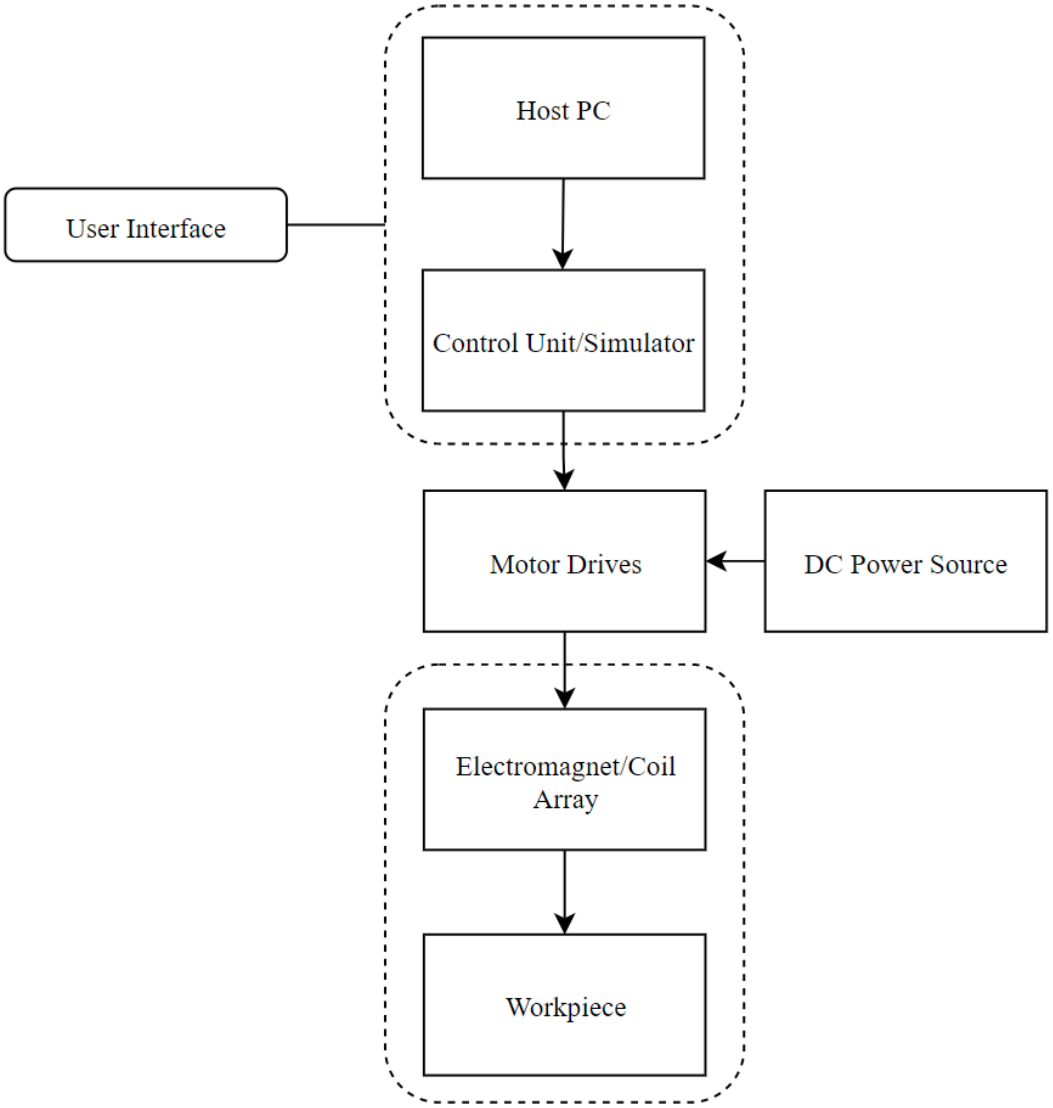

Figure 1.2 Block diagram of Magnetic Field Assisted Abrasive Polishing Appratus

1.2 Thesis Objectives and Outline

The goal of this thesis is to develop a Magnetic Field Assisted Abrasive Polishing Apparatus. To meet this goal the following objectives were undertaken:

- Design and optimization of an electromagnet geometry to maximize the material removal from the surface of the workpiece.
- Fabrication, integration, and calibration of electromechanical and mechatronics sub-systems for a full-scale prototype.
- Development of an open loop control model to vary the cutting force by altering the magnitude of the magnetic flux density and the RPM of the rotating magnetic field.
- Validation of the proposed technique by observing the motion of steel balls under the effect of four and six coils at varying frequencies and amplitudes.
- Evaluation of reduction in surface roughness due to six coils on cylindrical and flat sheet specimens.
- Evaluation of the effect of abrasive particle size on the average reduction in surface roughness of the workpiece.

This thesis includes **6** chapters:

- Chapter **1** states the thesis motivations and goals. It also presents the project organization and contributions.
- Chapter **2** provides the background of Magnetic Abrasive Finishing. A detailed review of the effect of process parameters on surface roughness and material removal rate is presented and the challenges and limitations related to conventional techniques are discussed. A brief section is dedicated to the dominating effect of each process parameter and their respective positive and negative aspects.

- Chapter **3** introduces the analytical and finite element optimization techniques used to design a novel optimized electromagnet and core tip geometries. The chapter also compares the results of both analytical model and Ansys Maxwell.
- Chapter **4** discusses the principle of rotating magnetic fields and a detailed description of sub-systems integrated to achieve the desired pattern of the magnetic fields is presented. This section also explains the control models used to alter the magnetic flux density in the working region.
- Chapter **5** discusses the experiments performed in this study to validate the efficacy of individual subsystems and the system. This chapter also presents the experimental results of the implementation of the polishing technique on aluminum samples.
- Chapter **6** outlines the conclusion of this research by reviewing the summary of the work. The limitations and recommended future work are also discussed.

1.3 Thesis Contributions

- Development of a novel abrasive surface polishing technique by eliminating the requirement of rotating machinery essential to produce rotating magnetic fields in conventional Magnetic Abrasive Finishing.
- Validated the flexibility of the polishing system by implementing a reconfigurable electromagnet array on cylindrical and flat sheet aluminum specimens.
- Development of an open loop control model to control the strength of magnetic flux density and the RPM of the RMF in the test region.
- Design and performance validation of a novel electromagnet/coil design optimized to reduce distance between adjacent coils and generate a uniform magnetic field.

Chapter 2

Literature Review

In this chapter, the literature review for the explored pathways in this thesis is presented. In addition, the foundation of the ideas, discussed in the subsequent chapters, is outlined. The literature review for this dissertation is focused on the effect of process parameters on the average reduction in surface roughness and material removal via conventional magnetic abrasive finishing. The current work is an extension of the preliminary studies on the feasibility of stationary electromagnets for surface polishing performed by Thamir Al-Dulami [5], a former PhD student at the Maglev Microrobotics Laboratory. Dr. Dulami's work implemented a wedge-shaped core tip with four electromagnets on a variety of specimen shapes at low frequencies (<3 Hz). The current system is more configurable, optimized and adaptable in terms on input process parameters and modularity of the coil array with respect to size and shape of the workpiece.

The output of a conventional magnetic abrasive finishing process is a result of more than 5 independent variables, mainly current, grain size of the iron powder, grain size of the abrasive powder, cycle time and RPM of the rotating magnetic field. Kanish et al. [6] used S/N ratio and Analysis of Variance (ANOVA) to study the effect of process parameters on surface finish (Ra) and Material Removal Rate (MRR). The findings indicated that high working voltage (47.11 and 44.09% respectively) and machining gap (28.51% and 32.86%) had the highest effects on both percentage change in Ra and MRR followed by abrasive size and feed rate. Hence it can be concluded that increase in voltage and abrasive size has a positive effect whereas increase in machining gap has a detrimental effect on the average reduction in surface roughness. In a similar study, Zhang et al. [7] employed MAF

for post processing of as printed selected laser melted (SLM) 316L stainless steel, to study the effect of slope angle on surface finish. The study validated a linear relationship between material removal and initial surface roughness.

Wu et al. [2] studied the effect of abrasive size on percentage change in surface roughness and material removal rate. The study found that one way of changing the magnetic force generated by a given magnetic field is by adjusting magnetic particle size in the abrasive mixture. The study also performed a comparative analysis of magnetic abrasives and conventional abrasives and found that magnetic abrasives result in a finer surface finish but a low material removal rate as compared to conventional abrasives, which were able to remove twice the amount of material as compared to magnetic abrasives. Two different sizes of steel grits (G25 and G14) were used in the analysis, and it was found that material removal using G25 (mean diameter 0.7mm) was around 3 times higher than using G14 steel grits (mean diameter 1.4mm). This is because the magnetic force acting on G14 steel grits is higher due to less particles per weight. However, due to its large size G14 steel grits were not able to penetrate narrow valleys.

Guo et al. (2017) [8] established a relationship between material removal rate, surface finish, polishing force and abrasive size using two rolling permanent magnet setups to generate a rotating magnetic field. The study found that after 10 minutes of polishing, particle scattering resulted in a drastic reduction in material removal rate. Four different abrasives were used, Al_2O_3 (5μm and 30μm) and SiC (5μm and 30μm) and it was observed that SiC 30 μm resulted in fast material removal rate due to low polishing force.

Rahul S. Mulik et al. [9] found that brittle fracture and shearing are the dominating mechanisms for the removal of small peaks. The study also compared the effect of bonded and unbonded MAPs and it was found that bonded MAPs dominate the surface finish, whereas unbonded MAPs affect material removal. Moreover, the magnetic force acting on the MAPs is dependent on the magnetic flux intensity and the gradient of the magnetic field followed by the magnetic and volume susceptibility of the particles. The study also revealed that an increase in the diameter of the MAPs and abrasive grain size increases the stock removal and surface roughness, respectively. Fig. 2.1 (c) depicts the forces acting on a single magnetic abrasive particle subjected to a rotating magnetic field due to a radial pole arrangement. Radial pole arrangement is preferred over annular as it is observed that annular pole placement increases the probability of chain breakage (radial chains are produced in annular pole arrangement) due to resistance in the orthogonal direction. The significance of tangential and normal forces is explained in chapter 3.

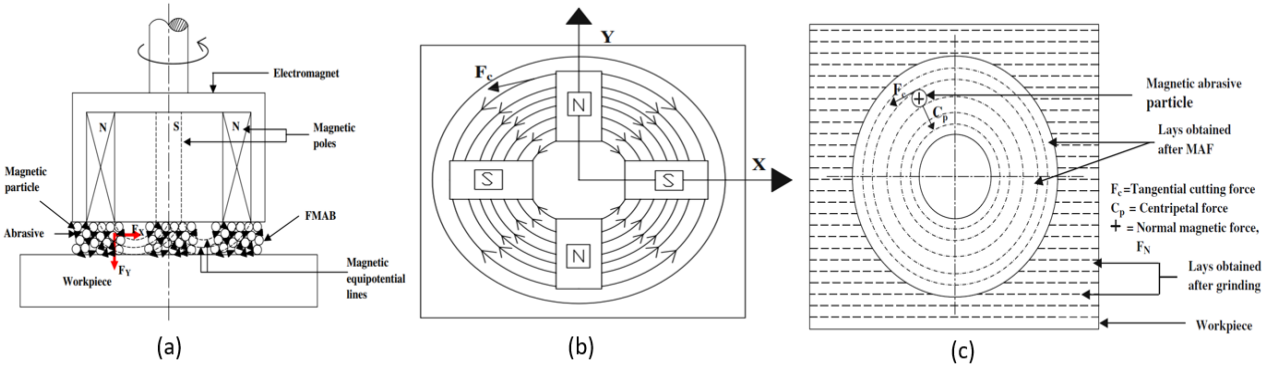

Figure 2.1 (a) Front view, (b) Top view of the schematic of radial electromagnetic pole arrangement, (c) forces acting on a MAP [9]

Dhirendra K. Singh et al. [10] studied the effect of normal and tangential forces on surface finishing and material removal rates. It was found that the tangential forces (f_t) generated due to relative motion between the flexible magnetic abrasive brush and the workpiece, are responsible for the microchipping of the workpiece. However, microchipping will only take place if f_t is greater than the resistance offered by the workpiece against its deformations (a function of hardness, yield strength and ultimate strength). Fig. 2.2 explains the variation of magnetic forces (total and tangential) with the current at varying working and air gaps. Normal forces, on the other hand, are responsible for the penetration/indentation depth of the MAPs into the workpiece. It was also observed that at higher rpm the increase in centrifugal forces and interface temperature reduces the tangential cutting force.

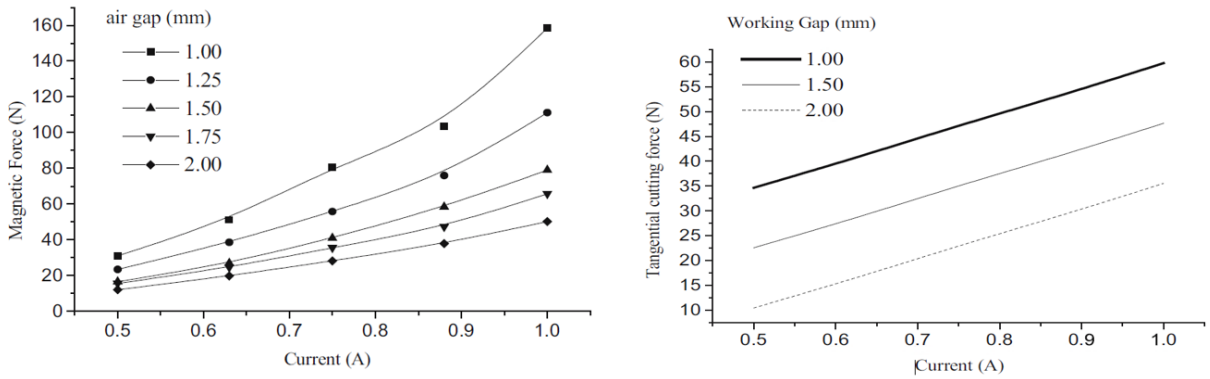

Figure 2.2 (a) Variation of magnetic force with current for different air gaps (b)Variation of tangential cutting force (Fc) with current for different working gaps [10]

ZhengHao Yu et al. [11] studied the surface finish of an elbow pipe using centerline reconstruction. This technique generates a spatial point cloud of the pipe based on the surface contour lines and hence optimizes the parameters for inner surface roughness reduction. Fig. 2.3 illustrates the setup used by ZhengHao Yu et al. for their experiments.

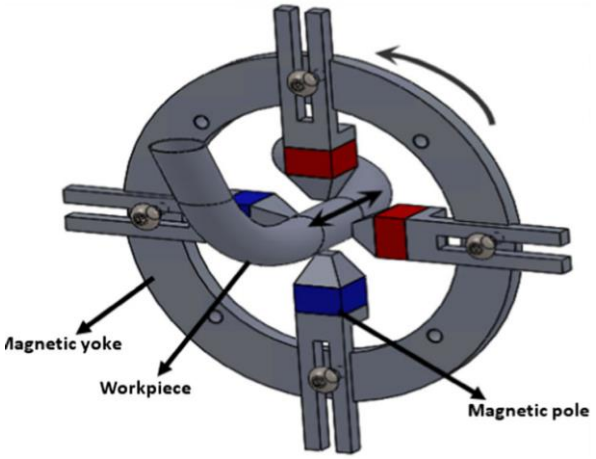

Figure 2.3 MAF setup for an irregular spatial elbow pipe [11]

SHINMURA et al. [12] were one of the first researchers to create a rotating magnetic field for static MAF without using a rotating mechanism. The study compared four types of exciting power source circuits to compare the results of static and rotating MAF setups. It was observed that rotating magnetic fields cause thermal effects in terms of temperature rise in core, yoke, and increased power consumption. The power consumption increases because in the case of rotating fields the tangential force is created by the magnetic field and not by the rotating tool/machine. However, rotating magnetic fields result in higher stock removal as compared to static fields.

Ajay Sidpara and V.K. Jain [13] illustrated the force analysis on a curved surface in an MR fluid-based finishing process. The surface roughness was reduced from 640 nm to 90 nm on mild steel workpieces. It was found that both normal and tangential forces decrease with the increase in the angle of curvature of the workpiece. This is caused due to a decrease in the effective area of contact. Fig. 2.4 illustrates the effect of angle of curvature on the forces exerted by MAPs on the workpiece.

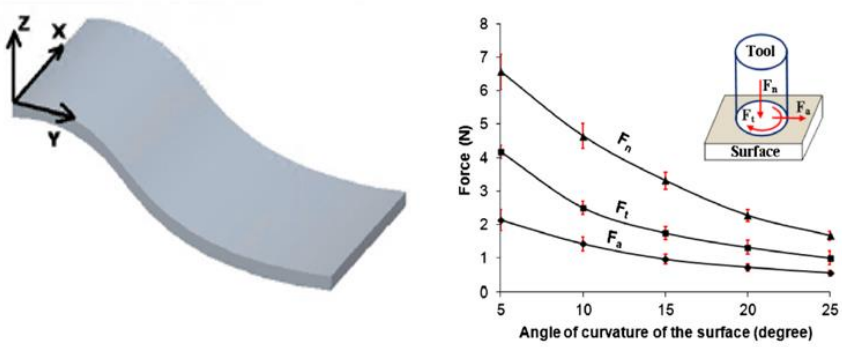

Figure 2.4 (a) Freeform surface subjected to magnetic abrasive finishing (b) Variation of Magnetic force components with angle of curvature of the workpiece surface [13]

Lida Heng et al. [14] implemented rotating magnetic fields to enhance the surface roughness of steel wires from 0.25 µm to 0.02 µm at 800 rpm for 60s. The study used Nd-Fe-B permanent magnets mounted on a plastic chuck for creating an RMF. The research also found that increase in rpm had a direct impact on material removal and final surface roughness.

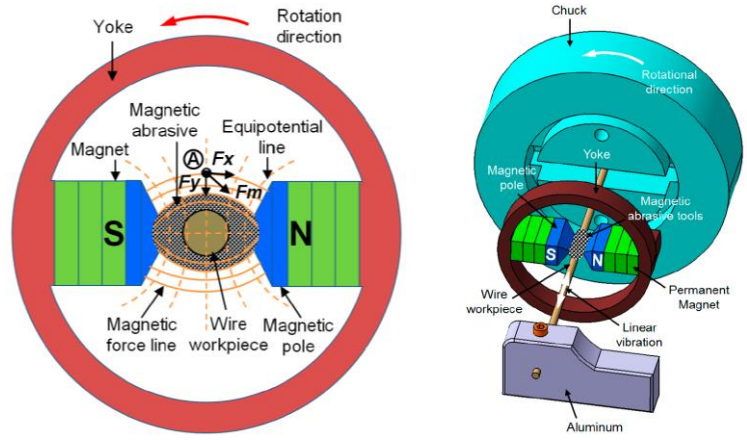

Figure 2.5 2D (a) and 3D (b) schematic of implementation of rotating magnetic fields on steel wire [14]

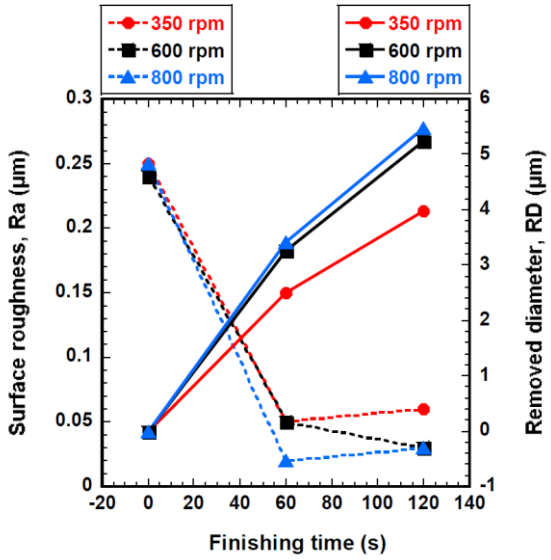

Figure 2.6 Effect of rpm on surface roughness [14]

Vibration assistance is a very common technique to amplify the effect of magnetic fields on the workpiece surface. Yi-Hsun Lee et al. [15] studied the effect of adding vibration to enhance MAF and found that a 2D VAMAF (Vibration Assisted Magnetic Abrasive Finishing) decreased the processing time to achieve similar/lower surface roughness results as compared to a typical MAF process. Fig. 2.7 illustrates the exploded view of the setup developed for implementing 2D VAMAF.

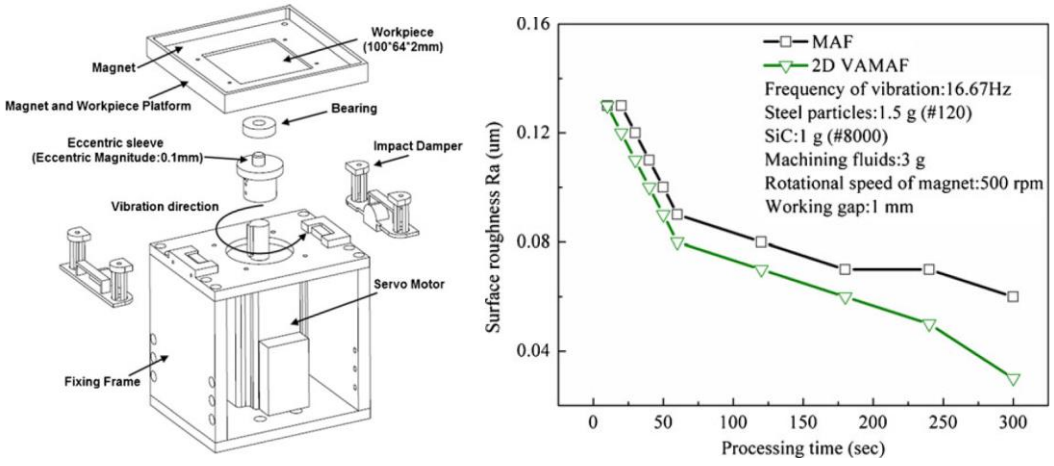

(a) (b)

Figure 2.7 Vibration Assisted MAF setup (a); Comparison of 2D VAMAF and MAF [15]

Due to the non-contact nature of the electromagnets/permanent magnets with the workpiece, MAF can also be implemented to finish internal surfaces such as liquid piping systems. Hitomi Yamaguchi et al [16] used this principle to polish internal surfaces using a stationary pole system. However, the claims were only validated on SUD304 stainless steel disks as the curvature of a tube is considerably negligible compared to the scanning area in microscope (<100 μm^2). In a similar study, Debin Wang et al. [17] implemented a rotating pole instead of a stationary pole to achieve internal material removal. The study also found that wet finishing (distilled water) results in more accurate and efficient surface roughness results as compared to dry finishing of Si_3N_4 tube.

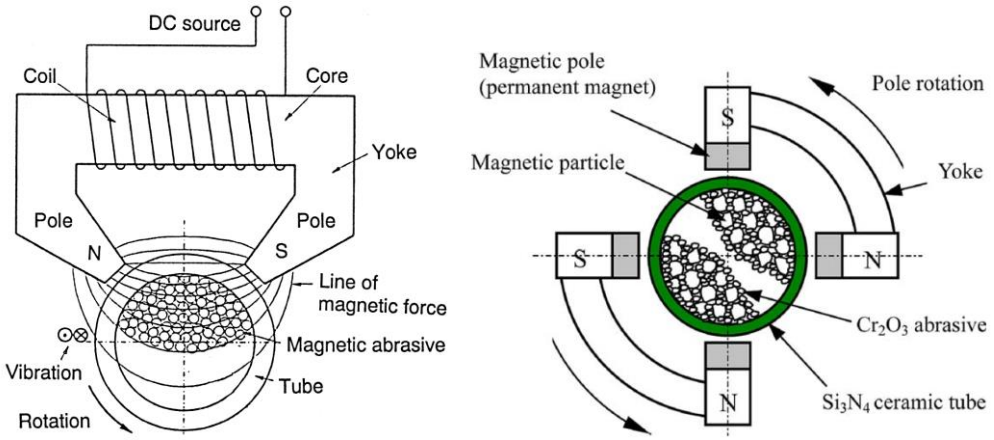

(a) (b)

Figure 2.8 Implementation of stationary (a) [16] and rotating pole (b) [17] system for internal surface finishing

2.1 A Brief Review of Literature Survey

Based on the literature survey, parameters affecting the change in surface roughness and material removal rate are defined below. A range of practically used magnitudes and the dominating effect of these parameters is also discussed. Magnetic flux density and machining gap are found as the most influencing parameters, followed by grain size and cycle time used to achieve the desired surface roughness. Following is a table of parameters with their brief description.

Table 1 Review of Literature Survey

Parameter	Description	Dominating Effect	Range
Working Gap	Gap between the workpiece and the tip of the electromagnet.	Increase in working gap decreases the magnetic field.	1 mm – 2 mm
Feed Rate	Translational motion of the workpiece towards the finishing spot.	-	4-8 mm/min
Rotational speed	Rotating speed of the tool/ milling machine on which the static magnetic field setup is mounted to create a rotational component.	Magnitude of F_x, F_y and F_z increases to an optimum value and then decreases due to increase in centrifugal force resulting in breakage of abrasive chains.	500-2000 RPM
Magnetic Flux density	Intensity of magnetic field lines at the finishing spot.	Increase in magnetic flux density increases the force on the iron grits.	0.2-1 T
Size Ratio	Ratio of size of iron particles to the abrasive particles.	Size Ratio defines the debonding force of the media which in turn limits the	-

		rotational speed to avoid separation.	
Reduction in Ra	These are the surface texture contrasts generated during the manufacturing process.	These values are specific to a material and will change with change in material hardness.	75-95 %
Cycle time	It is the time interval for which the MAF setup is continuously activated via energizing an electromagnetic or a permanent magnet mounted on rotating machinery.	- -	5 – 90 minutes
Angle of Curvature	Angle b/w the normal to the workpiece surface and the rotational axis of the tool.	F_t and F_n decrease with increase in angle of curvature due to reduction in contact area.	0-30 degrees

Chapter 3

Design and Optimization of a Novel Electromagnet Geometry

3.1 Introduction to Analytical Modelling

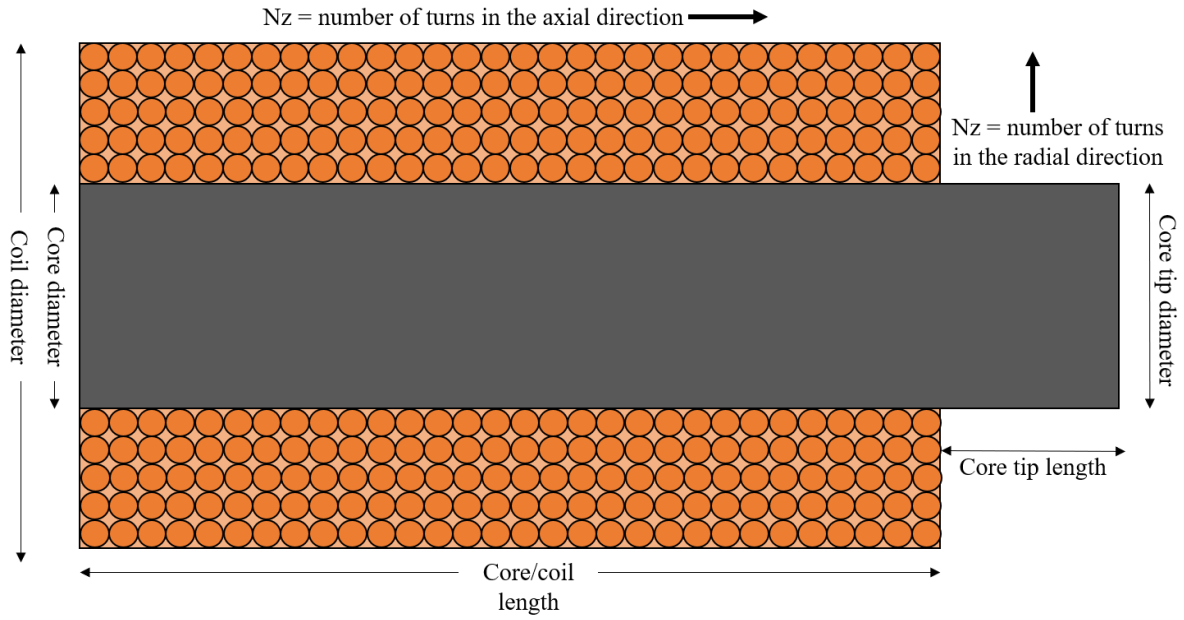

Figure 3.1 Typical coil design parameters

To design an electromagnet/coil, the geometry/dimensions of the coil require optimization. The optimization is based on the force and field components experienced by a mixture of iron and abrasive particles on the surface of a workpiece. The forces generated are a function of many coil parameters:

$$F = f(I, N_z, N_r, r_o, r_i, d_w, l_w, g, B)$$

Where, I is the current in the coil in amperes, B is the magnetic field in Tesla, r_o and r_i are the coil outer and inner radii, respectively, d_w and l_w are the diameter and length of the copper winding wire, N_z and N_r are the number of turns in the axial and radial direction respectively and g is the working gap between the electromagnet and the MAPs. Fig. 3.1 represents a typical coil cross section and Fig. 3.2

provides a 3D view of a cylindrical coil with design parameters that are optimized in this chapter. The project started by referring to literature available on preliminary coil design to maximize the magnetic field on the axis of a cylindrical coil. However, the primary design function of the coil is to maximize the magnetic force at 1-2 mm above the tip of the core. Since, magnetic force is directly proportional to the gradient of the magnetic field, for initial parametric analysis magnetic field was chosen as the cost function. One of the most important aspects of the optimization process is modeling the trend and effect of various dimensional parameters on the desired output of the coil, which in our case is magnetic force and field.

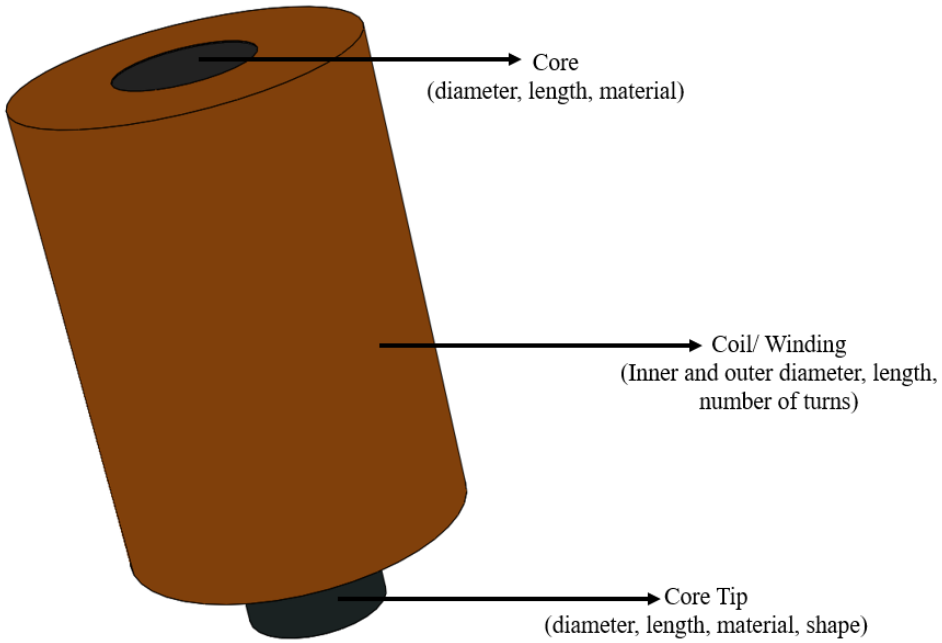

Figure 3.2 Ferromagnetic Coil with design parameters

The optimization process started by creating an analytical model to calculate the magnetic field and analyzing that model in MATLAB for optimization trend analysis. This analytical solution was further modified to calculate the magnetic field at points lying off the axis of the cylindrical coil. However, due to the complex and nonlinear nature of the MAF process the optimization process was later shifted

to finite element analysis performed using Ansys Maxwell. The process of obtaining the analytical model has been explained in the flow chart below. Moreover, it is difficult to analytically solve the field parametric analysis of an iron core coil, hence the analytical model is limited to an air core coil only. However, a comparative analysis has been done using relative permeability of the ferromagnetic core.

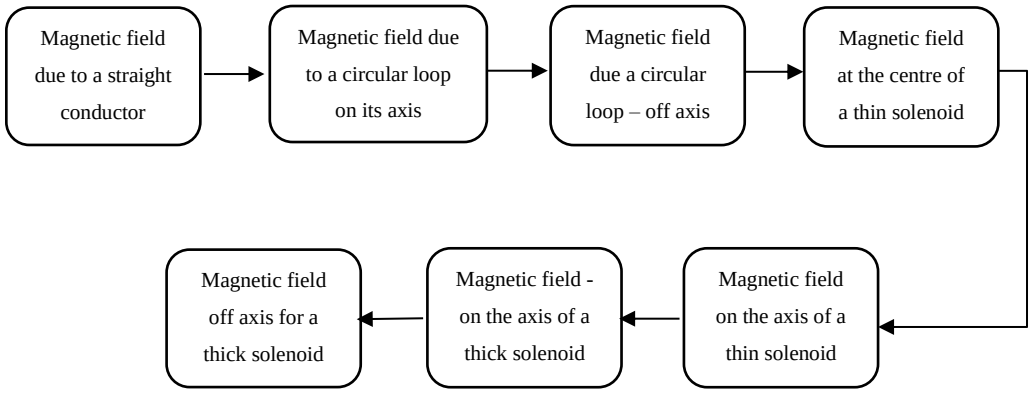

According to ampere's law [18] the magnetic field around a current carrying conductor is proportional to the electric current carried by the source, which can be mathematically represented as:

$$\oint_{closed\ path} \vec{B} \cdot \overrightarrow{dl} = \mu_0 I_{enclosed} \ldots\ldots\ldots\ldots (3.1)$$

Where B is the magnetic field generated due to an infinitely small element of the closed amperian loop dl (not the current element as in Biot Savart's Law) and $I_{enclosed}$ is the total current enclosed by the closed loop. For a closed loop (referred to as the amperian loop) the summation of the length elements of the loop times the magnetic field is equal to permeability of free space times current enclosed in the loop. Ampere's law can be used when the magnetic field along an amperian loop is constant, and the application of this law can be seen in the next sub-sections.

Biot Savart's law [19]: This quantitative relationship defines the magnetic field at a point P due to a constant electric current, which in turn is the summation of the magnetic fields generated by all the small current elements $I\overrightarrow{dl}$.

$$\overrightarrow{dB} = \frac{\mu_0}{4\pi}\frac{I\overrightarrow{dl}\,X\,\hat{r}}{r^2} \text{.....(3.2)}$$

μ_0 = permeability of free space

I = current flowing through the conductor

r = distance of the point of interest from the current element

3.1.1 Magnetic Field on the Axis of a Circular Current Carrying Conductor

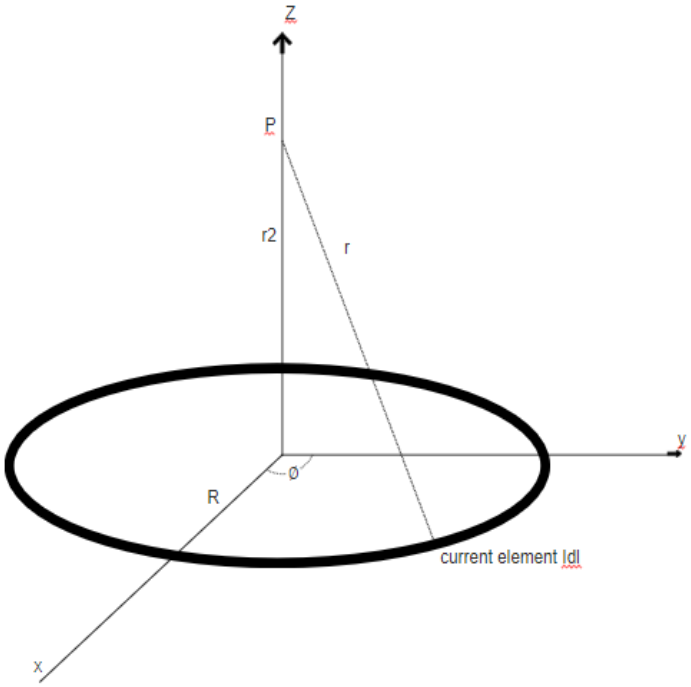

Figure 3.3 Magnetic Field on the Axis of a Circular Current Carrying Conductor

Consider a circular conducting ring carrying a constant current 'I'. From Biot Savart's law, the magnetic field generated by a current element $I\overrightarrow{dl}$ at a distance r from the current element is given by:

$$\overrightarrow{dB} = \frac{u_0}{4\pi}\frac{I\overrightarrow{dl}\,X\hat{r}}{r^2}$$

The total magnetic field at point P will be the summation of magnetic fields due to all such current elements and can be formulated by integrating the above expression:

$$B = \frac{u_0 I}{4\pi}\int \frac{\overrightarrow{dl}\,X\hat{r}}{r^2}$$

Location of the current element can be represented by a vector $\overrightarrow{r_1} = R(cos\,\emptyset\,\hat{\imath} + sin\,\emptyset\hat{\jmath})$

Location of point P, at which field is measured $\vec{r} = \overrightarrow{r_2} - \overrightarrow{r_1} = z\hat{k} - R\sin\emptyset\hat{\jmath} - R\cos\emptyset\hat{\imath}$

where, $|r| = \sqrt{R^2 + z^2} = (R^2 + z^2)^{3/2}$

$$I\overrightarrow{dl} = I\left(d\vec{r}_1/_{d\emptyset}\right)d\emptyset$$

$$\overrightarrow{dl}\,X\,\vec{r} = d\emptyset\,(-Sin\emptyset\hat{\imath} + cos\emptyset\hat{\jmath})\,\mathrm{X}\,\left(z\hat{k} - R\sin\emptyset\hat{\jmath} - R\cos\emptyset\hat{\imath}\right)$$

$$\overrightarrow{dl}\,X\,\vec{r} = Rd\phi(z\cos\emptyset\,\hat{\imath} + z\sin\emptyset\,\hat{\jmath} + R\hat{k})$$

$$\overrightarrow{dB} = \frac{u_0 IR(Rd\phi(z\cos\emptyset\,\hat{\imath} + z\sin\emptyset\,\hat{\jmath} + R\hat{k})}{4\pi(R^2 + z^2)^{3/2}}$$

Due to symmetry of the geometry, radial components (x and y direction) cancel each other, and only axial component (z direction) contribute towards the total magnetic field [20].

$$\int_0^{2\pi} dB = \int_0^{2\pi} \frac{u_0 IR^2(d\phi)}{4\pi(R^2 + z^2)^{3/2}} = B_z = \frac{u_0 IR^2}{2(R^2 + z^2)^{3/2}} \ldots\ldots\ldots\ldots (3.3)$$

The above expression is the resultant magnetic field at a point P on the axis of a circular current carrying conductor.

3.1.2 Magnetic Field Due to a Straight Current Carrying Conductor

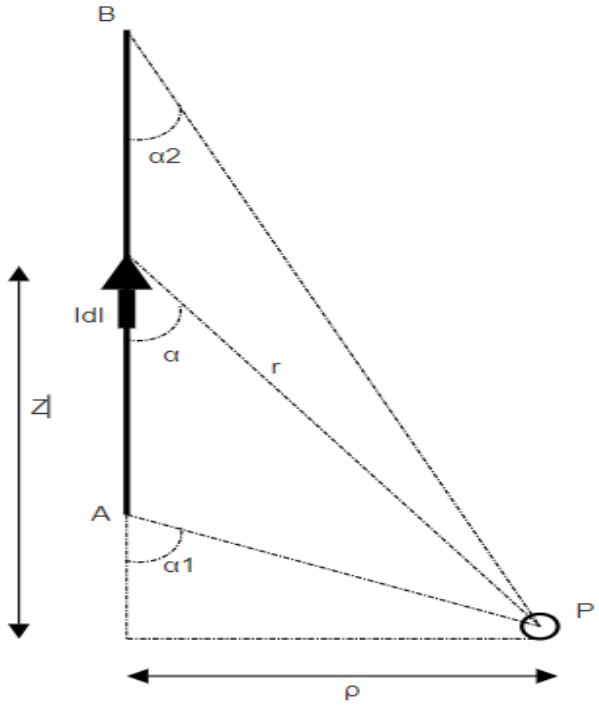

Figure 3.4 Magnetic field due to a straight current carrying conductor

Consider a straight vertical wire carrying a constant current I. From Biot Savart's law, we know that the magnetic field generated by a current element $I\overrightarrow{dl}$ at a distance r is given by:

$$\overrightarrow{dB} = \frac{\mu_0}{4\pi}\frac{I\overrightarrow{dl}\ X\ \vec{r}}{r^3}$$

$$\overrightarrow{dl} = dz\,\hat{k}$$

Location of point P = $\rho\hat{\imath}$; Location of current source = $z\,\hat{k}$

$$\vec{r} = \rho\hat{\imath} - z\,\hat{k}\ ;\ r = \sqrt{\rho^2 + z^2}$$

$$\overrightarrow{dl}\ X\ \vec{r} = \left(dz\,\hat{k}\right) X\left(\rho\hat{\imath} - z\,\hat{k}\right) = \rho\ dz\hat{\jmath}$$

$$\vec{B} = \frac{u_0 I}{4\pi} \int \frac{\rho \, dz \hat{j}}{(\rho^2 + z^2)^{\frac{3}{2}}}$$

Substituting z = $\rho cot\alpha$ and $dz = -\rho cosec^2\alpha$

Hence, the net magnetic field at point P can be formulated as:

$$\vec{B} = \frac{u_0 I}{4\pi} \int_{\alpha_1}^{\alpha_2} \frac{sin\alpha d\alpha}{(\rho^2 + z^2)^{\frac{3}{2}}} \hat{j}$$

$$\vec{B} = \frac{u_0 I}{4\pi\rho} (cos\alpha_2 - cos\alpha_1) \, \hat{k} \ldots\ldots\ldots\ldots (3.4)$$

The above expression is the resultant magnetic field at a point P due to a straight current carrying conductor.

3.1.3 Magnetic Field inside a Thin Solenoid

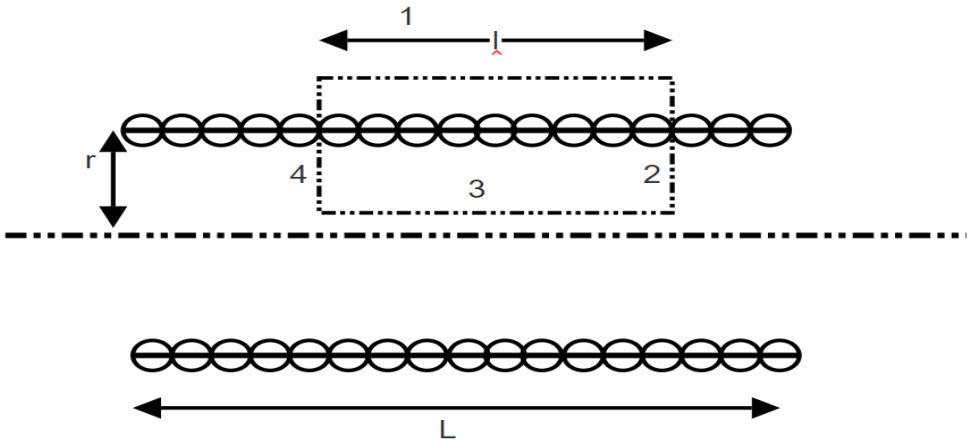

Figure 3.5 Magnetic Field inside a Thin Solenoid

A thin solenoid can be defined as a coil with only one layer of winding in the axial direction. Since, the magnetic field generated by the amperian loop (dotted line) is symmetric, we can use ampere's law to

calculate the magnetic field inside a thin solenoid. The closed loop can be divided into four paths (1, 2, 3 and 4) and only path 3 produces a magnetic field inside the solenoid as the other components are either outside the magnetic flux (magnetic field outside the solenoid is almost zero) lines or perpendicular to the magnetic flux which makes the dot product $\vec{B} \cdot \vec{dl}$ zero.

$$\oint \vec{B}.\vec{dl} = \int_1 \vec{B} \cdot \vec{dl} + \int_2 \vec{B} \cdot \vec{dl} + \int_3 \vec{B} \cdot \vec{dl} + \int_4 \vec{B} \cdot \vec{dl}$$

$$= 0 + 0 + Bl + 0$$

$$Bl = \mu_0 NI$$

$$n = \frac{N}{l} = number\ of\ turns\ per\ unit\ length$$

$$N = total\ number\ of\ turns$$

$$B = \mu_0 nI \quad \ldots\ldots\ldots\ldots (3.5)$$

The above expression is the resultant magnetic field at a point P inside a thin solenoid.

3.1.4 Magnetic Field on the Axis of a Thin Solenoid

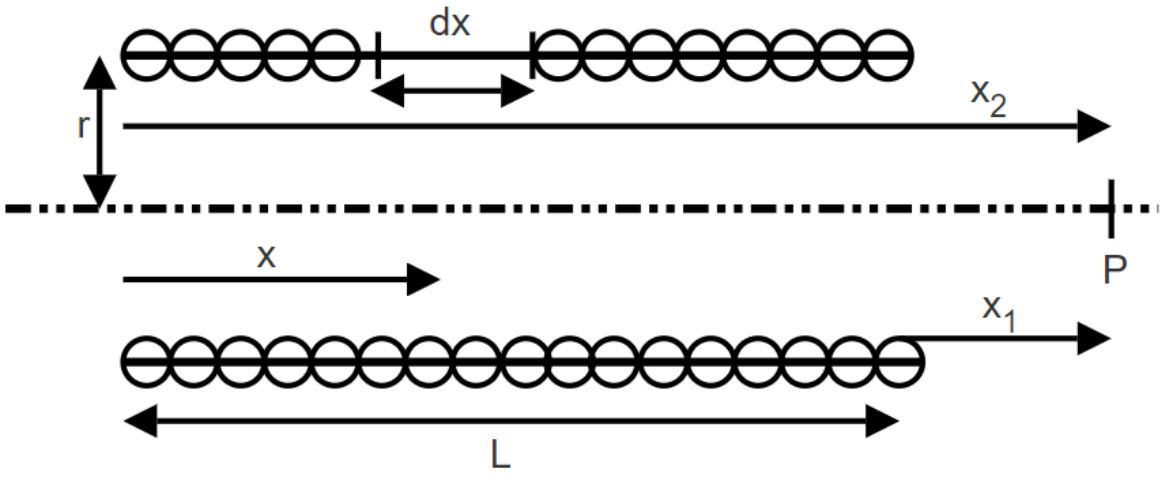

Figure 3.6 Magnetic Field on the Axis of a Thin Solenoid

We have derived the magnetic field due to circular coil of radius 'a' in section 3.1.3 as:

$$B = \frac{u_0 I}{2} \frac{a^2}{(\rho^2 + z^2)^{\frac{3}{2}}}$$

The current density due to a thin solenoid can be denoted by the Greek letter lambda $\lambda = \frac{NI}{l}$

$$dI = \lambda dx \text{ and } dB = \lambda dx$$

$$dB = \frac{u_0}{2} \frac{\lambda a^2 dx}{(a^2 + (L + x_1 - x)^2)^{\frac{3}{2}}}$$

$$B = \frac{u_0 \lambda a^2}{2} \int_0^L \frac{dx}{(a^2 + (L + x_1 - x)^2)^{\frac{3}{2}}}$$

assuming $L + x_1 - x = u, then\ dx = du$

When $x = 0;\ u = L + x_1$

When $x = L;$ u=x_1

$$B = \frac{u_0 \lambda}{2} \int_{x_1}^{L+x_1} \frac{du}{(a^2 + u^2)^{\frac{3}{2}}} = \frac{u_0 NI}{2L} \left[\frac{x_2}{\sqrt{x_2^2 + r^2}} - \frac{x_1}{\sqrt{x_1^2 + r^2}} \right] \ldots\ldots\ldots\ldots (3.6)$$

The above expression is the resultant magnetic field at a point P on the axis of a thin solenoid.

3.1.5 Magnetic Field on the Axis of a Thick Solenoid

A thick solenoid (also known as a multi-layer- multi turn coil) is an inductor having more than one turn in both axial and radial directions. From section 3.1.4, the magnetic field on the axis of a thin solenoid can be calculated by the equation:

$$B = \frac{u_0 NI}{2L}\left[\frac{x_2}{\sqrt{x_2^2 + r^2}} - \frac{x_1}{\sqrt{x_1^2 + r^2}}\right]$$

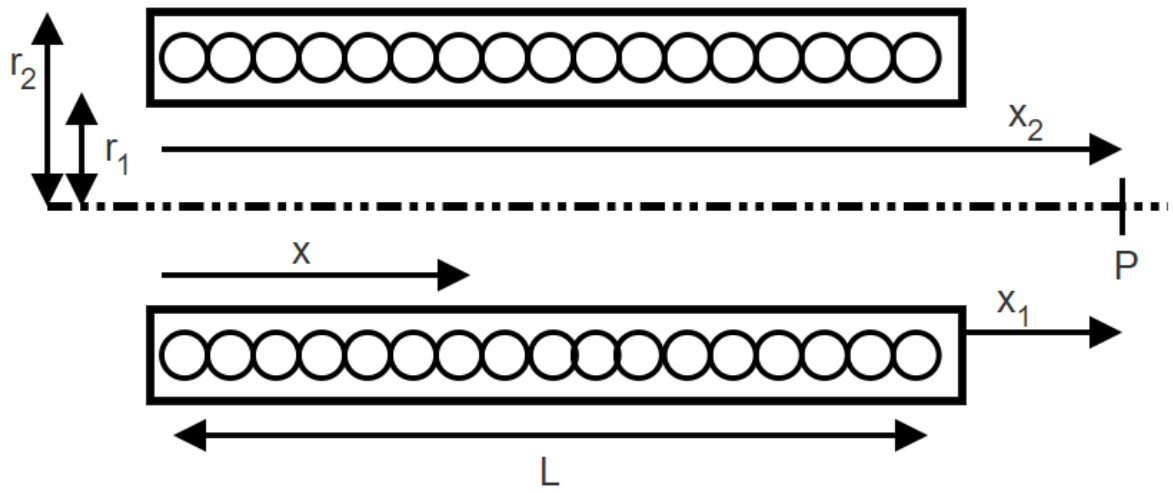

Figure 3.7 Magnetic field on the axis of a thick solenoid

The magnetic field due to a thick solenoid can be calculated by considering an ideal thin solenoid at the center of the coil cross section, whose magnetic field is to be determined at a certain point on the axis of the coil [21].

Current density of an ideal thin solenoid is given by J = NI/L

Hence the current density for a thick solenoid will be $J_\lambda = Jdr$

Where, r = radius of the coil measured from the ideal central location of the thin coil, and it varies from r_1 to r_2.

$$dB = \frac{u_0 NI}{2L} dr\left[\frac{x_2}{\sqrt{x_2^2 + r^2}} - \frac{x_1}{\sqrt{x_1^2 + r^2}}\right]$$

Now, we know the from basics of integration:

$$\int \frac{1}{\sqrt{x^2+a^2}} = \frac{1}{a}\int \frac{1}{\sqrt{1+\frac{x^2}{a^2}}}dx$$

$$= \ln\left(\sqrt{x^2+a^2}+x\right) ; (put\ x = a\tan\theta)$$

Therefore, the net magnetic field at point P due to thick solenoid can be formulated as:

$$B = \frac{u_0 NI}{L(r_2-r_1)}\left[x_2\, ln\left(\frac{\sqrt{r_2^2+x_2^2}+r_2}{\sqrt{r_1^2+x_2^2}+\ r_1}\right) -\ x_1\, ln\left(\frac{\sqrt{r_2^2+x_1^2}+r_2}{\sqrt{r_1^2+x_1^2}+\ r_1}\right)\right] \ldots\ldots\ldots\ldots (3.7)$$

3.1.6 Magnetic field off the axis of a circular current carrying coil

Consider a circular conducting ring carrying a constant current 'I'. From Biot Savart's law we know that the magnetic field generated by a current element $I\overrightarrow{dl}$ at a distance r from the current element is given by: $\overrightarrow{dB} = \frac{u_0}{4\pi}\frac{I\overrightarrow{dl}\ X\ \hat{r}}{r^2}$

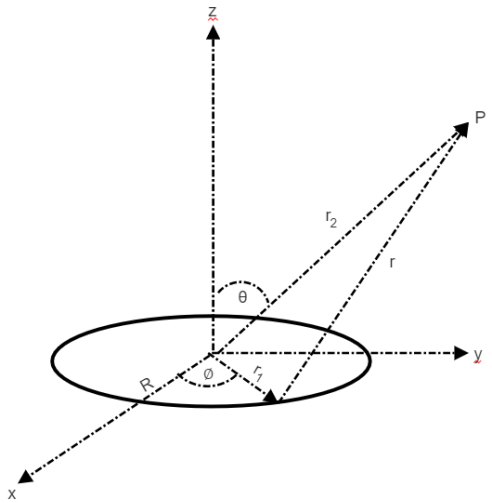

Figure 3.8 Off-Axis magnetic field due to a circular current carrying conductor

Now, the total magnetic field at point P will be the summation of magnetic fields due to all the current elements.

$$B = \frac{u_0 I}{4\pi} \int \frac{\overrightarrow{dl}\, X\, \hat{r}}{r^2}$$

Location of the current element $= R(cos\,\emptyset\,\hat{\imath} + sin\,\emptyset\hat{\jmath})$

$$I\overrightarrow{dl} = I\left(d\vec{r}_1/_{d\emptyset}\right) d\emptyset$$

$$\overrightarrow{Idl} = \; Rd\emptyset\,(-Sin\emptyset\,\hat{\imath} + cos\emptyset\hat{\jmath})$$

For simplicity of analysis the off-axis point is considered in the YZ plane to cancel the components of magnetic field generated due to the current elements lying symmetrically to this point.

$$\overrightarrow{r_2} = y\hat{\jmath} + z\hat{k}$$

$$r = \overrightarrow{r_1} - \overrightarrow{r_2} = y\hat{\jmath} + z\hat{k} - R\,cos\,\emptyset\,\hat{\imath} - R\,sin\,\emptyset\,\hat{\jmath}$$

$$\vec{r} = -R\,cos\,\emptyset\,\hat{\imath} + (y - R\,sin\,\emptyset)\hat{\jmath} + z\hat{k}$$

$$\overrightarrow{dl}\, X\, \vec{r} = Rd\emptyset\,[-Sin\emptyset\,\hat{\imath} + cos\emptyset\hat{\jmath}]\,\mathrm{X}\,[-R\,cos\,\emptyset\,\hat{\imath} + (y - R\,sin\,\emptyset)\hat{\jmath} + z\hat{k}]$$

$$det\begin{bmatrix} \hat{\imath} & \hat{\jmath} & \hat{k} \\ -\,sin\,\emptyset & cos\phi & 0 \\ -R\,cos\,\emptyset & y - R\,sin\,\emptyset & z \end{bmatrix}$$

$$\overrightarrow{dB} = \frac{u_0 IR}{4\pi} \frac{z\,cos\,\emptyset\,\hat{\imath} + zsin\,\emptyset\,\hat{\jmath} + (R - y\,sin\,\emptyset)\hat{k}d\emptyset}{(R^2 + y^2 - 2Ry\,sin\,\emptyset)^{3/2}}$$

$$B(0, y, z) = \int_0^{2\pi} \frac{u_0 IR}{4\pi} \frac{z\,cos\,\emptyset\,\hat{\imath} + zsin\,\emptyset\,\hat{\jmath} + (R - y\,sin\,\emptyset)\hat{k}d\emptyset}{(R^2 + y^2 - 2Ry\,sin\,\emptyset)^{3/2}}$$

x components of the magnetic field can be neglected as they cancel out each other due to symmetry.

$$B(y) = \int_0^{2\pi} \frac{u_0 IR}{4\pi} \frac{zsin\,\emptyset\,d\emptyset}{(R^2 + y^2 - 2Ry\,sin\,\emptyset)^{3/2}} \ldots\ldots\ldots\ldots (3.8)$$

$$B(z) = \int_0^{2\pi} \frac{u_0 IR}{4\pi} \frac{(R - y\,sin\,\emptyset)\hat{k}d\emptyset}{(R^2 + y^2 - 2Ry\,sin\,\emptyset)^{3/2}} \ldots\ldots\ldots\ldots (3.9)$$

The above elliptic integrals can be solved in MATLAB or by using the following assumptions, which presume that the location of the test point is far greater than the radius of the circular current carrying conductor.

$$if R \ll (y^2 + 2^2) = r$$

$$(R^2 + y^2 + z^2 - 2Ry\sin\phi)^{-3/2} = \frac{1}{-r^3}\left(1 + \frac{R^2 - 2Ry\sin\emptyset}{r^2}\right)^{-3/2}$$

$$\frac{1}{r^3}\left(1 - \frac{3}{2}\left(\frac{R^2 - 2yR\,sin\,\emptyset}{r^2}\right) + \cdots\right)$$

After neglecting higher order terms,

$$B_y = \frac{u_0 I}{4}\frac{3zR^2 y}{r^5}$$

Similarly, by neglecting higher order terms, we can calculate the magnetic field in the z direction as:

$$Bz = \frac{\mu_0 I}{4}\frac{R^2}{r^3}\left(2 - \frac{3y^2}{r^2}\right) \ldots\ldots\ldots\ldots (3.10)$$

3.1.7 Magnetic Field off the Axis for a Thick Shell Solenoid

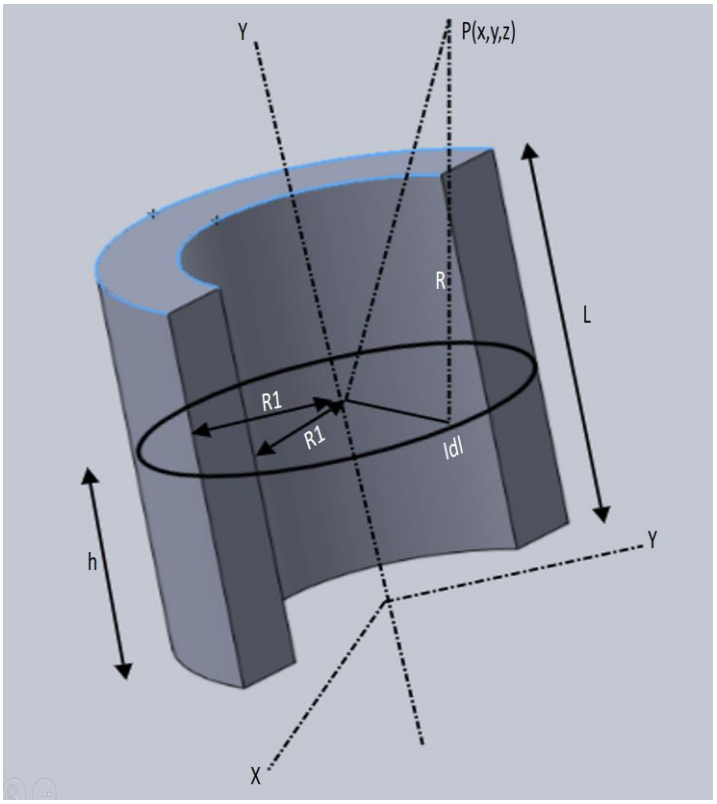

Figure 3.9 Magnetic field off the axis of a thick solenoid

The final step in analytical modelling for this project is calculating the magnetic field at off-axis locations due to a thick solenoid. This situation is the closest approximation to the real world and actual coils manufactured in this research. In later sections, it will be proved that the results from these analytical field models match closely with the FEA and experimental results. From the results of a circular current carrying coil:

$$I\overrightarrow{dl} = Rd\phi(-sin\,\emptyset\,\hat{\imath} + cos\,\emptyset\,\hat{\jmath})$$

Location of the point of interest P = $x\hat{\imath} + y\hat{\jmath} + (z-h)\hat{k}$

Location of the current element = $a(cos\,\emptyset\hat{\imath} - sin\,\emptyset\,\hat{\jmath})$

$$\vec{R} = x\hat{\imath} + y\hat{\jmath} + (z-h)\hat{k} - a(cos\,\emptyset\hat{\imath} - sin\,\emptyset\,\hat{\jmath})$$

Where a = radius of the ideal thin shell solenoid and Current density $J_\lambda = Jdr$ [21]

$$\Rightarrow B(x,y,z) = \frac{\mu_0 IN}{4\pi L}\int_0^{2\pi}\int_{-\frac{L}{2}}^{\frac{L}{2}}\int_{r_{in}}^{r_{out}} \frac{r(-\sin\phi\hat{\imath} + \cos\phi\hat{\jmath})\;X\;R}{R^3}\,d\phi dr dz$$

$$\Rightarrow B(x) = \frac{\mu_0 IN}{4\pi L}\int_0^{2\pi}\int_{-\frac{L}{2}}^{\frac{L}{2}}\int_{r_{in}}^{r_{out}} \frac{r(\cos\phi)(z-h)\hat{\imath}}{R^3}\,d\phi dr dz$$

$$\Rightarrow B(y) = \frac{\mu_0 IN}{4\pi L}\int_0^{2\pi}\int_{-\frac{L}{2}}^{\frac{L}{2}}\int_{r_{in}}^{r_{out}} \frac{r(\sin\phi)(z-h)\hat{\jmath}}{R^3}\,d\phi dr dz$$

$$B(z) = \frac{\mu_0 IN}{4\pi L}\int_0^{2\pi}\int_{-\frac{L}{2}}^{\frac{L}{2}}\int_{r_{in}}^{r_{out}} \frac{cos\emptyset(x - rcos\emptyset) + \; sin\emptyset(y - sin\emptyset)}{R^3}\,\hat{k}d\phi dr dz \;\ldots\ldots\ldots\ldots (3.11)$$

Where $R = \sqrt{(x - rcos\emptyset)^2 + (y - rSin\emptyset)^2 + \;(z-h)^2}$

The equations formulated in this section form the basis of validation of finite element models developed in Ansys Maxwell. Both analytical and finite element models will be compared with the magnetic field results obtained from a high-resolution gauss meter with both tangential and axial field measuring probes.

3.2 Finite Element Modelling and Optimization

Due to the nonlinear nature of magnetic fields and advances in the capabilities of current FEA software, the final optimization of the coil geometry was performed on Ansys Maxwell. This approach facilitated the evaluation of multiple design parameters on coil performance individually and collaboratively. The finite element coil optimization is divided into two subsections. Section 3.2.1 elaborates the optimization of coil geometry for an iron particle on the axis of a 2D coil in Ansys Magnetostatic Module. Section 3.2.2 illustrates the optimization of coil geometry, core tips and orientation in 3D. This section also covers the effect of inclination and number of coils on the force experienced by a test particle. The concept of a taper coil is also realized in this section along with the effect of core tip shapes on the magnetic field distribution in the test region. OFF-axis optimization is only performed in 3D as for a 2D case any test particle away from the central axis would become a ring, as the model is symmetric about Z-axis.

3.2.1 Optimization of Electromagnet Geometry in 2D

A two-dimensional model is very critical for the optimization process at it encompasses the least number of assumptions in finite element modelling. Furthermore, due to the simplicity of the model a finer mesh can be implemented for accurate results. However, it must be noted that an adaptive meshing technique was implemented to achieve an energy error of less than 0.1%. To optimize and compare the analytical and simulation results, it has been assumed that the wires are perfectly wound with no air

gap and hence a fit factor of 0.86 has not been yet considered but will be considered towards the end of the optimization process.

3.2.1.1 Comparison of Air Core and Iron Core Electromagnets

Initially simulations were performed for an air core coil to study the effect of various physical and process parameters such as working gap, length and current density on coil performance. Fig. 3.10 illustrates the initial 2D (cylindrical coordinates) air core model used to understand the behavior and magnetic field generated around an air core coil.

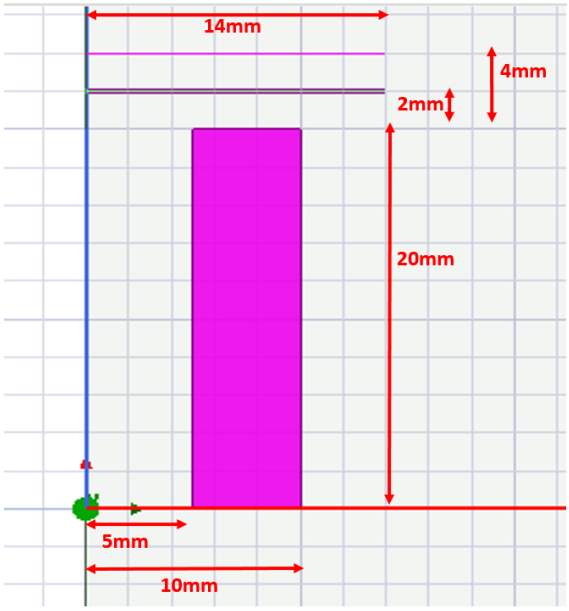

Figure 3.10 Dimensions of initial 2D air core coil setup

The magnetic field due to the above setup was measured at 3 different test locations:

a) Vertical line coinciding with the coil axis (length = 15 mm)

b) Lower horizontal line at 2 mm above the coil to measure off-axis values (length = 14mm)

a) Upper horizontal line at 4 mm above the coil to measure off-axis values (length = 14mm)

Following are the process parameters used to generate the magnetic field around the given air core coil as depicted in Fig. 3.11.

Total ampere turns = 3*800 = 2400A; Material of coil: copper; Number of turns of copper wire (N) = 800; Coil inner and outer radius = 5mm; 10mm; Length of the coil = 20mm

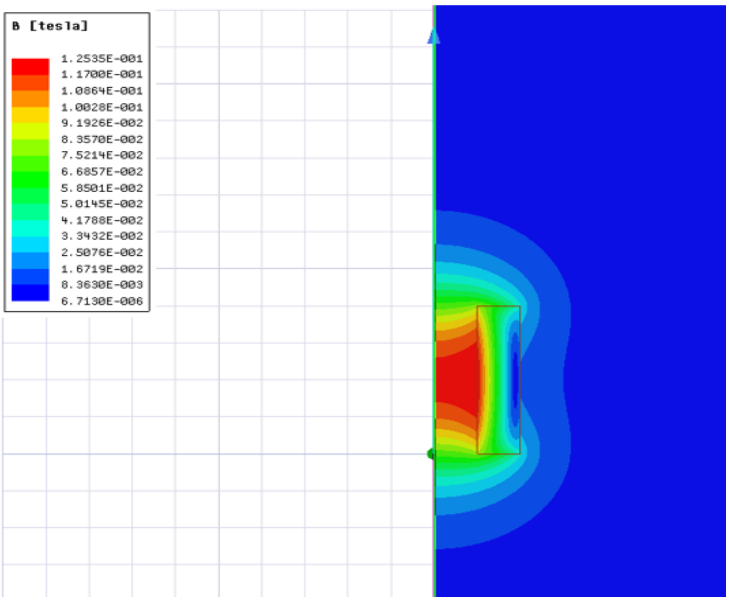

Figure 3.11 Magnetic field around an air core coil

A MATLAB code developed using the analytical models explained in section 3.1, was used to compare the results generated by finite element analysis (Fig. 3.15). A comparison of iron core and air core coils was also performed to drive the optimization process in the right direction. Fig. 3.12 illustrates the amplification of magnetic field due to the addition of an iron core with relative permeability of 4000. It can be observed quantitatively and qualitatively from Fig. 3.16 and Fig. 3.17 that the magnetic field increases approximately by 3 times due to the addition of an iron core to the coil. The following intensity plots illustrate the effect of addition of an iron core on the magnetic field at the three target locations as mentioned above.

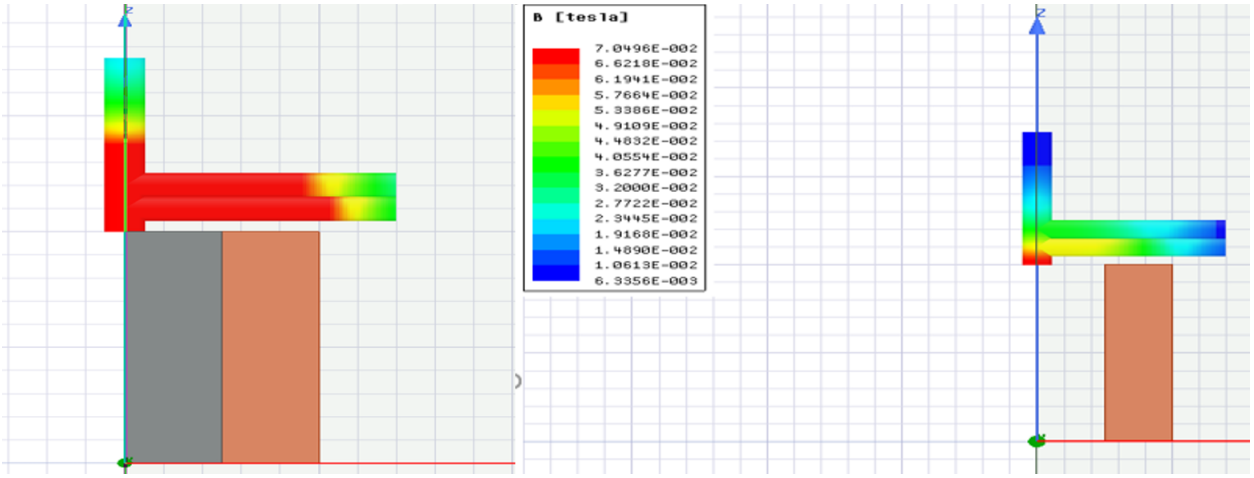

Figure 3.12 Increase in magnetic field due to the addition of an iron core for 3 different test locations

Fig. 3.13 and Fig. 3.14 illustrate the distribution of magnetic flux lines inside an iron core and on a sample testing location above the coil.

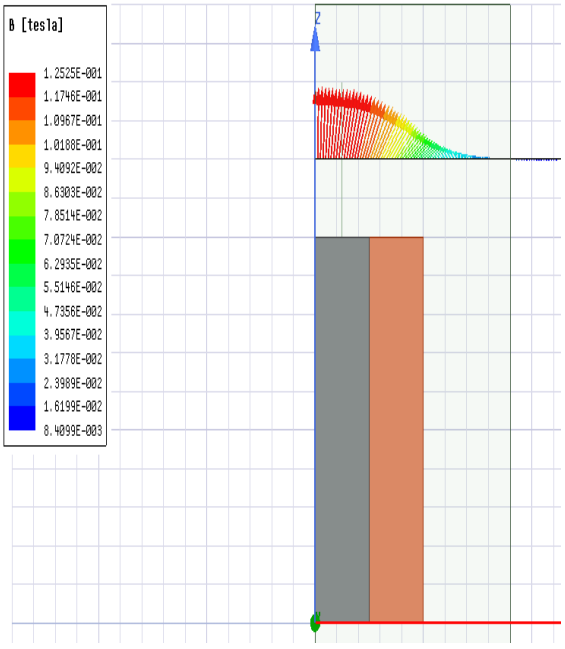

Figure 3.13 Magnetic flux lines at a test location 5 mm above an iron core coil

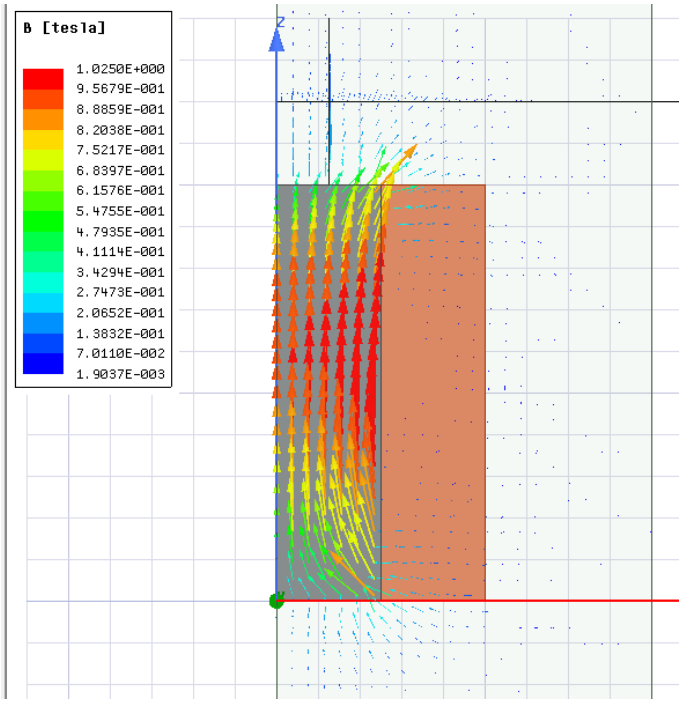

Figure 3.14 Magnetic flux lines inside an iron core coil

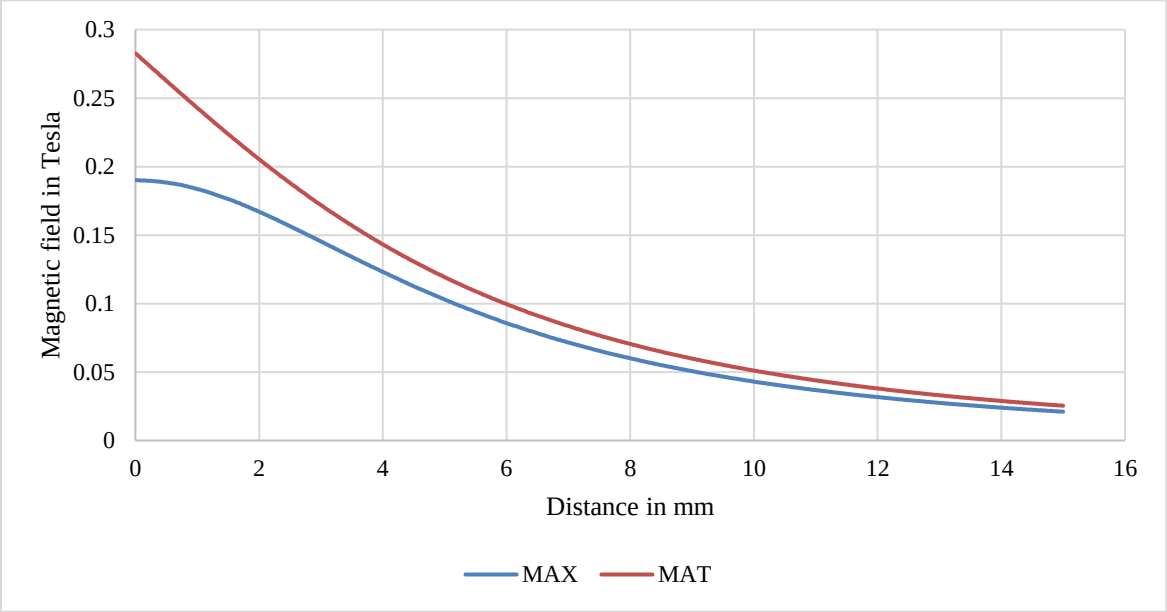

Figure 3.15 Comparison of iron core field results (on the axis of the coil) produced by analytical model (MAT) and FEA (MAX) using relative permeability

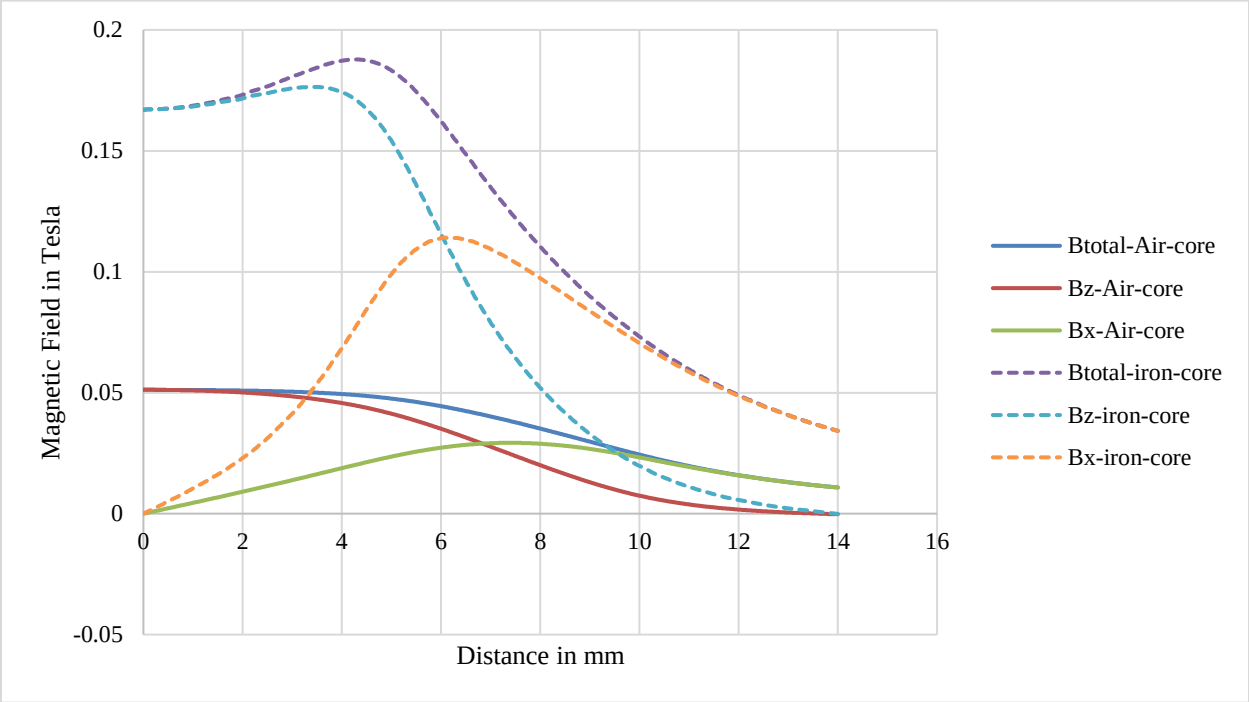

Figure 3.16 Comparison of Air Core and Iron Core Magnetic Field- lower horizontal location

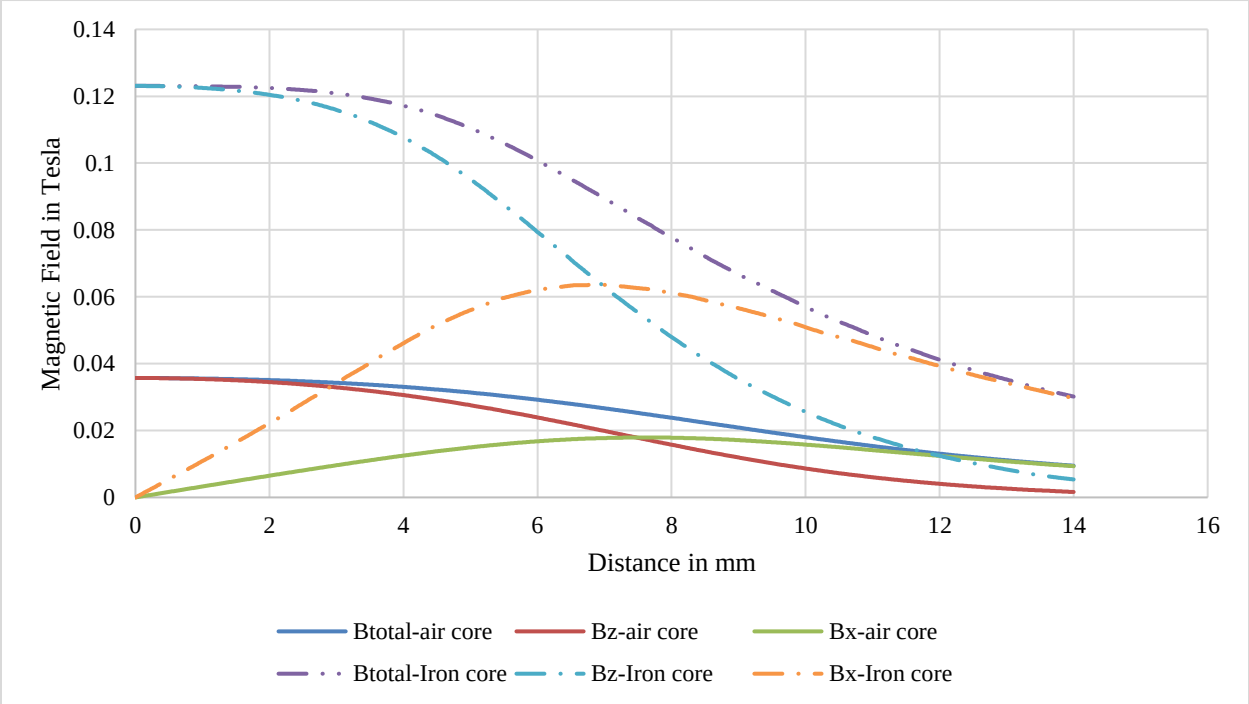

Figure 3.17 Comparison of Air Core and Iron Core Magnetic Fields - upper horizontal location

Fig. 3.18 compares the magnetic field at the lower horizontal location using MATLAB anlytical model and FEA simulatios. It can be concluded that the results of MATLAB and ANSYS completely overlap each other for an air core electromagnet. For ON axis case the magnitude of the total magnetic field is same as the magnetic field in the Z direction which is due to the fact that the radial components of the magnetic field cancel each other on the axis which leaves only axial component. It must be noted that 'MT' represents Matlab analytical model and 'MX' represents Maxwell finite element model.

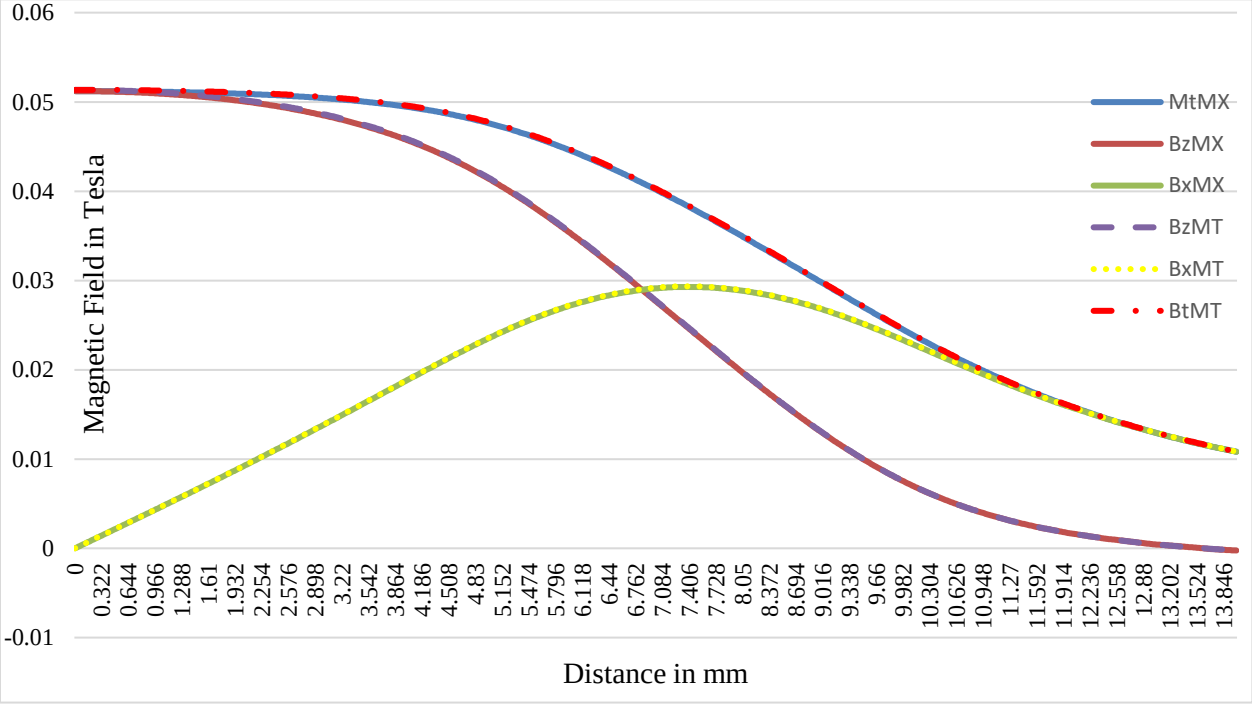

Figure 3.18 Verification of analytical and finite element results on lower horizontal

After validating the benefits of an iron core electromagnet, two-step dimensional optimization was performed in Ansys 2D magnetostatic module. The first step includes optimizing the radial dimensions (inner and outer radii of the coil) using parametric sweep analysis, and the second step includes optimization of the length of the coil using the analytical method of Fabry factor for maximum power efficiency. Initially the optimization procedure is aimed at maximizing the force produced by an iron

core coil at 10mm working gap on the axis of the coil. The optimization is performed to maximize the force output at 10mm on a flat iron sheet of thickness 1 mm and radius 2mm, which in turn can be a representation of about 12 spherical particles of 1mm^2 surface area. A series of parametric analysis were performed to understand the effect of individual dimensional parameters on the force and field output generated by an iron core electromagnetic coil.

1. Effect of increase in length and coil thickness on force: Fig. 3.19 illustrates that for constant current density and constant core size the larger (in terms of length and coil thickness) the coil the higher the force output. Therefore, it is clear from Fig. 3.20 that for constant current density increase in coil size (radially or axially) results in increased force output.

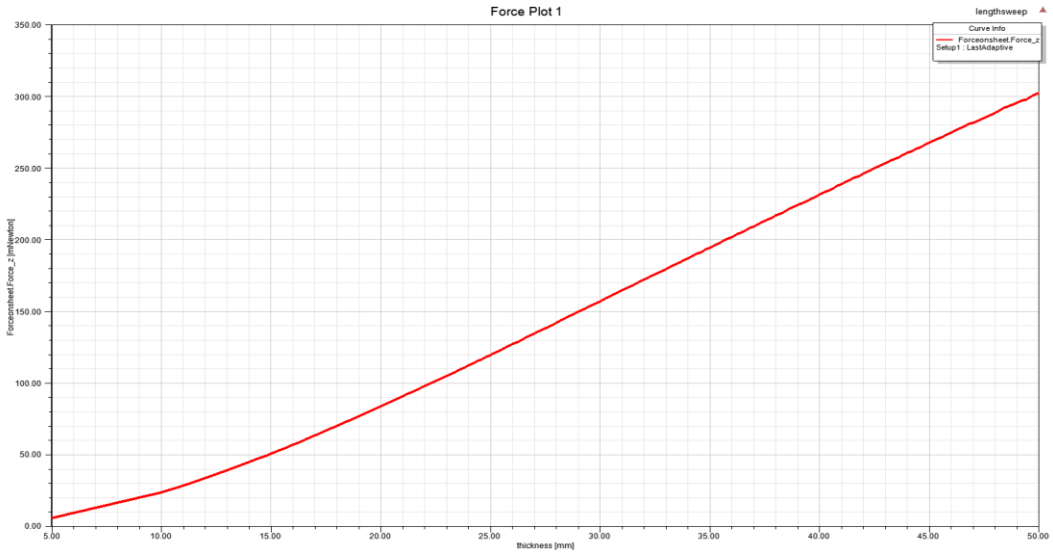

Figure 3.19 Effect of increase in coil thickness while keeping the core thickness constant at 5mm – constant current density of 24 A/mm^2

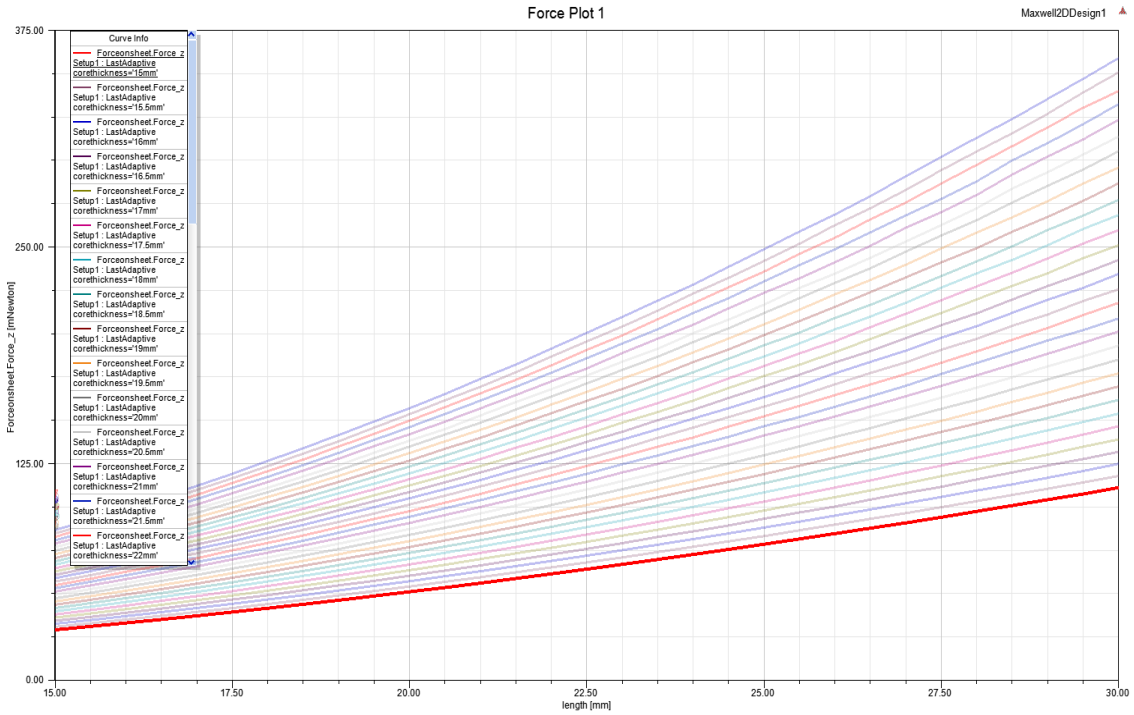

Figure 3.20 Effect of increase in coil thickness and length on force keeping core thickness constant at 5mm – constant current density of 24 A/mm^2 – Force plot

2. For an imaginary line on the axis of the coil, the magnetic field increases as the length increases (Fig. 3.21) at a constant current density of 24 A/mm^2. The horizontal axis of the plot represents the length of the imaginary line and each colored line in the plot represents a length of the coil which increases towards the top of the graph.

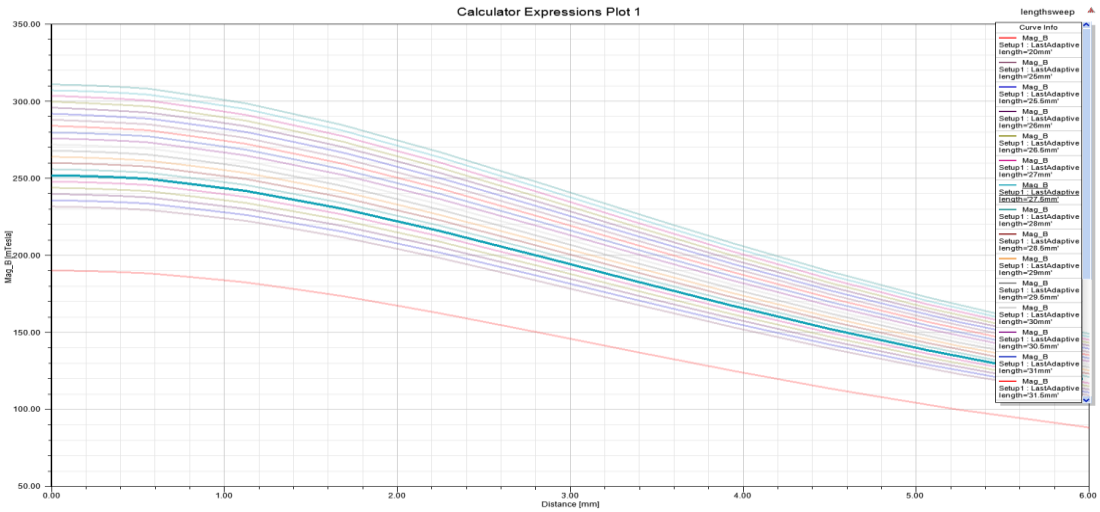

Figure 3.21 Variation of Magnetic Field on the axis of an electromagnet with increase in length

3. Effect of current density for a fixed dimension on the force output on iron test particle: After fixing the geometry (fixed outer and inner radii) and length, the current density is varied to understand the trend of the force experienced at 10 mm above the coil cross section. It can be concluded from Fig. 3.22 that the magnitude of the total force increases with the increase in current density.

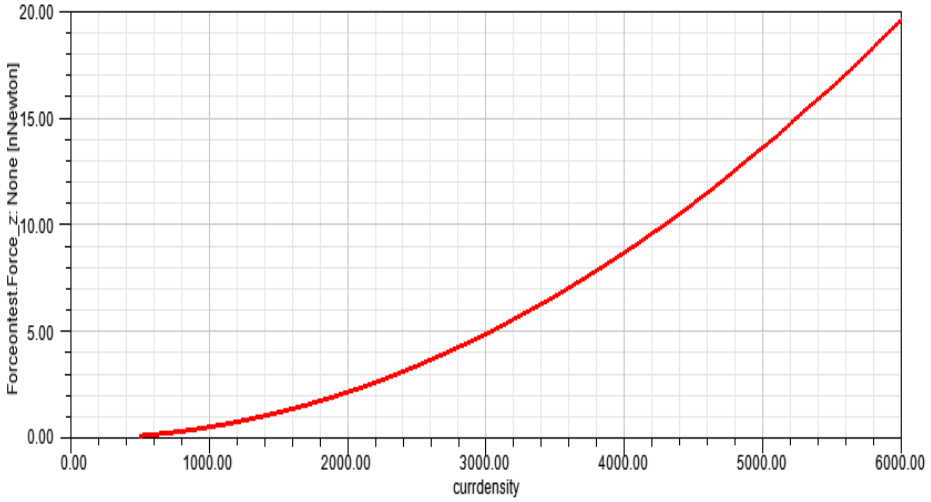

Figure 3.22 Effect of variation in current density on the force output on an iron test particle

3.2.1.2 Optimum Volume Ratio of Ferromagnetic Core to Copper Coil

It is apparent from above analysis that factors such as increase in length and coil thickness increase the force output on the iron particle. Therefore, the next step in the optimization process is to find the right balance between the volume of the core and the copper winding that should be used to produce maximum force on the axis of the ferromagnetic coil for a fixed outer radius. Fig. 3.23 and Fig. 3.24 illustrate the effect of variation in inner radius of the coil/radius of the core on the magnetic field and force produced at an imaginary fixed point on the axis of the coil.

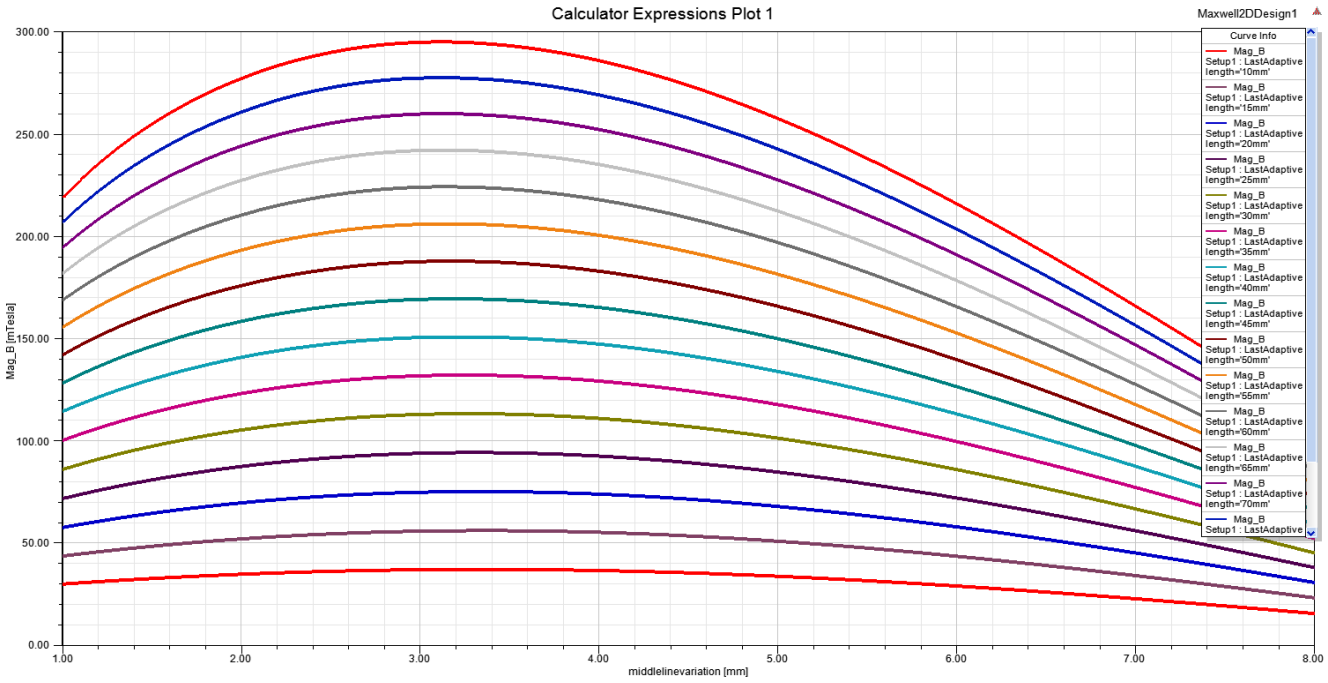

Figure 3.23 Effect of varying coil inner radius/core radius and length with fixed outer coil radius on the magnetic field at a fixed location on the axis of the coil

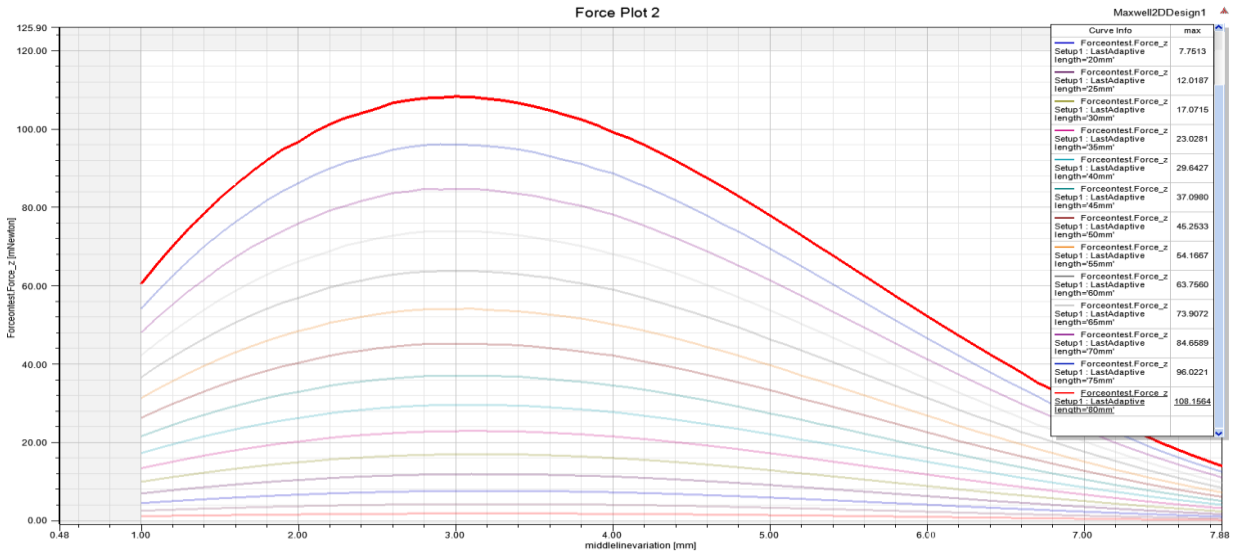

Figure 3.24 Effect of varying coil inner radius/core radius and length with fixed outer coil radius on the force experienced by an iron particle at a fixed location on the axis of the coil

Hence, increase in length increases both the force and magnetic field on the iron particles. However, increase in length has no effect on the optimized dimensions in the radial direction. However, from a power efficiency point of view, dimensions in the longitudinal direction are optimized using the concept of Fabry Factor. It must be noted that for core and coil the only variable parameters are length and thickness. The length (same for both core and coil), location of core origin (always 0) and thickness of core (coil inner radius) are some of the common variables between the core and the coil and hence facilitates the reduction of the number of variables in the optimization process. Fig. 3.28 also shows that for the same length if current density is varied the radius ratio (α) remains the constant. Fabry factor (G) for a ferromagnetic core can be formulated as:

$$G(\alpha,\beta) = \frac{\sqrt{2\pi}}{5}\sqrt{\frac{\beta}{\alpha^2-1}}\,ln\left(\frac{\alpha+\sqrt{\alpha^2+\beta^2}}{1+\sqrt{1+\beta^2}}\right) \ldots [22]$$

Where, $\alpha = \frac{r_0}{r_i}$ and $\beta = \frac{l}{2r_i}$

r_0 and r_i are the inner and outer radius of the coil and l is the length of the coil.

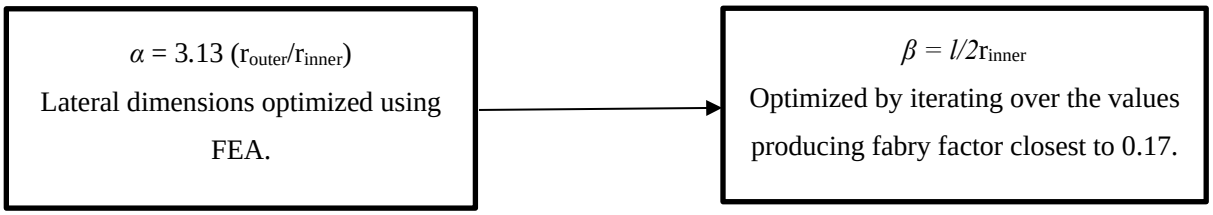

The maximum value of Fabry factor for any general case can be found by varying both, α and β from 1 to 9 to get G_{max} = 0.179 (Fig. 3.27). Hence our aim is to have optimized dimensions producing G closest to 0.179. The following table contains optimization results for 5 different cases of outer radii. Acceptable values of Fabry factor are found by varying β from 1 to 4.1 (Fig. 3.26). This means length can vary from 6 mm to 24.6 mm and since the length of the coil is directly proportional to the force applied on the test particle, maximum value of length is selected as long as G≥ 0.16. The results also match with the general dimensions of a ferromagnetic coil given by $2r_{inner} \cong 0.6r_{outer}$ [4] .

Outer radius (in mm)	Inner radius (in mm)	Percentage of Core	Length (in mm)	α	β	G
10	3	30	24.6	3.33	4.1	0.1600
15	4	26.67	34.48	3.75	4.31	0.1602
20	4.5	22.5	40.14	4.44	4.46	0.1605
25	4.5	18	50	$2r_i \neq 0 \cdot 6r_0$		0.1518
30	5	16.67	50	$2r_i \neq 0 \cdot 6r_0$		0.1549

Therefore, the percentage volume of core keeps decreasing as the size of the coil increases to maintain maximum force on the iron sheet at 10mm above the coil axis.

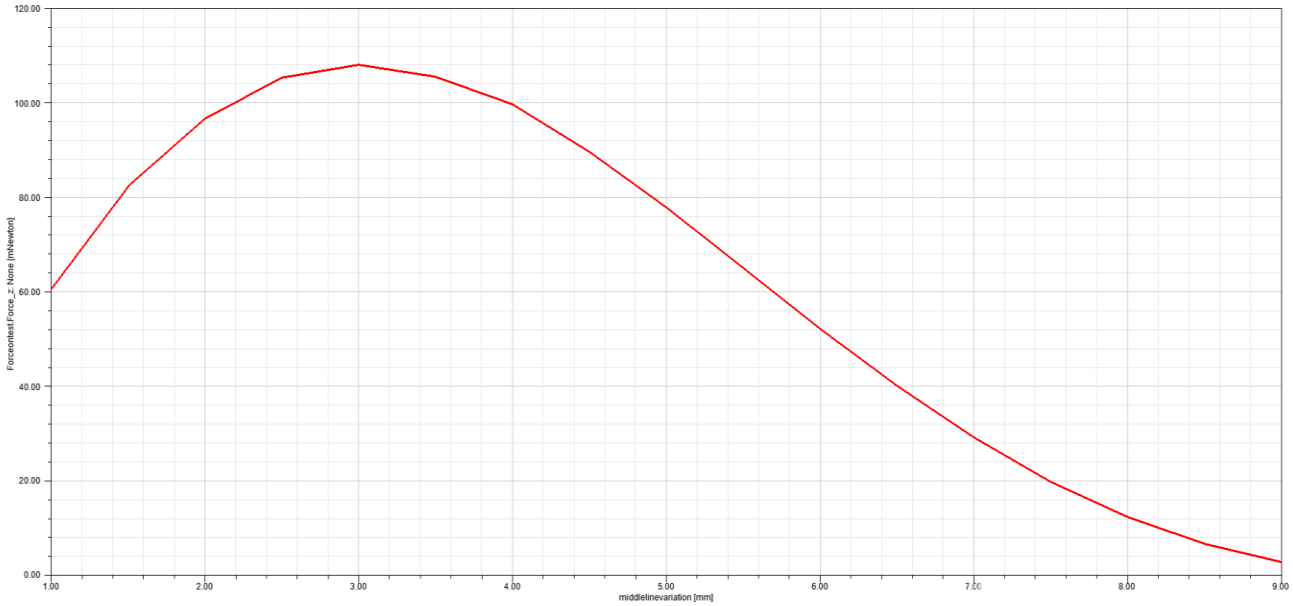

Figure 3.25 Plot of variation of inner radius for a fixed outer radius of 10 mm

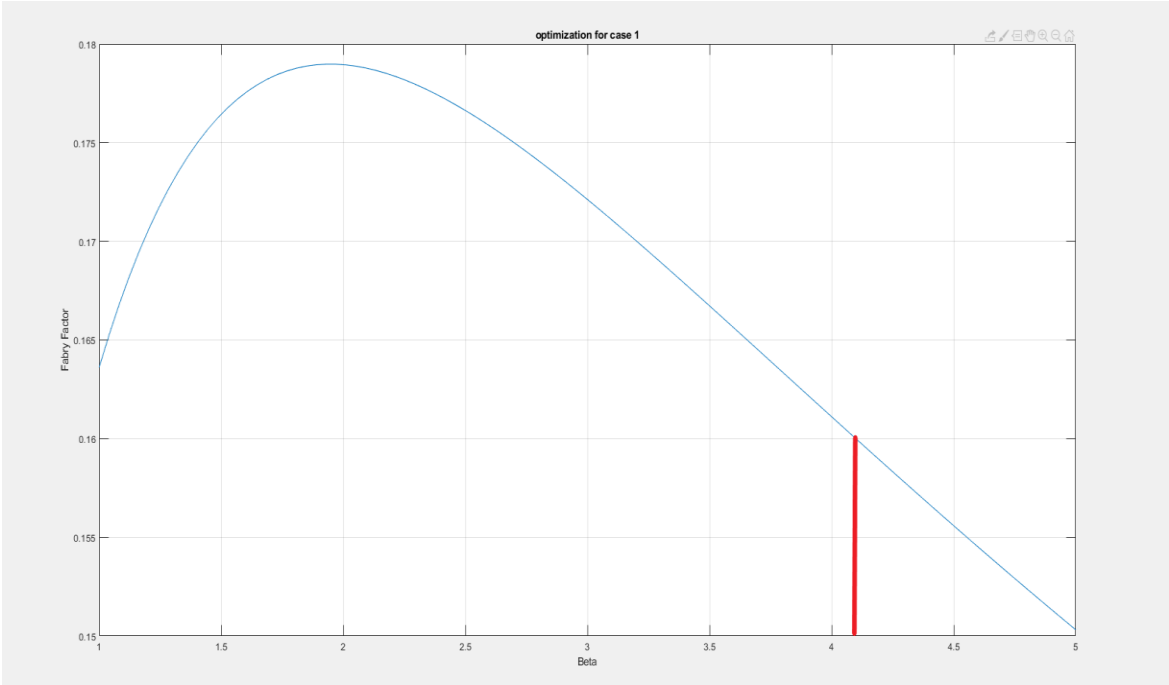

Figure 3.26 Variation of β with G to optimize the longitudinal dimensions

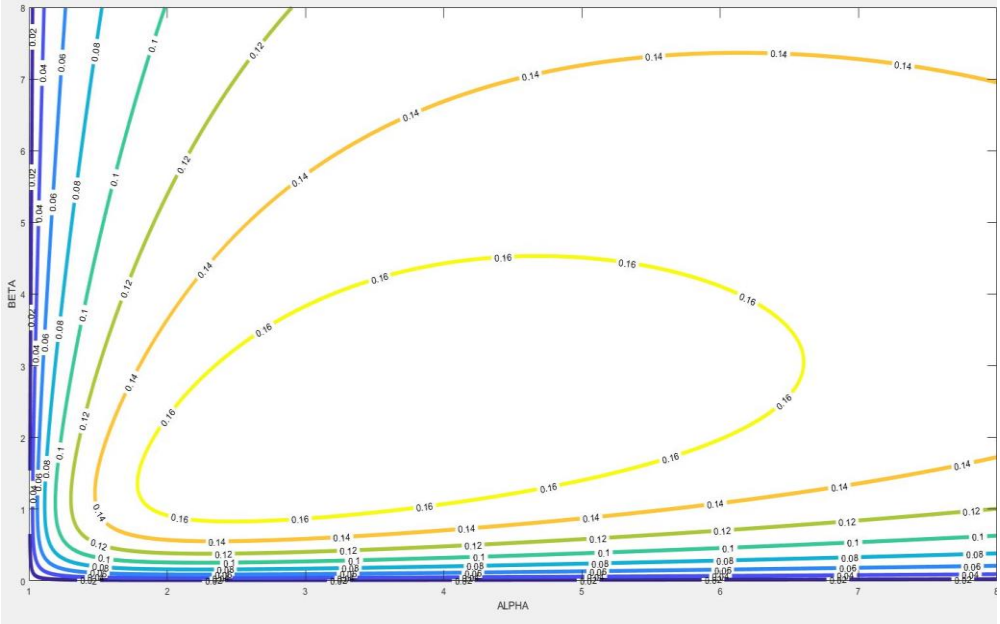

Figure 3.27 G contour plot with α and β

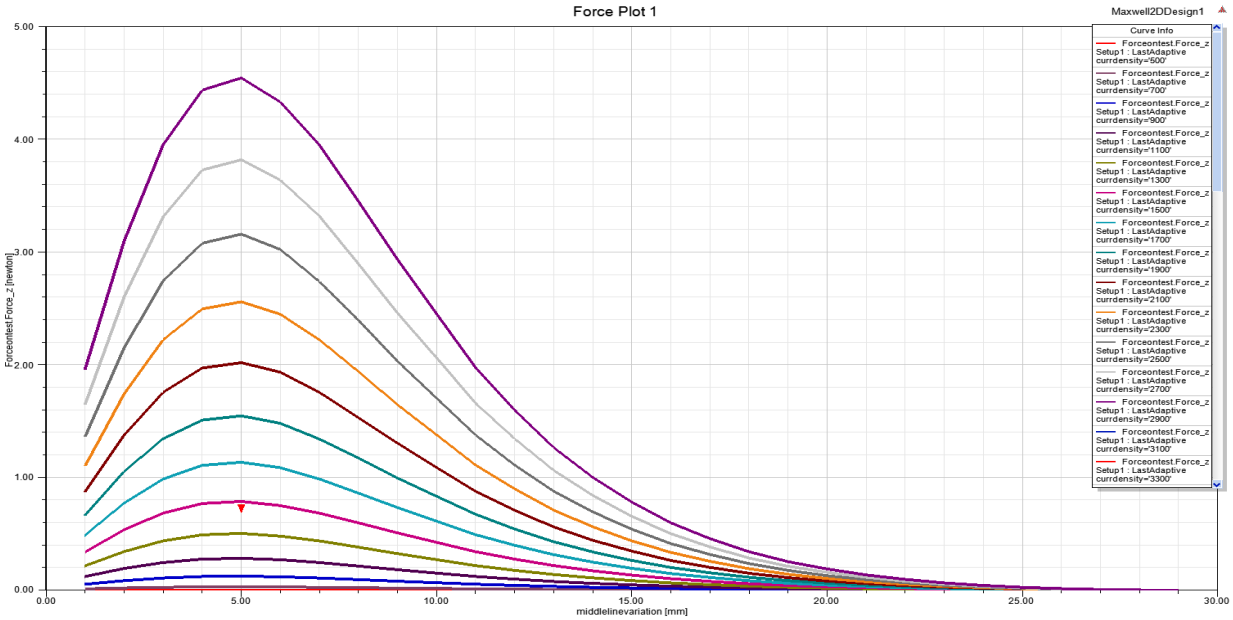

Figure 3.28 Combined effect of change in current density and radius ratio on the force experienced by a test plate on the axis of the ferromagnetic electromagnet

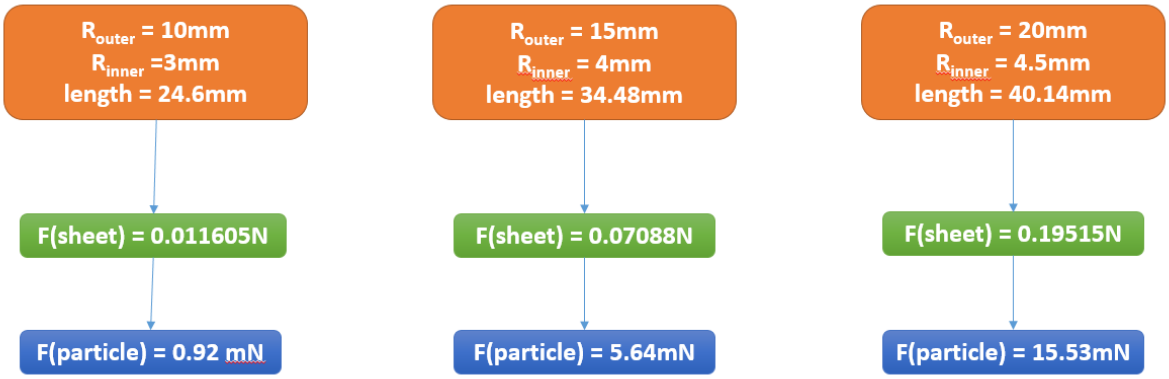

Figure 3.29 Final Optimized dimensions for ON-axis optimization in 2D

The above analysis was performed by aiming to optimize dimensions that produce a Fabry factor not lower than 0.16. Therefore, once alpha is optimized using FEA/Ansys Maxwell, increase in β results in increased length, therefore leading to more force. However, increase in β should not result in drop of Fabry factor below 0.16. βmax (with safe reasonable G) = 4.1 was considered in normal calculations and optimization sheet. Maximum Fabry factor is achieved for β ranging from 1 to 1.91.

The tangential forces (f_t), generated due to the relative motion between the flexible magnetic abrasive brush and the workpiece, are responsible for the microchipping of the workpiece surface. However, microchipping will only take place if f_t is greater than the resistance offered by the workpiece against its deformations (a function of material hardness, yield strength and ultimate strength). Normal forces, on the other hand, are responsible for the penetration/indentation depth of the MAPs into the workpiece [10]. Normal forces impact the change in surface roughness (ΔRa), this means that a constant normal force will not change the depth of indentation and hence ΔRa will remain constant, irrespective of the magnitude of the tangential force. An increase in current increases the magnetic field and hence the normal and tangential forces on the test particle also increase. However, for successful

microchipping of the material, the tangential forces must be maximized as well. This is because higher normal forces result in greater penetration and hence increased resistance for chip formation. To compensate for this increase in resistance the tangential forces will have to consequently increase. Therefore, we can conclude that force components form the basis of electromagnetic coil design.

One of the most important parameters to be considered while designing a polishing apparatus using stationary electromagnets is that the tangential forces are not provided by the rotational motion of a mechanical equipment but through the controlled activation of adjacent coils at different instances of time. The forces in the x and y direction experienced by a test particle can be expressed by the following equations [4]:

$$F_x = V\chi H\frac{\partial H}{\partial x}$$

$$F_y = V\chi H\frac{\partial H}{\partial y}$$

Where, V is the volume of the abrasive particles in m^3, χ is the magnetic susceptibility of the MAPs, H is the magnetic field in A/m and $\frac{\partial H}{\partial y}$ and $\frac{\partial H}{\partial x}$ are the variations of the magnetic field in the x and y direction respectively. Hence the total tangential force can be represented by:

$$Ft = \sqrt{F_x^2 + F_y^2}$$

Another important parameter is the griding pressure, defined as the pressure exerted by the MAPs on the workpiece surface [4]:

$$P = \frac{H^2}{2}\left(1 - \frac{1}{\mu_m}\right) = \frac{B^2}{2\mu_0}\left(1 - \frac{1}{\mu_m}\right)$$

The above equation illustrates that the grinding pressure is proportional to the square of magnetic flux density (H). Therefore, the pressure can be increased by increasing the magnetic flux density. Since the

MAPs are not only restricted to the axial vicinity of the coil, dimensions are also optimized for off-axis force /fields test locations. This is achieved by calculating the forces on a test particle (disc with 1.1 mm radius and 1.1 mm thickness) 4 mm away from the outer edge of the coil in Ansys 3D module. Table 2 illustrates the coil inner radius corresponding to 8 different cases of fixed outer radii of the coil and the optimum value of fabry factor (power consumption). Fabry factor is a dimensionless term which only depends on the shape of the coil and not size and hence is a function of normalized coil geometry [23]. It can be observed from Fig. 3.30 that the mean value (represented by a blue line) of coil inner radius for ON axis and OFF axis case covers both the OFF axis and ON axis range. Moreover, it can be observed that neither the ON axis nor the OFF-axis force values drop/rise steeply in this range. Hence, the average radius is considered while designing the coil. Each simulation was performed for constant outer coil radii. The location of the test particle is 10mm (below) on the axis of the coil.

For example, consider the case of a 16 mm outer radius:

- Length of the coil = 20mm
- Coil inner radius for Maximum force OFF axis = 7mm
- Coil inner radius for maximum force ON axis = 4.5mm
- ON axis force for 7mm inner radius = 15.51 mN
- ON axis force for 4.5mm inner radius (maximum) = 20.93 mN
- OFF axis force for 4.5mm inner radius = 2.91 mN
- OFF axis force for 7 mm (maximum) inner radius = 3.37 mN
- Force at avg. radius (5.75mm) ON axis = 19 mN
- Force at avg. radius (5.75mm) OFF axis = 3.2 mN

It is evident that there is an acceptable 9 % and 5 % drop in the peak force for ON axis and OFF axis case if the average radius is considered. However, we have a steep peak for ON axis force plots and

hence if average inner radii are considered, the emphasis should be on selecting values closer to the ON axis case as the curve flattens out near the peak for OFF axis case.

Table 2 Optimization of single-coil dimensions based ON and OFF axis force variation and power consumption (Fabry factor)

R_{outer}	R_{inner} – ON axis (in mm)	R_{inner} – OFF axis (in mm)	alpha (range)	Beta (range) with G higher than 0.16	Fmax (ON-axis) mN	Fmax (OFF-axis) mN
16	4.5	7	2.28 – 3.55	0.82 - 3.63	22	3
18	4.5	8.5	2.117 - 4	0.81 - 3.72	28	4
20	4.5	8.5	2.35 - 4.44	0.9 - 4	38	4.7
22	4.5	10	2.2 – 4.89	0.9-4	48	5.3
24	4.5	10.5	2.28 – 5.33	0.9-4.27	58	6
26	5	13.5	1.93 - 5.2	0.9-4	70	6.8
28	5	13.5	2.07 - 5.6	0.9-4.27	76	7.5
30	5	13.5	2.22 - 6	0.9-4.3	85	8

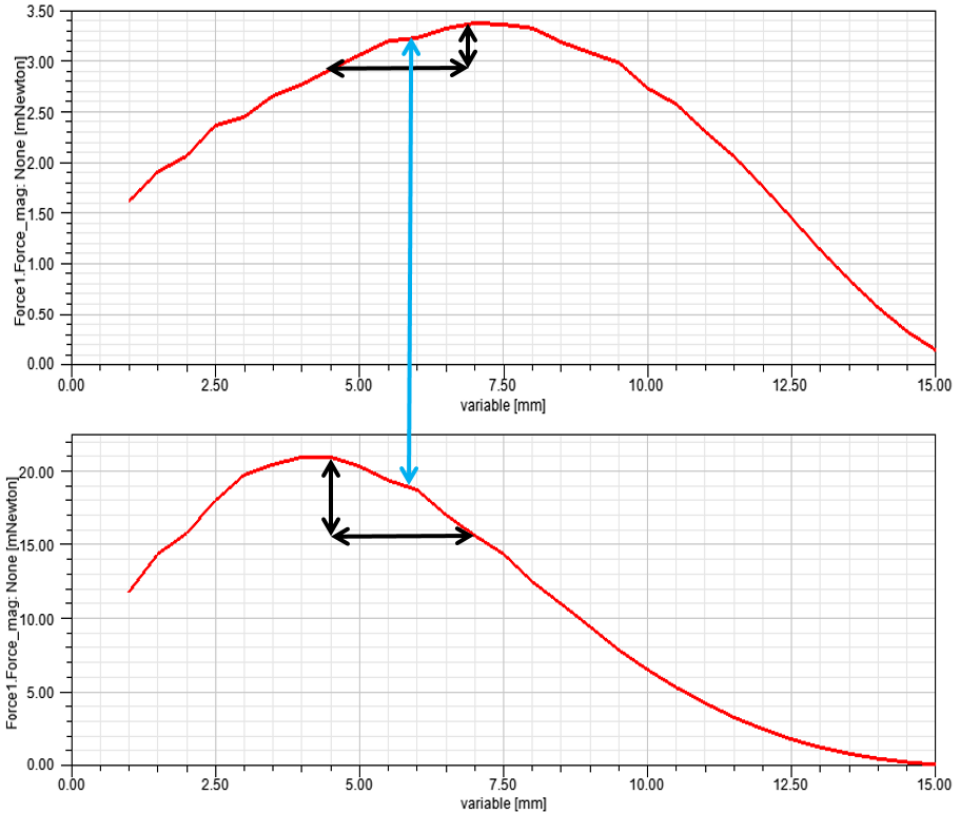

Figure 3.30 Variation of total Magnetic force (Mag F) with change in coil inner radius (variable) on the axis of the coil (bottom plot), at a location 4 mm away from the coil outer surface (top plot)

The magnetic force experienced by an iron particle can also be expressed by the gradient of the magnetic potential energy [24].

$$B = \frac{\mu_0}{2} \nabla \int M \cdot H \, dV$$

Where V is the volume of the abrasive particle. H and M are the internal magnetization and flux intensity. Also, the relation between internal magnetization (M) and magnetic flux intensity (H) in a vacuum can be expressed by the following equation:

$$B = \mu_0 (H + M)$$

However, due to the small volume of the abrasive particles M and H are considered uniform. Hence, magnetic force becomes proportional to the gradient of the magnetic field [25].

$$F = \mu_0 V(M.\nabla)H$$

$$Fn = Fz = \mu_0 V\left(Mx\frac{\partial Hz}{\partial x} + My\frac{\partial Hz}{\partial x} + Mz\frac{\partial Hz}{\partial x}\right)$$

$$Fx = \mu_0 V\left(Mx\frac{\partial Hx}{\partial x} + My\frac{\partial Hx}{\partial y} + Mz\frac{\partial Hx}{\partial z}\right)$$

$$Fy = \mu_0 V\left(Mx\frac{\partial Hy}{\partial x} + My\frac{\partial Hy}{\partial y} + Mz\frac{\partial Hz}{\partial z}\right)$$

Furthermore, to understand the relation between force and gradient of the magnetic field, forces on an iron disc were measured at different locations on a horizontal imaginary line 10 mm below the flat face of the core tip and starting from the axis of the coil. It can be observed from Fig. 3.31 to Fig. 3.33 that the total magnetic force is proportional to both the magnetic field and the gradient of magnetic field.

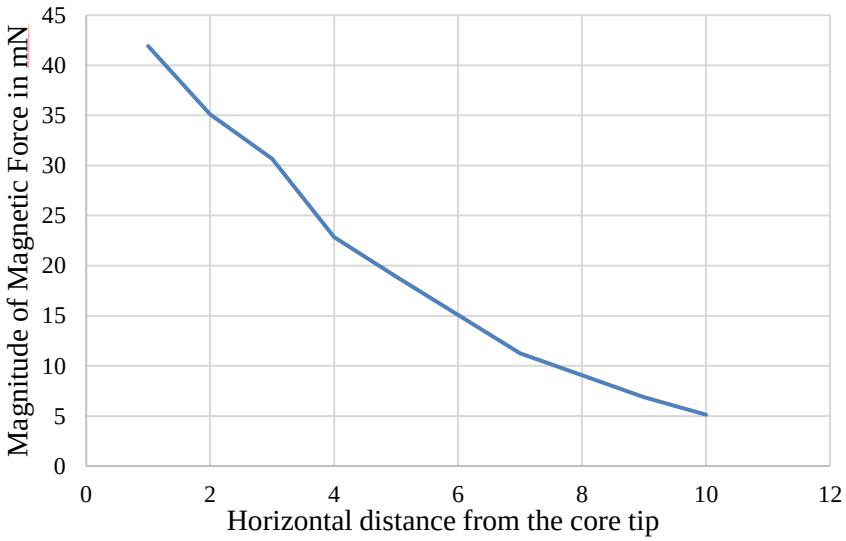

Figure 3.31 Variation of magnitude of the total magnetic force on a test particle moving on a horizontal line 10 mm below the core tip

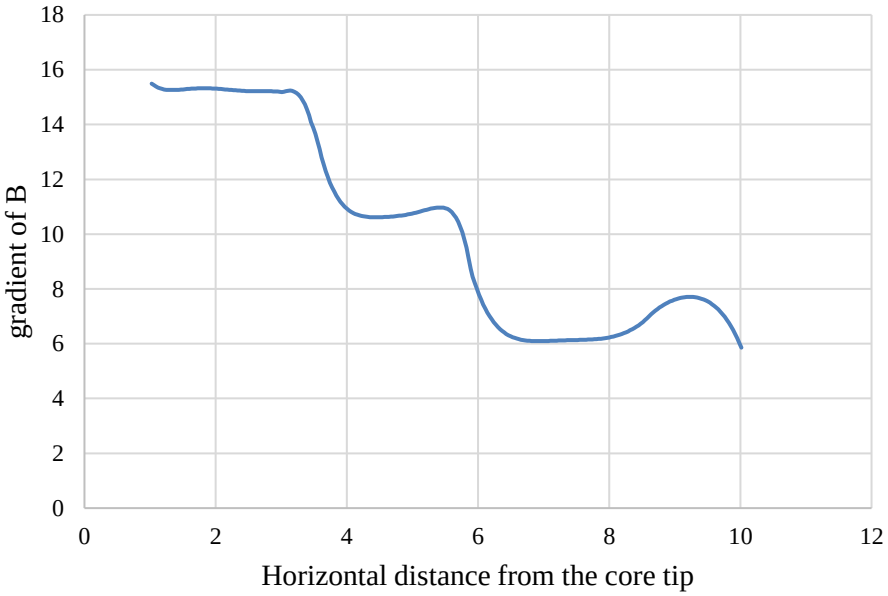

Figure 3.32 Variation of the magnetic field gradient on a horizontal line 10 mm below the core tip

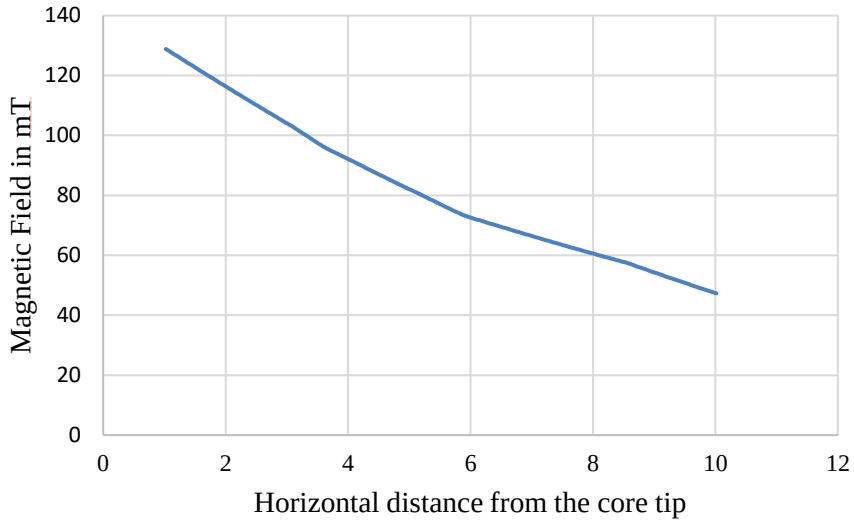

Figure 3.33 Variation of magnetic field on a horizontal line 10 mm below the core tip

3.2.2 Optimization of Coil Geometry in 3D

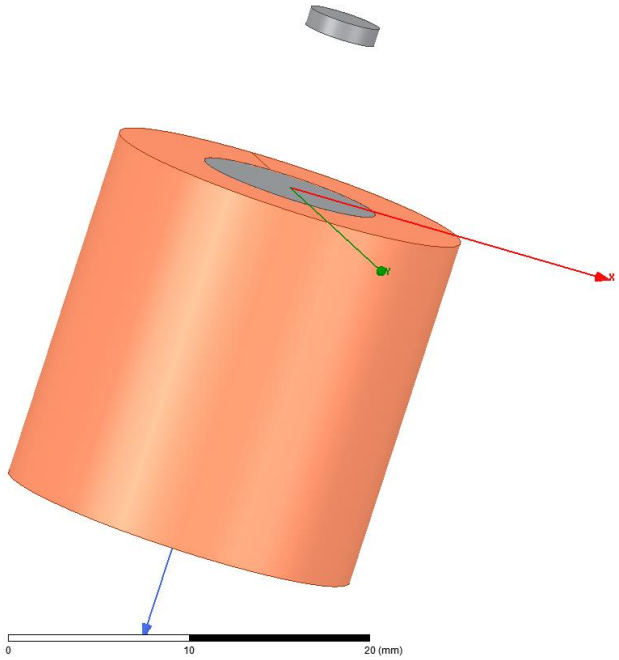

Figure 3.34 Cylindrical coil in 3D with test particle on the axis

For final optimized dimensions of both ON axis and OFF axis cases, magnetic force was measured on the axis of a cylindrical coil with constant outer diameters and varying inner diameter (equal to the diameter of the core). A separate parametric analysis was performed by varying both length and radius ratios at the same time. For a three-dimensional case the same procedure was followed as used in 2D and initial comparison checks were performed to check whether results from 2D and 3D FEA models match each other (Fig. 3.35) with an acceptable margin of error. Fig. 3.36 and Fig. 3.37 provides an idea about the difference in the relative magnitude for ON and OFF-axis force outputs. To design a coil optimized for both ON and OFF axis force outputs for a test plate 10mm above the coil cross-section, 8 different outer diameters were considered from 16 mm to 30 mm with a step increase of 2mm and the length of the coil was always fixed at 20mm. The analysis was aimed to have a definite range for coil

inner radius which produces maximum force at the test location. We know from our results in section 3.2.1 that increase in length is directly proportional to the force generated on the power output, however, length cannot be increased infinitesimally due to concerns of power efficiency and heat generated. Once two different values of coil inner radius are obtained, the dimensions are subjected to optimization using power efficiency i.e. Fabry factor (G), where both α and β are varied in MATLAB to achieve the maximum value of G.

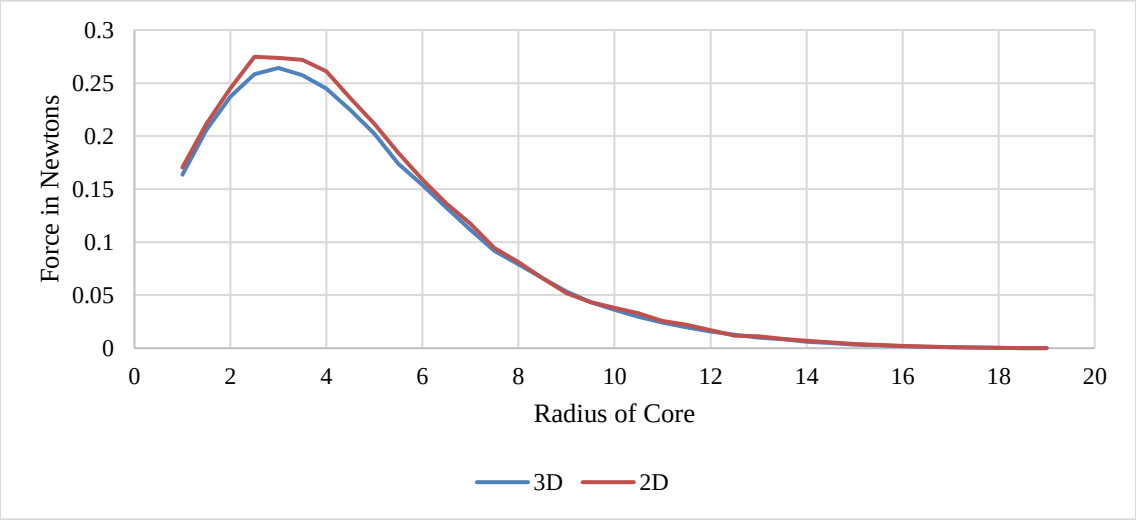

Figure 3.35 Comparison of Force Results from 2D and 3D

The case of R_{outer} = 16mm is explained for the purpose of understanding the procedure followed to optimize the dimensions after FEA results are generated. Fig. 3.36 is a plot for the variation of force produced on an ON-axis test plate with varying inner diameters. The peak corresponding to 4.5 mm produces maximum magnetic force and similarly the corresponding value for an OFF-axis case using Fig. 3.37 is 7mm. Now, once we have a range of radial dimensions the next step is to optimize longitudinal dimensions using the concept of Fabry factor. Therefore, R_{inner} will vary from 4.5 mm to 7 mm and β will vary from 1 to 9 (or we can vary the length from 10mm to 80mm) and combinations

resulting in an acceptable value of Fabry Factor (usually above 0.16) will be selected. The above optimization process was carried out for 8 different values of outer radii.

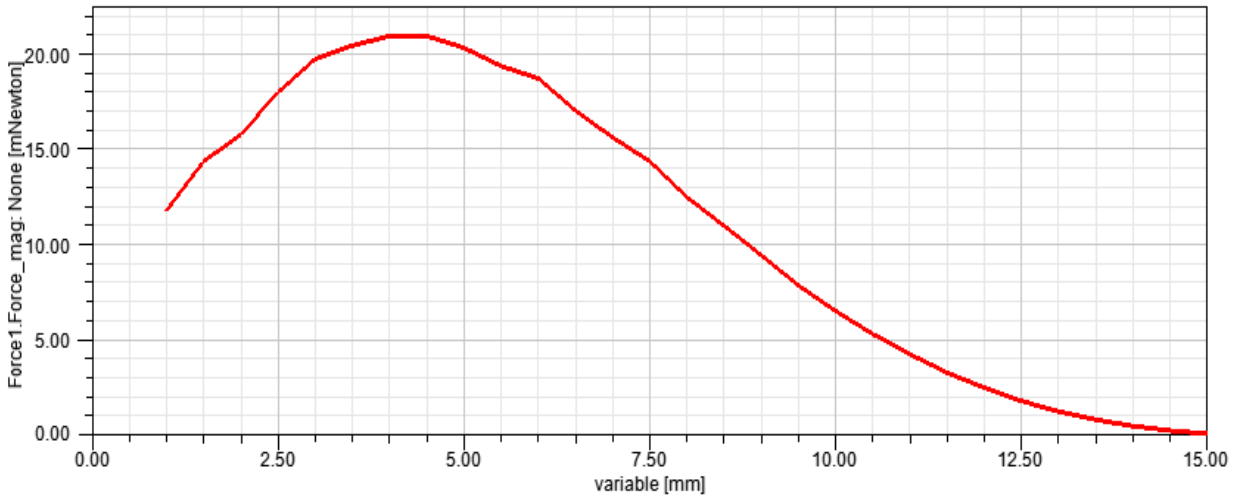

Figure 3.36 Force plot for ON-axis test plate with varying inner coil radius and constant outer radius of 16mm

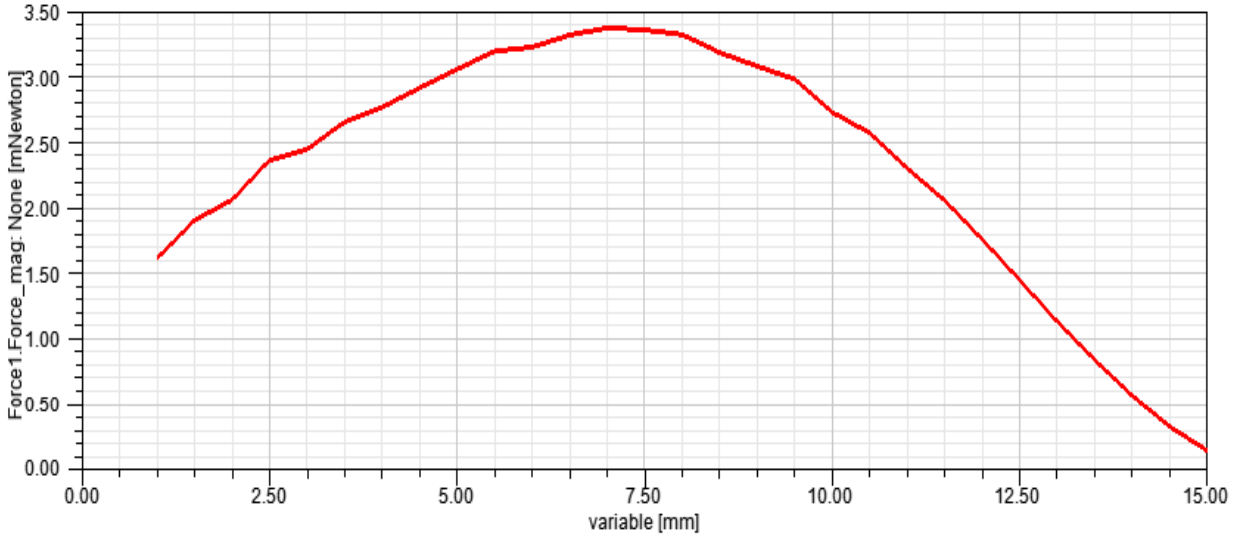

Figure 3.37 Force plot for on OFF-axis test plate with varying inner coil radius and constant outer radius of 16mm

3.2.2.1 Taper Coil

For the purpose of space efficiency and to maximize the manipulation of abrasive particles in the working area, it is optimal to introduce a greater number of coils that can be activated in a defined sequence. Hence, the concept of taper coils is introduced. The following section will elaborate on the finite element parametric analysis done to understand the effect of taper both in the axial and radial direction for electromagnets with ferromagnetic cores. The section illustrates how a typical cylindrical electromagnet only marginally outperforms its tapered counterpart in terms of magnetic field. This is because coil wrap far from the central axis contributes negligibly towards the magnetic field as compared to the current elements in the proximity of the central axis [26].

For defining the space efficiency of a coil system, we have defined a new parameter called mirror distance which is the distance used in finite element analysis setup to offset the initial coil from the origin in order to accommodate more coils. As it can be imagined that mirror distance would increase as the number of coils add up, because existing coils will have to move farther away to make space for more coils. For a 3 cylindrical coil setup the mirror distance is 14 mm. The mirror radius almost doubles on doubling the number of coils from 3 to 6. This in turn reduces the intensity of the magnetic flux in the working area

Two different taper geometries were considered a) a conical coil b) regular cylindrical coil with taper provided at one end. Taper radius is the lower radius of the coil which is essentially less than the radius of the cylindrical section. Taper length is the length of the taper section which should be minimized to avoid excessive reduction in magnetic field. Taper coils would always have less magnetic field as compared to its cylindrical counter parts due to reduction in the total number of current carrying

conductors in the cross section. Fig. 3.38 to Fig. 3.40 illustrate the effect of taper length and taper radius on the force components experienced by a spherical iron particle at an OFF-axis location for an un-tilted coil.

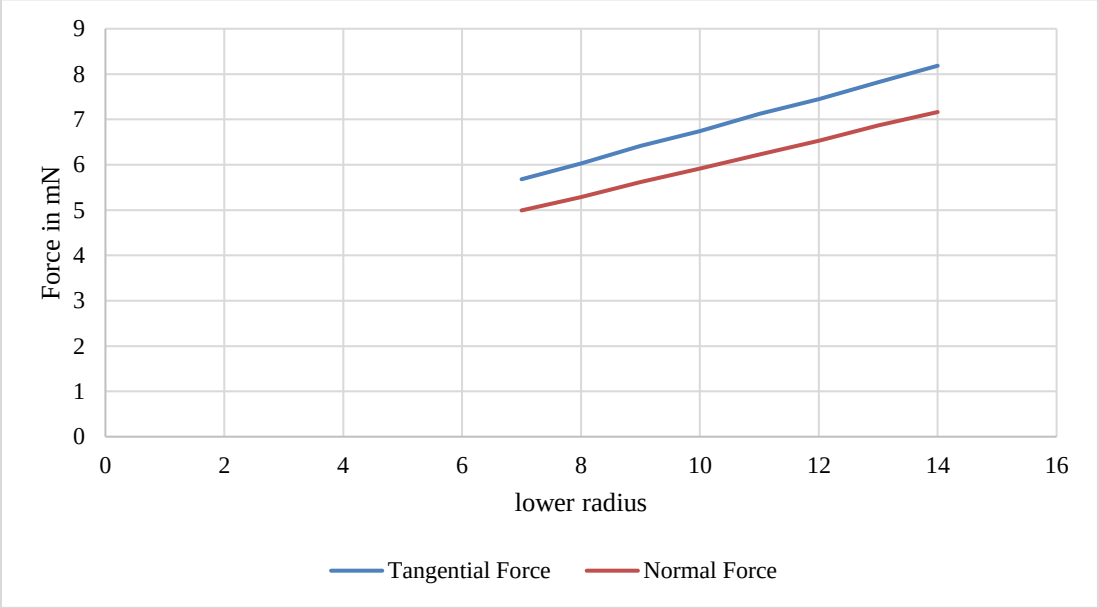

Figure 3.38 Normal/Tangential Force vs taper lower radius

It can be observed that increase in lower radius increases both the tangential and normal forces, however, increase in length has an opposite effect due to reduction in the number of current carrying conductors. Furthermore, it is found that there is a 1.05 – 3.5% decrease in magnetic field with 1mm increase in taper length. On the contrary the magnetic field increases by 1.29 - 4.93% with 1mm increase in taper radius. Hence, while optimizing the taper for a multi coil setup, it is important to prioritize high radius and low taper length.

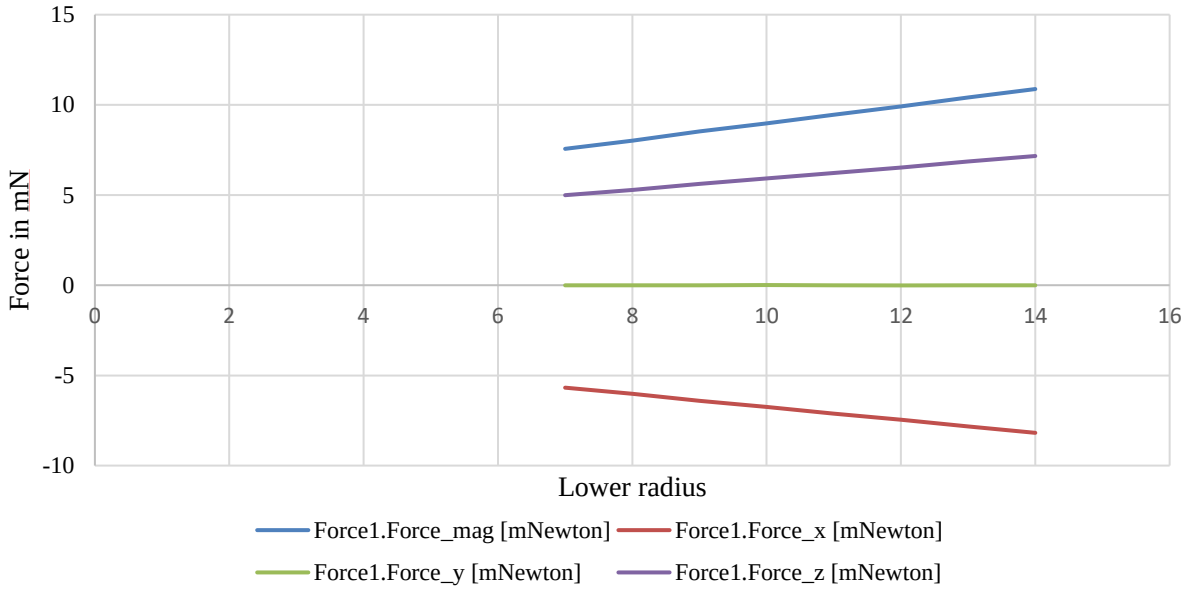

Figure 3.39 Fx, Fy, Fz, Mag F vs lower radius

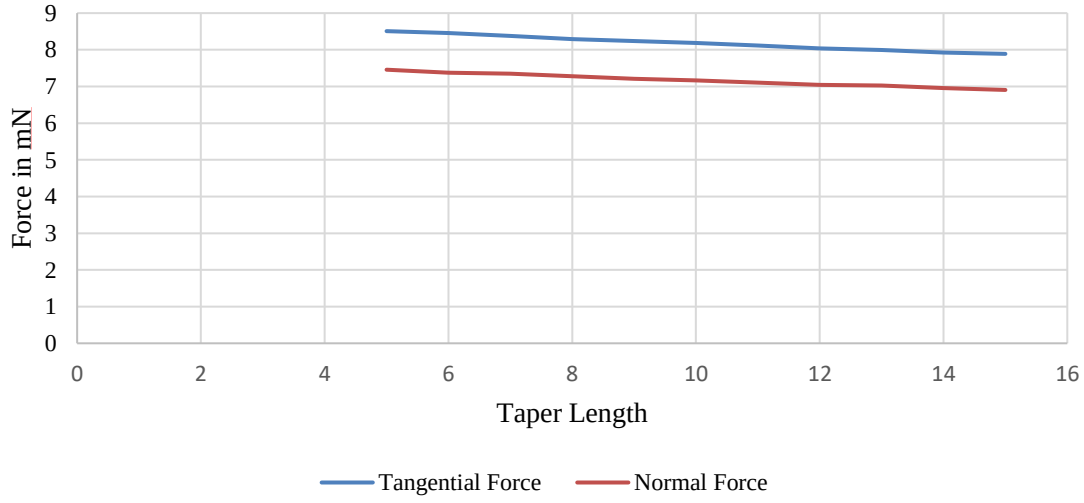

Figure 3.40 Normal/Tangential Force vs Taper Length

Fig. 3.41 illustrates the comparison between a single cylindrical and a taper coil by plotting the magnetic field on the axis of the coil. The grey line represents coil with a taper length of 1 mm and taper radius of 7mm and the orange line represents a taper length of 10 mm and a taper radius of 6mm.

Conventional cylindrical coil is represented by the blue line. It can be clearly observed that a taper coil setup is able to produce a magnetic field close to 0.12 T.

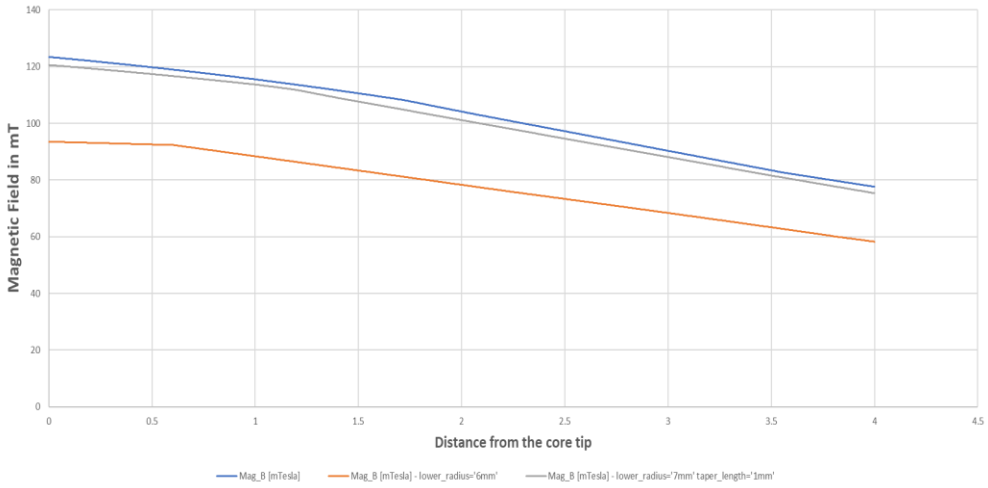

Figure 3.41 Comparison between cylindrical and taper coils with 2 different configurations

3.2.2.1.1 Conical Taper Coil - ON axis and OFF axis force analysis

A conical taper coil Fig. 3.42 is variation of conventional cylindrical coil with the radius away from the test specimen remaining constant but the face facing the test specimen has a lower radius which allows for better space efficiency. For this purpose, a coil dimension was considered with the outer radius being fixed at 20 mm and the radius of the taper end varying from 6 mm to 20 mm with a step increase of 0.5 mm with current density remaining constant.

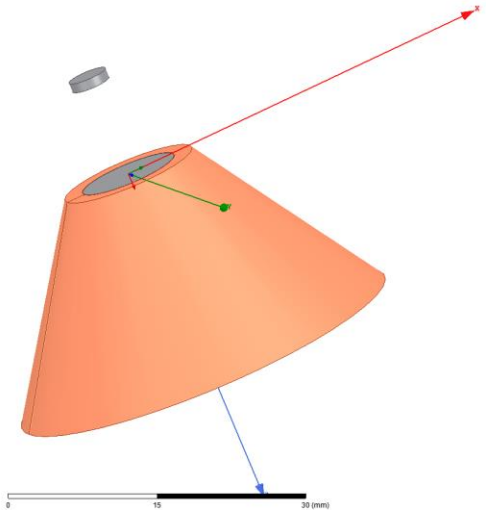

Figure 3.42 ON axis analysis of conical taper coil

Fig 3.41 illustrates how increase in taper significantly effects (almost linearly) the force on the test specimen. However, this does not conclude that conical taper coils are inefficient. The next stage in the conceptual design phase would work on the arrangement of coils in the 3D space and it would be the combined effect of the number of coils in the 3D space that would decide the efficacy of using conical coils and same would be the case with cylindrical taper coils analyzed in the next section. Fig. 3.44 illustrates how taper is varied over each pass in finite element analysis.

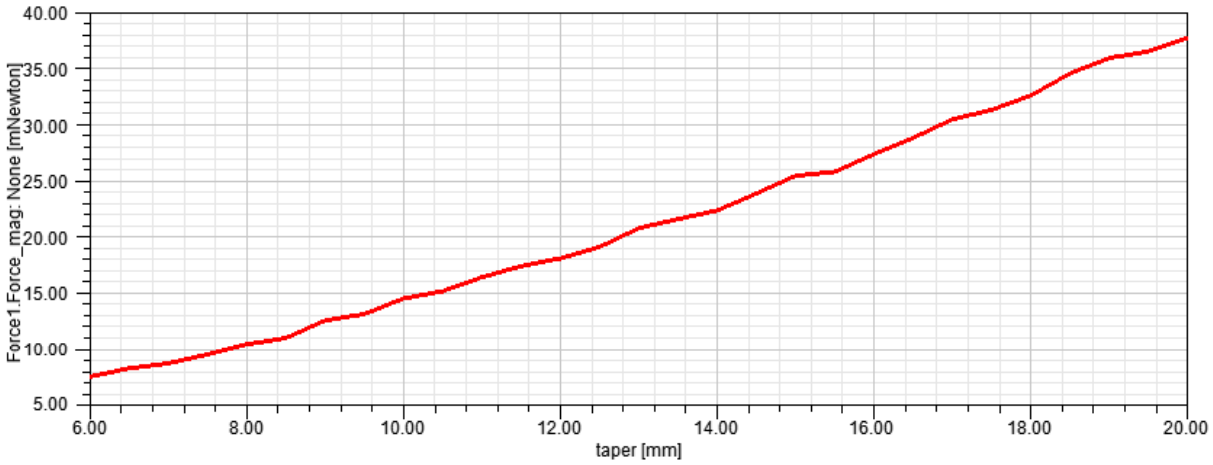

Figure 3.43 Effect of variation of Taper on ON axis force

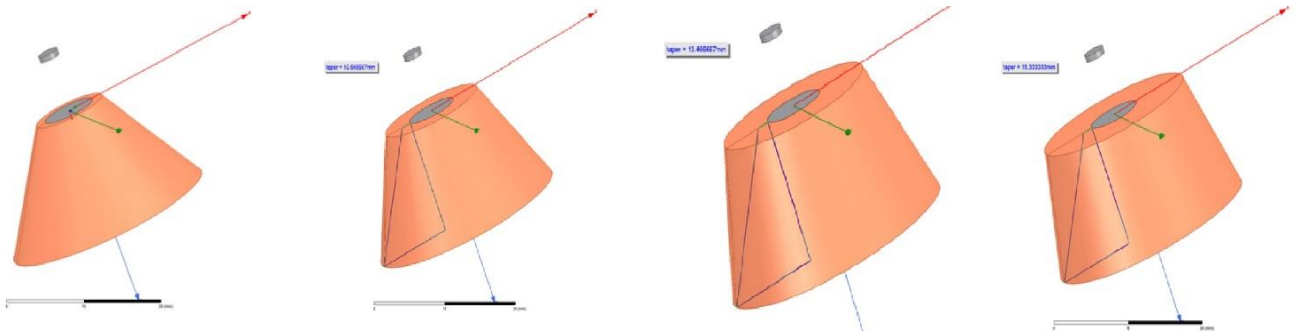

Figure 3.44 Snippets from parametric variation of horizontal taper

For OFF axis force analysis of the cone shaped taper coil the test sheet was always kept 4mm away from the outer edge of the larger diameter (Fig. 3.45), which is the same condition as analysed in the cylindrical case. Fig. 3.46 reveals the same trend as ON axis results. i.e force on the test sheet increases as taper increases, however, the increase in OFF axis case is not linear.

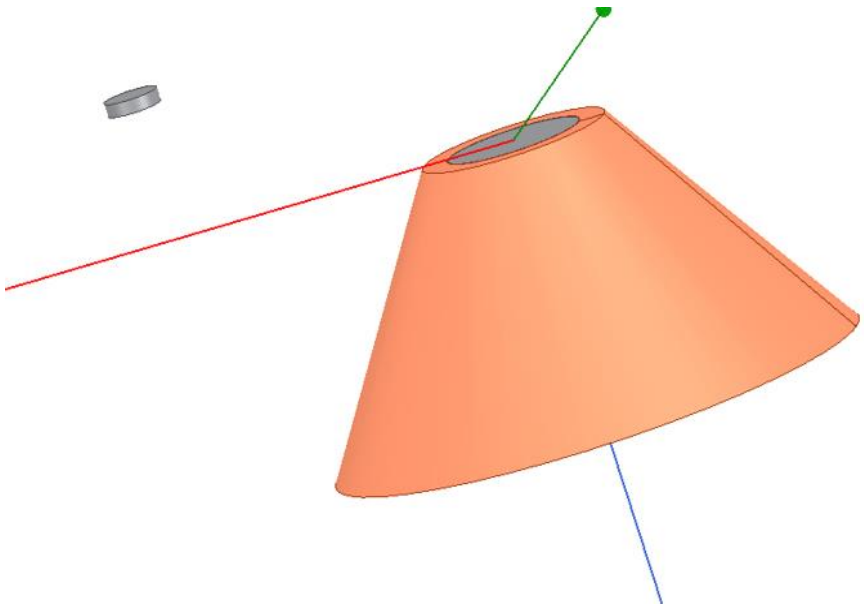

Figure 3.45 OFF axis analysis of conical taper coil

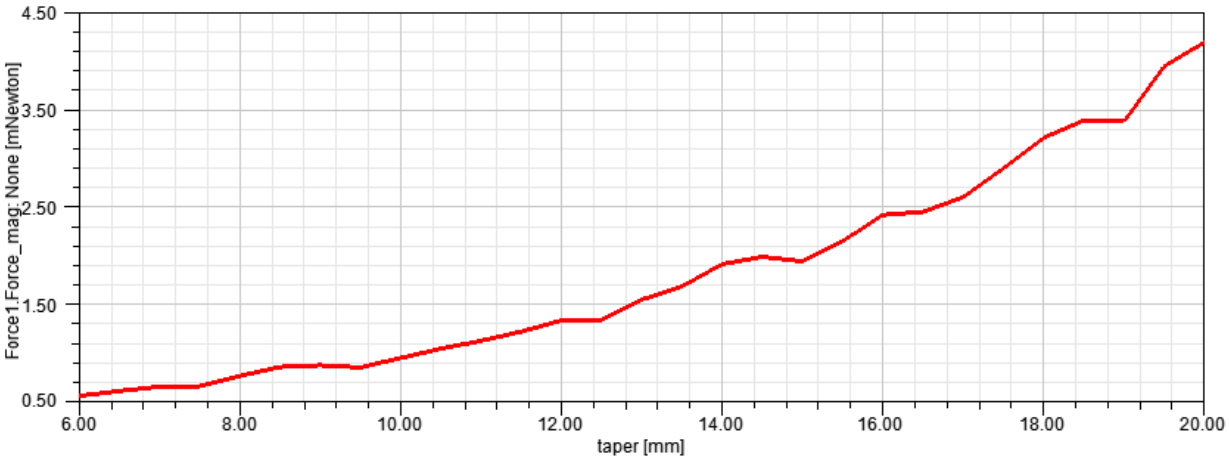

Figure 3.46 Effect of variation of Taper on OFF axis force for a conical coil

3.2.2.1.2 Cylindrical Taper Coil – ON axis and OFF Axis Force Analysis

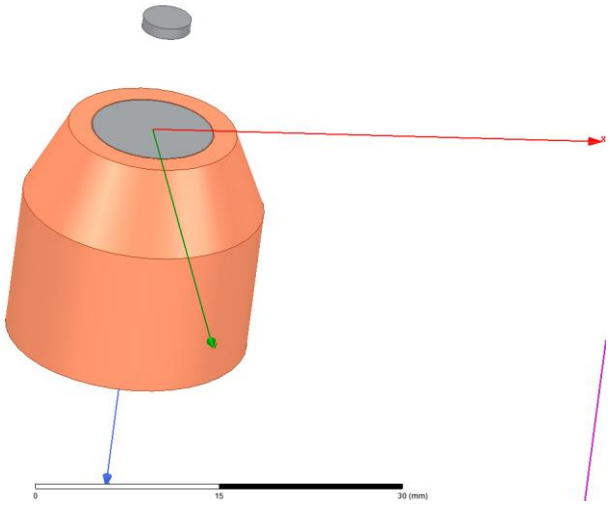

Figure 3.47 ON axis analysis of cylindrical taper coil

To minimize the effect of steep increase in force over the test plate as the horizontal taper increases another conceptual design was analyzed in Ansys Maxwell, where the outer diameter of the cylindrical

coil and the total length of the coil (20mm) were fixed and the only variable parameters were horizontal and vertical taper which is defined as the increase in length of the conical section and decrease in length of cylindrical section while keeping the total length constant (Fig. 3.51). Fig. 3.48 depicts how increase in horizontal taper results in increase in force on the test plate.

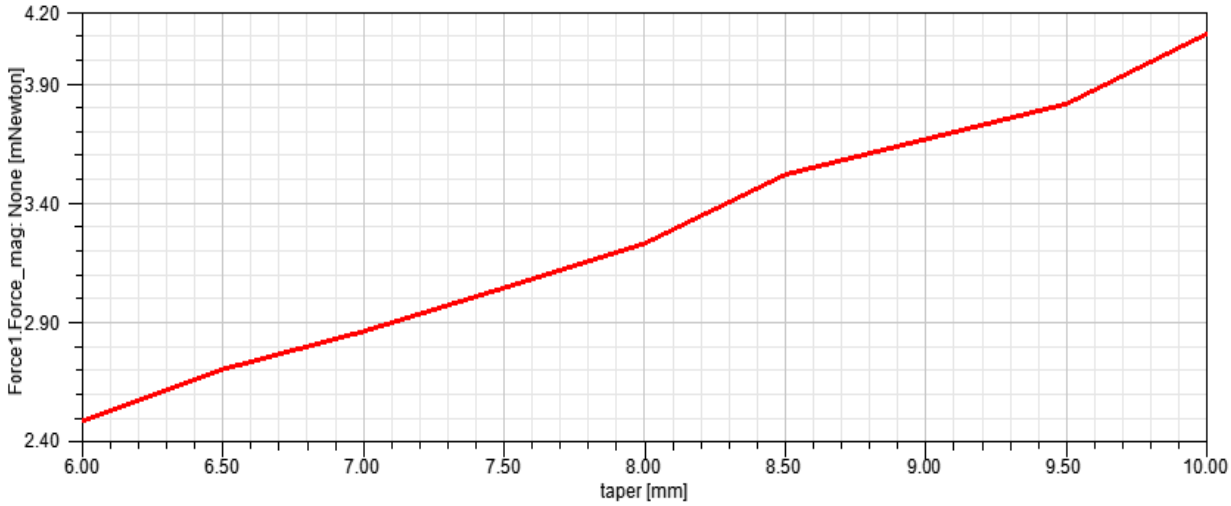

Figure 3.48 Effect of variation of Horizontal Taper on ON axis force

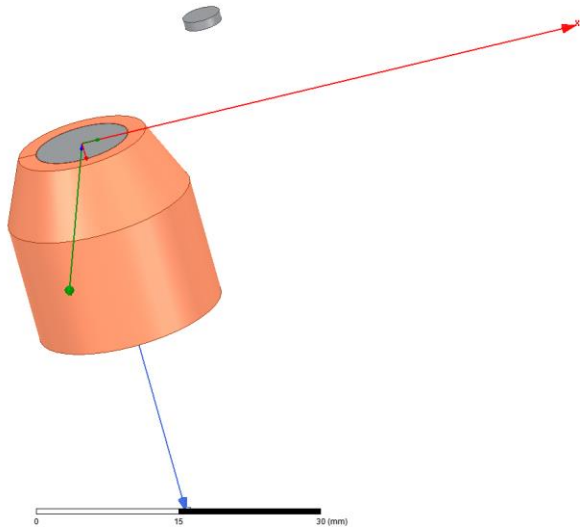

Figure 3.49 OFF axis analysis of cylindrical taper coil

Similar procedure was followed for OFF axis force analysis as done in conical taper coil, where the outer edge of the test plate is kept 4mm away from the cross section of the coil having maximum diameter, which in this case is the cylindrical coil. Fig. 3.50 illustrate the effect of increase in horizontal taper with each pass.

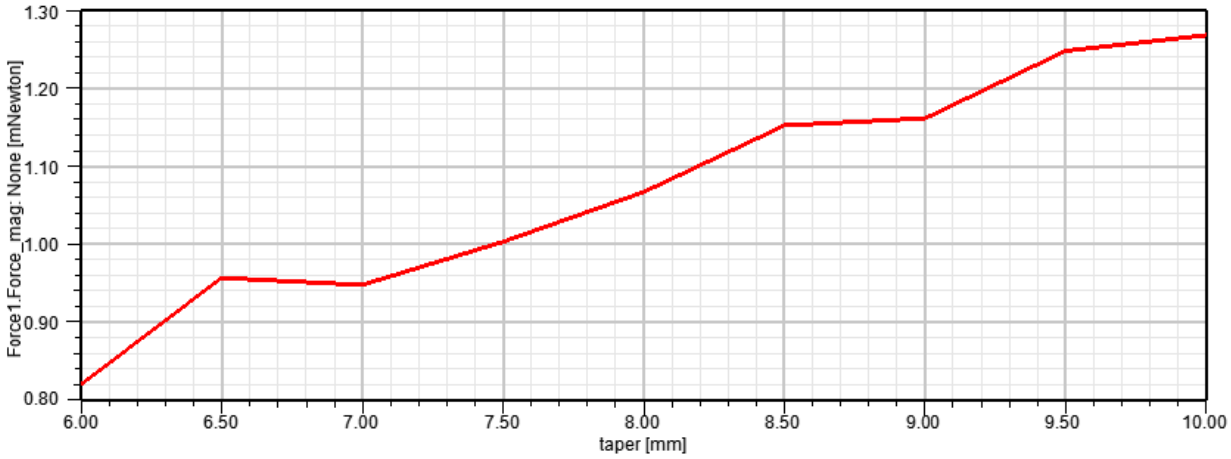

Figure 3.50 Effect of variation of Horizontal Taper on OFF axis force

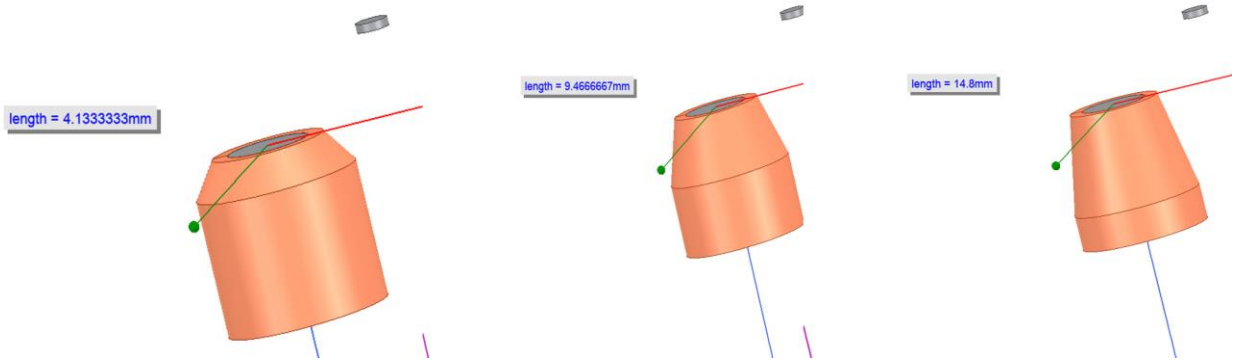

Figure 3.51 Snippets from parametric variation of vertical taper

Vertical Taper can be defined as the ratio of the conical section to the ratio of the cylindrical section while keeping the total length of the coil constant. Fig. 3.52 illustrates that as the length of the conical section increases the force on the test plate (OFF axis) decrease which is due to the fact the total number

of ampere turns would decreases (N*I; where N is the total number of turns and I is the current passing through each turn).

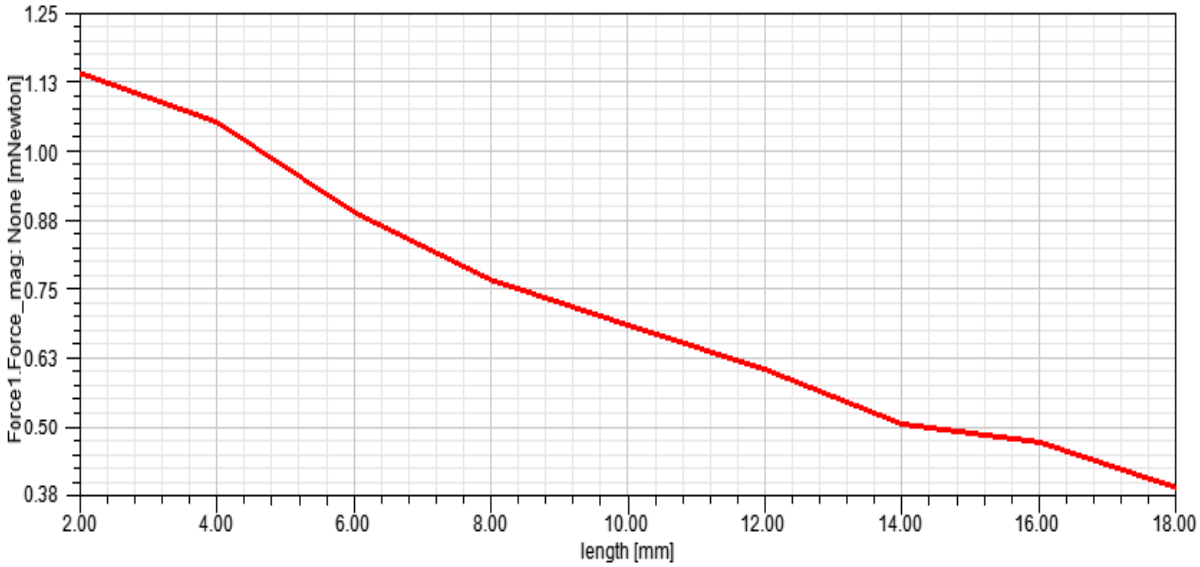

Figure 3.52 Variation of Vertical Taper for OFF axis force analysis

3.2.3 Design of Ferromagnetic Core Tip

The magnetic field gradient can be significantly magnified by selecting an appropriate core tip shape and core material. The geometry of the core tip is based on the length of the tip and its geometrical shape. This is a crucial design phase as core tip is used to direct and concentrate the magnetic flux lines in the working spot. Moreover, an extended core tip can also result in reduced leakage of magnetic flux. It has been observed that an appropriate core shape can increase the magnetic forces by about 10 times [27]. Iron was selected for the core tip as it has one of the highest relative permeability (4000) amongst metals. The length of the core tip is optimized based on the effect of core extension for the same constant distance between the core tip and the test particle-ON axis. It can be observed from Fig. 3.55 and Fig. 3.56 that an increase in core length sharply decrease the magnetic forces on the iron particle

(for both ON axis and OFF axis case). However, this does not suggest that the design should eliminate the idea of a core tip.

Moshe Stern et al. [27] compared the magnetic fields generated by 4 different tip shapes (Fig. 3.53) and found the following optimum core geometries for maximum magnetic force on the axis of the electromagnet based on the working gap (Fig. 3.54)

1. 0 - 0.17 mm: Conical pole tip
2. 0.17 - 7.5 mm: Parabolic pole tip
3. Above 7.5 mm: Flat-top pole tip

Since the aim of our project is to manipulate iron particles which are not always located on axial locations, it is required that the shape of the tip should be best suited for both axial and radial ranges, while maintaining high tangential and normal forces. It can be inferred from the above-mentioned study that using a flat pole tip also facilities our future for scalability of the entire setup. However, the study also found that at small distance (< 3 mm), parabolic pole tip generates about 10 times more force than its cubic counterpart.

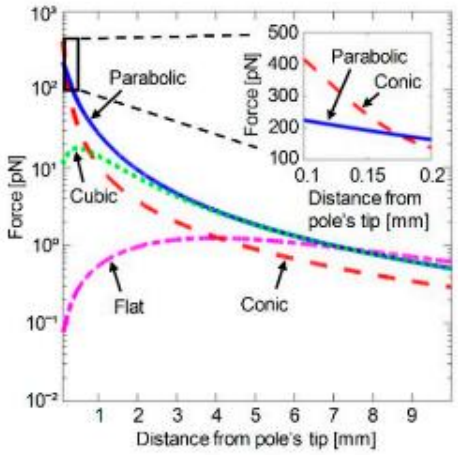

Figure 3.53 Variation of Magnetic force on the axis of an electromagnet with pole tip shape [27]

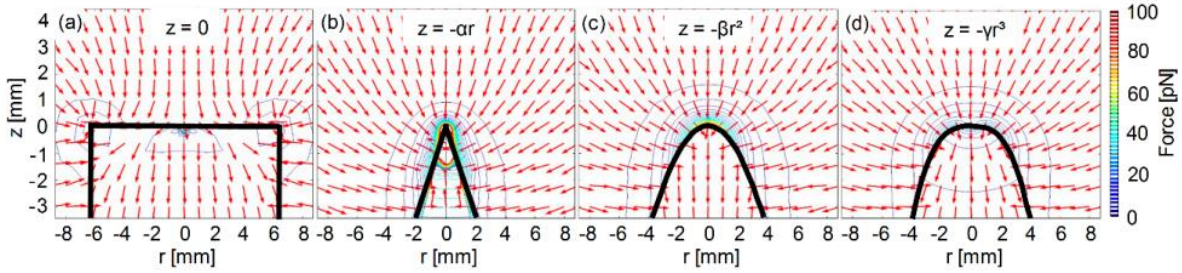

Figure 3.54 Force contour lines for flat, conical, parabolic, and cubic tip shapes [27]

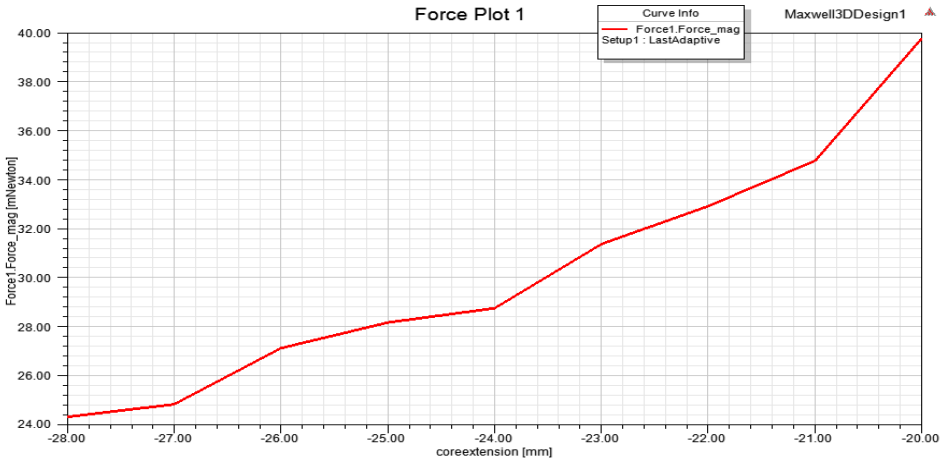

Figure 3.55 Effect of increase in core length (ON – axis) on magnetic force for a constant working gap

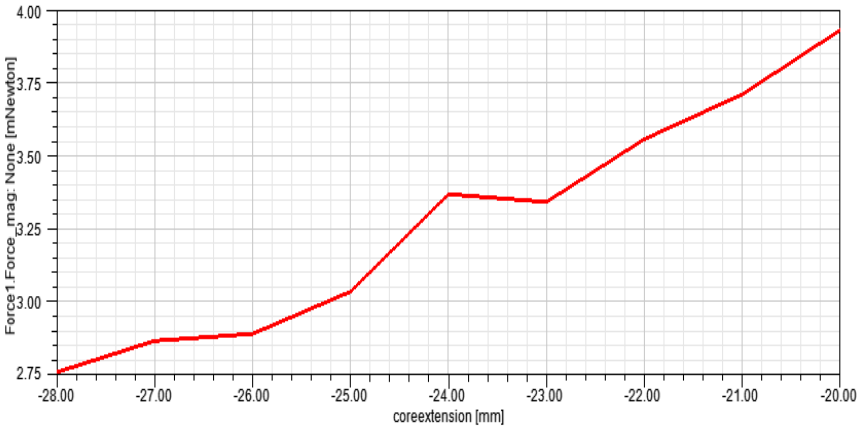

Figure 3.56 Effect of increase in core length (OFF – axis) on magnetic force for a constant working gap

Since, magnetic field and total magnetic force decrease with increase in core length for constant working gap (measured from the tip), it is important to determine the minimum length of core extension. This can be achieved by considering general coil design formula for a typical electromagnetic coil (l/lc=0.7~0.9) [28]. Where 'lc' is the length of the core and 'l' is the length of the coil, which was optimized as 41.4 mm for a coil with 16 mm outer radius and 5.75 mm inner radius.

Therefore,

$$\frac{l}{l_c} = 0.8$$

$$l_c = 51.5\ mm$$

3.2.3.1 Optimization of Core Tip Geometry for a Fixed Tip Length

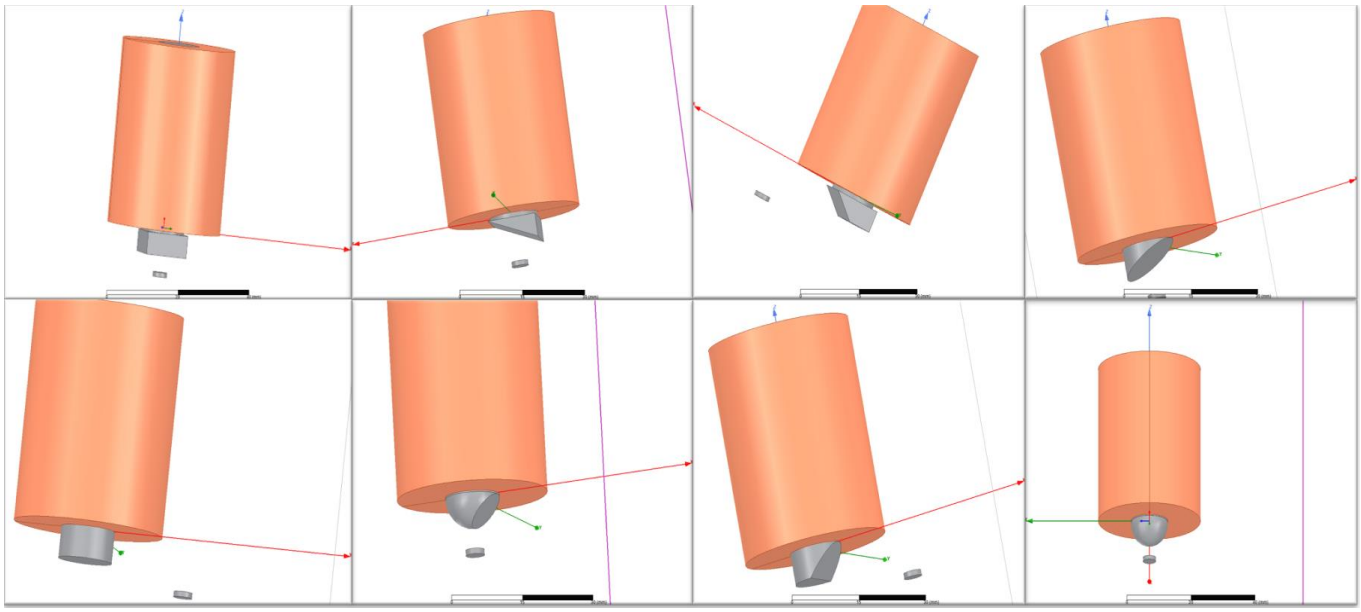

Figure 3.57 Pole tip shapes

After fixing the core length more than 8 core tip shapes were used to optimize the maximum uniform force field ON and OFF the axis for electromagnetic coil. Constant volume approach was also used to for comparison, where the volume of a tip shape is used as a benchmark (cylindrical in this case) and new designs having the same material volume are compared for force and field outputs. However, it was found that this approach is inefficient as it limits the innovation in geometry shapes. Therefore, constant length of the different core tips was chosen as a parameter to compare different tip shapes. The length of tip extension was obtained as 10 mm in the previous section. The results of tangential and normal forces are summarized in table 3. It can be observed that except cylindrical full chamfered case all other shapes result in a higher tangential force than normal forces for an OFF-axis test location. Cylindrical half chamfered produced the highest normal forces. This is because sharp edges/irregularities of the pole tip result in lower surface area which increases the number of flux lines per unit area to pass through. Moreover, it can be observed that a cylindrical tip shape produces the highest normal and tangential forces for the OFF-axis case and was among the top 3 shapes for normal force generation in ON-axis case as well. Hence, cylindrical core shapes are preferred as a symmetrical geometry which will enable us to make our design scalable, adaptable, and versatile to different surface profiles. Effect of fillet radius on flat face of a cylindrical tip is also studied in sub-section 3.2.3.2.

Table 3 Comparison of Normal and Tangential force for ON and OFF axis locations with varying tip geometries

configuration	Tangential Force - ON axis	Normal Force – O N Axis	Tangential Force - OFF axis	Normal Force – OFF Axis
Cylindrical full-chamfered	0.0197	0.25825	0.0153	0.017022
Spherical extension	0.0215	0.34867	0.0222	0.017882
Cylindrical extension	0.0012	0.3285	0.0296	0.020263
square Extension	0.0054	0.27449	0.0280	0.016896
Half cut Spherical Extension	0.0310	0.32743	0.0185	0.017479
Full cut Spherical Extension	0.0043	0.1923	0.0169	0.015635
Chamfered triangular cut- full	0.0124	0.21218	0.0226	0.016702
Chamfered triangular cut- half	0.0146	0.32526	0.0204	0.015674
Cylindrical half-chamfered	0.0056	0.41398	0.0183	0.014271

3.2.3.2 Effect of Fillet Radius on The Flat Face of The Cylindrical Core Tip

After selecting a cylindrical shape of core tip, we tried to reduce the sharp edges of the flat face as it causes high peaks of magnetic force and field values due to sudden reduction in surface area which increases the number of flux lines per unit area. This was done by adding a fillet to the flat face of the tip as shown in Fig. 3.58. However, as it can be inferred from Fig. 3.59 that fillet radius does not have a notable effect on the tangential and normal force components and it decrease the tangential forces at off-axis locations. Moreover, as it will be observed in the later sections that the peaks observed near the edges of the cylindrical tip are not observed in a tilted multi coil setup as the test particles are never subjected to these locations.

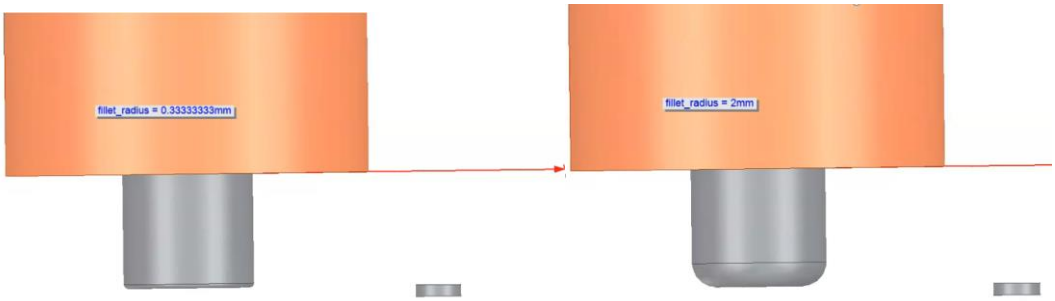

Figure 3.58 Variation in fillet radius of a cylindrical core tip

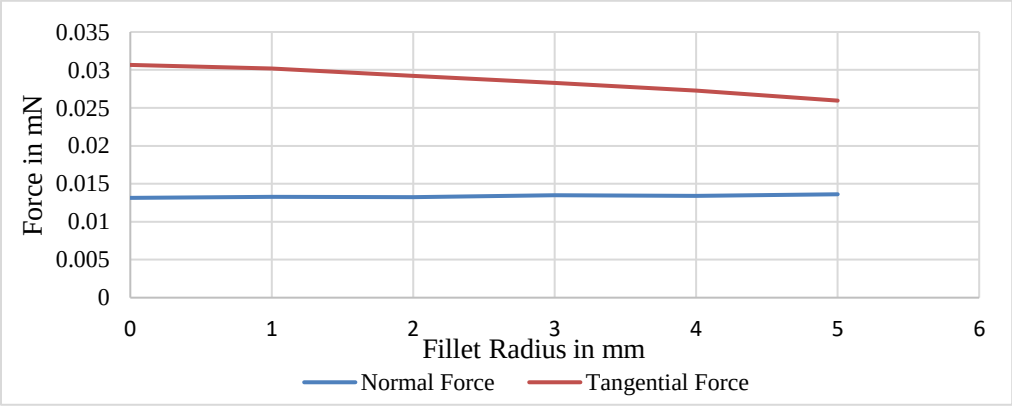

Figure 3.59 Effect of variation in fillet radius of a cylindrical core tip on the tangential and normal forces

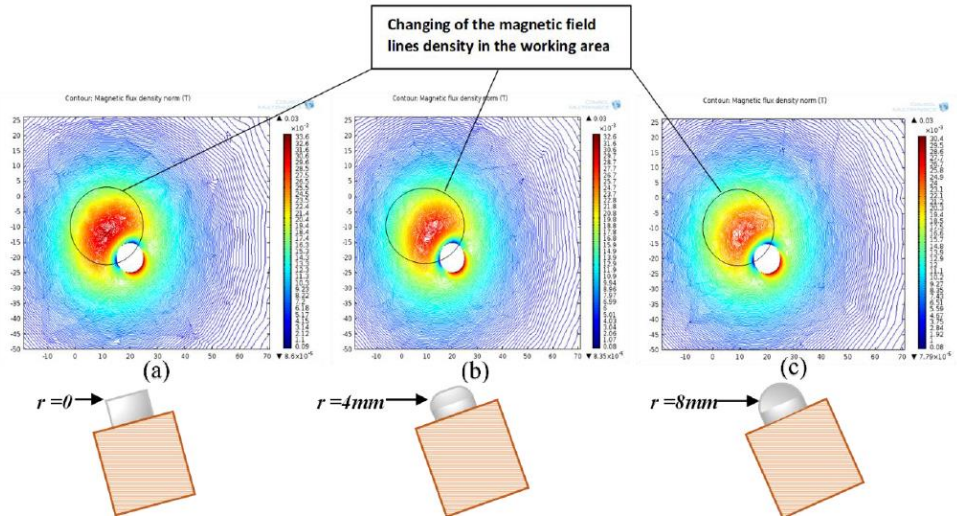

Figure 3.60 Effect of Fillet radius on magnetic flux density in the working area [5]

It is important to note that the results of this section agree with the experiments performed by Al-Dulami [5]. Fig. 3.60 illustrates of the magnetic field lines in the working area, it can be observed that increase in tip fillet radius decreases magnetic flux density in the working area, and fillet radius r = 0 results in highest magnetic field for both ON and OFF axis locations.

3.2.4 Optimization of Coil Inclination Angle

As it can be observed from our findings in the previous sub-sections that a test particle placed on the axis of an electromagnetic coil results in negligible tangential forces due to symmetry along the x and y axis resulting in cancellation of minor force components. Although a major part of the tangential force will be generated by the control law used to create a rotating magnetic field, we optimize our coil design for both ON axis and OFF axis locations. In this sub-section effect of inclination of the coil about a fixed point located at the bottom of the copper coil on its axis is studied to achieve higher normal and tangential forces. As it can be observed from Fig. 3.61 and will also be reconfirmed in the subsequent sections that a range of angles between 45-55 degrees produces the highest amount of total forces while maintaining high tangential and normal components. These angles are further analyzed in a multi coil cylindrical and taper setup, and it is interesting to note that the optimized range remains the same.

Case	Normal Force (Maximum for cases with Tilt)	Tangential Force (Maximum for cases with Tilt)	Optimum Tilt angle
OFF axis + Tilt	29.119 mN	46.34 mN	51^0

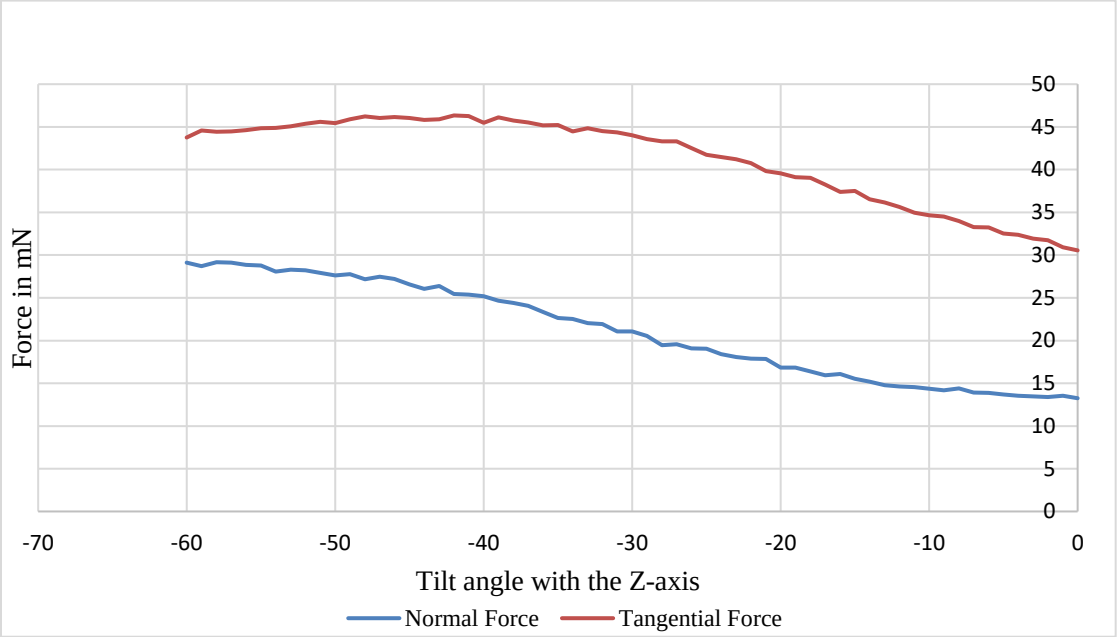

Figure 3.61 Variation of Normal and Tangential forces with tilt angle for a cylindrical tip

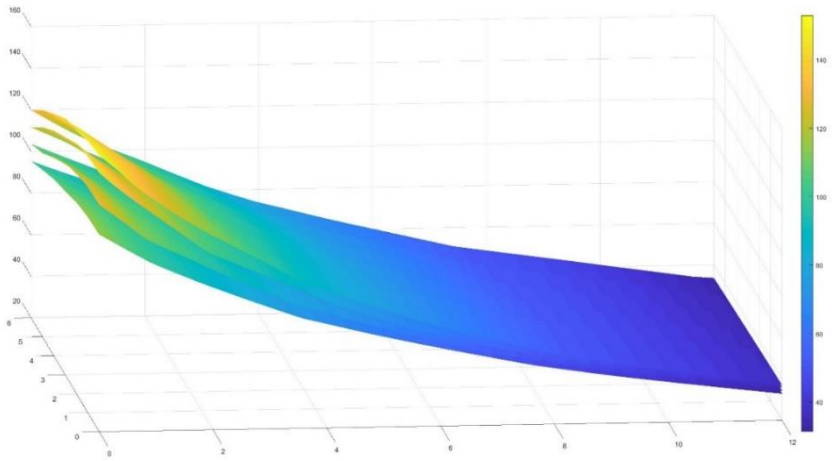

Figure 3.62 Variation of magnetic field on a horizontal rectangular sheet due to varying angles of inclination – Color plot[1]

1 Z-axis represents magnetic field in mT

Certain tip shapes were separately simulated for coil angle inclinations, and it was found that angle of inclination to generate high tangential and normal forces is a function of core tip geometry. A case of cylindrical chamfered tip (Fig. 3.63) is presented below with an optimum inclination angle of 30^0 as compared to 50^0 in the case of cylindrical tip.

Case	Normal Force (Maximum for cases with Tilt)	Tangential Force (Maximum for cases with Tilt)	Optimum Tilt angle
OFF axis + Tilt	22.06 mN	33.85 mN	30^0

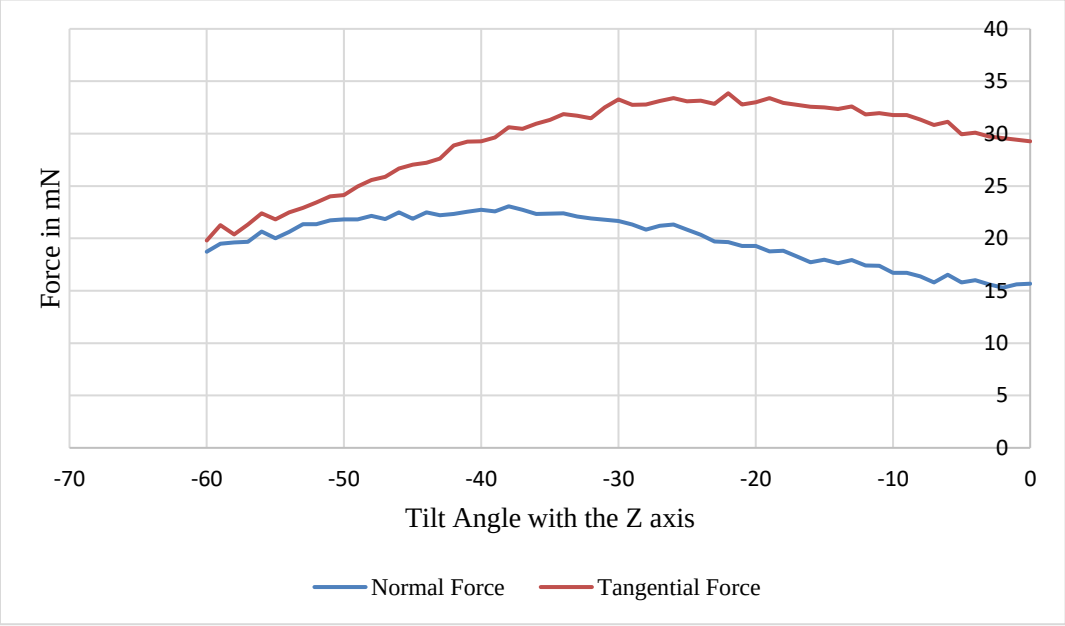

Figure 3.63 Variation of Normal and Tangential forces with tilt angle for a cylindrical chamfered tip

XY-axis represents the horizontal distance in mm

3.2.5 Comparison of a Square coil with a cylindrical coil

Square coil is another commonly used coil shape. A square coil (Fig. 3.64) with side length equal to the diameter of the cylindrical coil was simulated for comparing the magnetic field on the axis and on a horizontal line (1 mm below the flat face of the tip spanning across the tip diameter + 1.25 mm on both sides) with a cylindrical coil and core shapes.

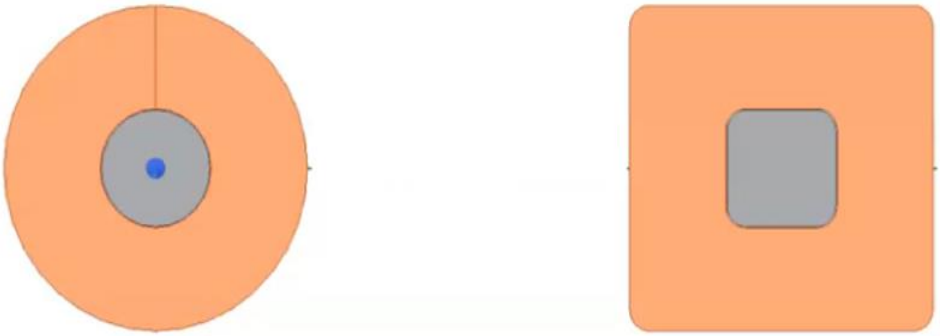

Figure 3.64 Comparison of a Square and Cylindrical Coil Shapes

Moreover, fillets we applied to the edges of the core and the coil to see the effect of transition towards a cylindrical coil shape. Fig. 3.65 and Fig. 3.66 illustrate the reduction in magnetic field with increase in fillet radius on a vertical (on the axis of the coil, starting 1mm below the flat face) and horizontal line (1mm below the flat face).

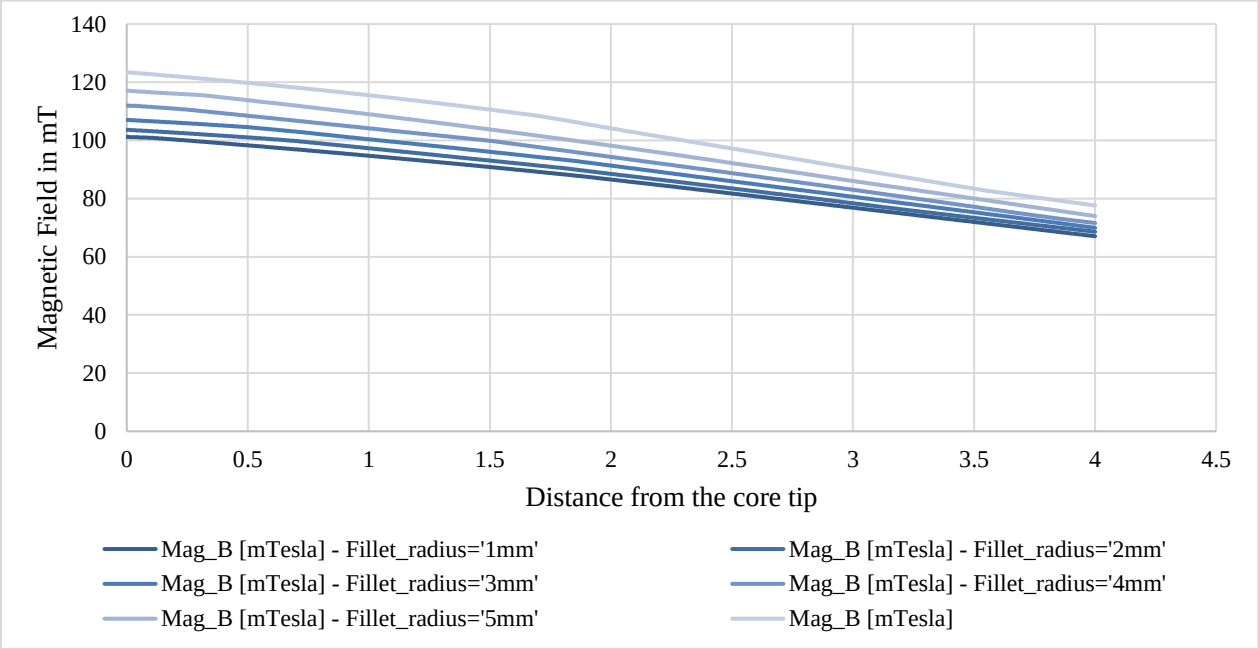

Figure 3.65 Effect of Fillet radius on the magnetic field on the vertical line on the axis of the coil, starting 1mm below the flat face

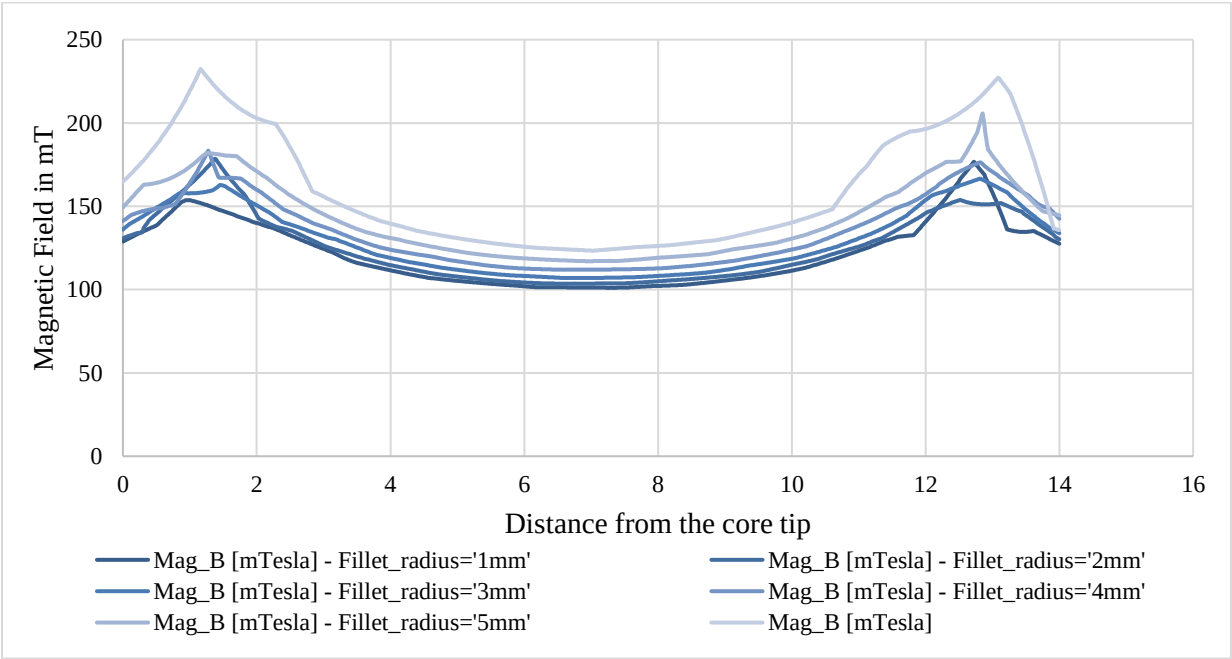

Figure 3.66 Effect of Fillet radius on the magnetic field on a horizontal line on the axis of the coil, 1mm below the flat face

Hence, it can be inferred that a cylindrical coil produces a higher magnetic field as compared to a square coil for both ON and OFF axis locations. It was be observed that a current density (J) of 12 A/m^2 is suitable for producing a uniform magnetic field of around 0.1 T on the axis of the coil and 0.23 T near the core tip edges. As it will be illustrated in further sections that a multi coil setup inclined at an optimized angle is able to generate similar magnetic fields (0.2 T) at 1-1.5 mm machining gaps.

3.2.6 Magnetostatic analysis of Multiple cylindrical coils

A single coil cannot generate a rotating magnetic field and hence is unable to create the griding pressure necessary for surface finish. Adjacent coils in a multiple coil arrangement can be energized using a control model to generate a rotating magnetic field. However, before designing a control law it is crucial to simulate the magnetic field at various locations due to a multi-coil setup and understand the forces experienced by the iron particle with varying polarities, current densities, working gaps, and angle of inclinations, while maintaining high tangential and normal forces at all times. The following magnetostatic analysis is based on the forces experienced by a particle at different locations in the working area. Please note that the forces in the following sections are illustrated when all the coils are activated at once using a DC excitation, however, the polarities and current densities can be different. Moreover, at instances when the particle is along the axis of the coil or in the vicinity of the core tip it can be assumed that only one coil is energized as the effect of other coils on the iron particle is negligible due to increased working gap. Since, the iron particles in flexible magnetic abrasive brush are attracted towards each other along the magnetic lines of force due to dipole-dipole interaction it is also crucial to understand the contour plots of magnetic field and gradient of magnetic field in these cases.

3.2.6.1 Magnetostatic Analysis of Two Cylindrical Coils

The following analysis is performed for a set of 2 coils at varying distances apart with design parameters such as current, coil separation, location of test particle and polarity. The coils are inclined at an angle of 50^0 with the vertical as optimized in the previous sections. The analysis has been divided into two cases based on the polarities of the coil (Fig. 3.67 and Fig. 3.68). Please note that a single electromagnetic coil will always attract an iron particle irrespective of the coil polarity. However, changing the polarity of two coils alters the path of magnetic flux lines. The magnetic forces are measured along a line 10 mm below the coils.

It can be noted that only in the case of similar polarity the tangential forces are inherently higher than the normal forces. However, the forces in the case of opposite polarities are around 100 mN higher than the same polarity case. Lower tangential than normal forces in the case of opposite polarity is not a limitation in coil design as controlled activation of coil will also add significantly to the component of tangential forces.

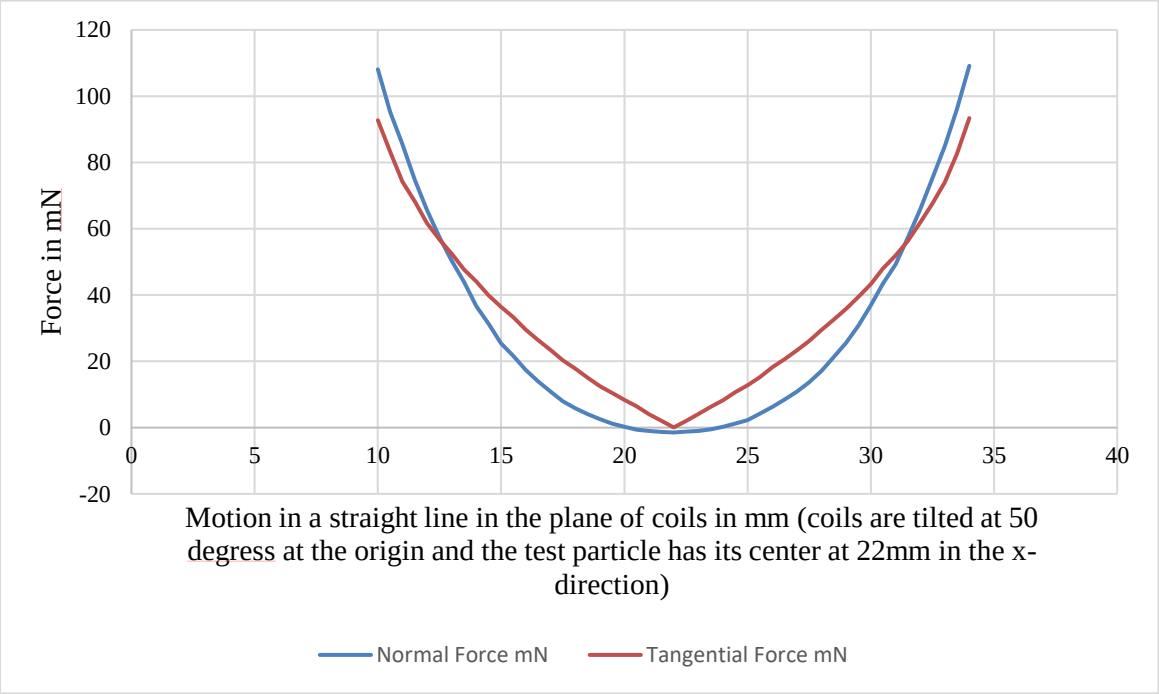

Figure 3.67 Force plot when both coils have same polarity

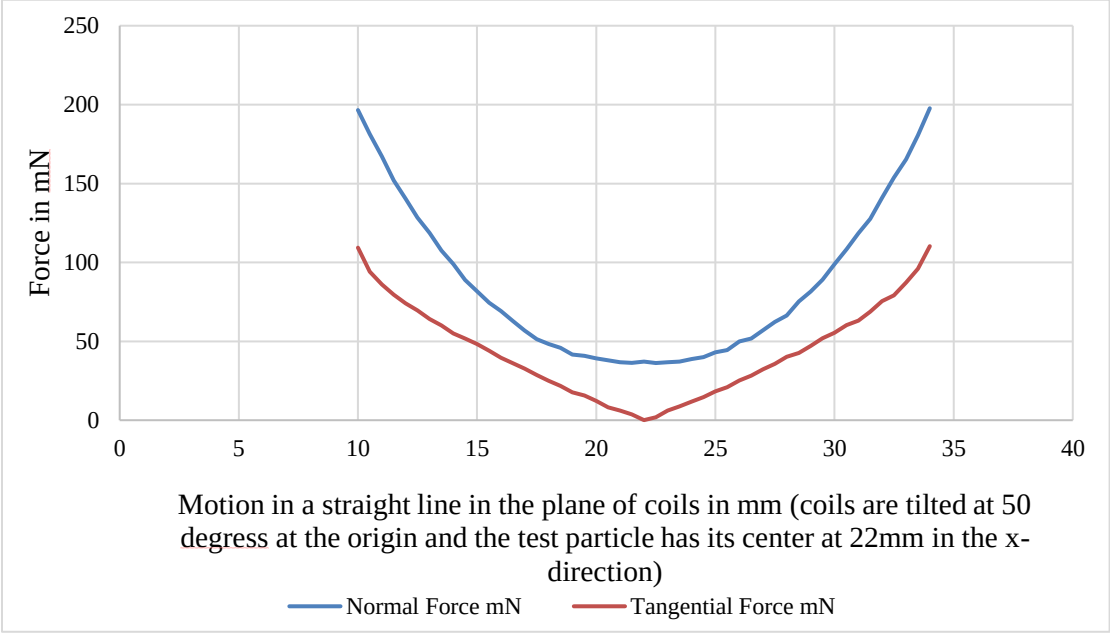

Figure 3.68 Force plot when both coils have opposite polarity

Also, it can be observed that the tangential forces almost remain the same in both the graphs and only the parabolic normal force curve shifts upward. Moreover, since both the coils produce attractive forces irrespective of the coil polarities, the midpoint results in cancellation of tangential force components.

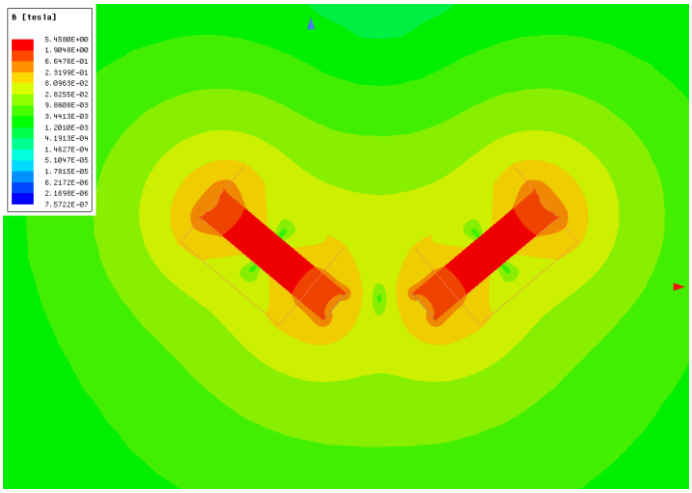

Figure 3.69 Magnetic field contour/color plot due to two coils having same polarity, in the same plane 22 mm apart

Now, to get an idea of the magnetic field in a direction perpendicular to the plane of coils, magnetic force is plotted for the case of same and opposite polarity along the centerline of the two-coil setup (Fig. 3.70 and Fig. 3.71). It can be observed that for the case of two coils with opposite polarities the normal forces are more than 30 mN higher than the case with similar polarities.

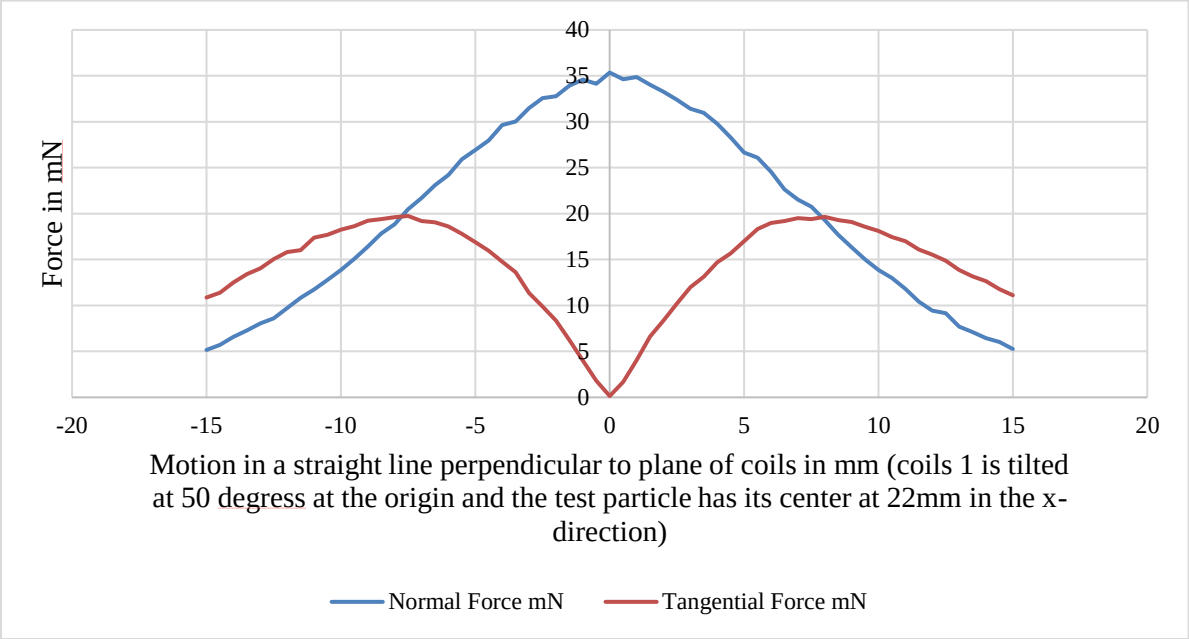

Figure 3.70 Total force on a test particle along the center line of the two-coil setup with opposite polarities

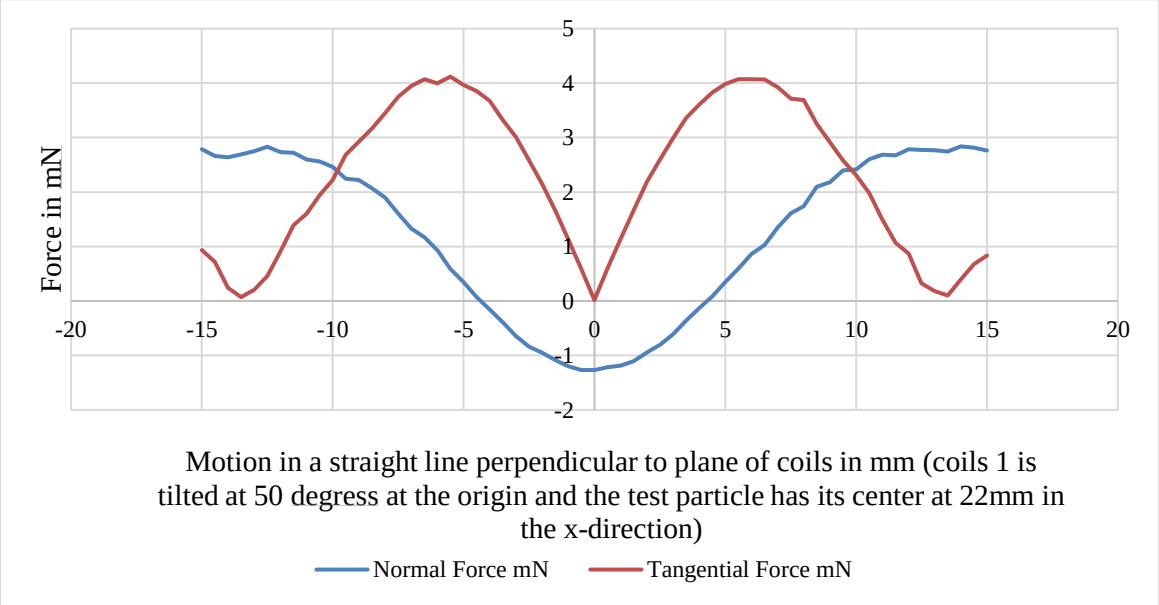

Figure 3.71 Total force on a test particle along the center line of the two-coil setup with same polarities

To gain an understanding of the variation of magnetic field and the gradient of magnetic field between two coils of same polarity the above simulations were also plotted on a rectangular sheet. However, Ansys does not provide the ability to plot magnetic field on a rectangular sheet, this is done by plotting the magnetic field (Fig. 3.73) and its gradient (Fig. 3.74) on equally spaced line along the plane containing the two coils at 10 mm below the coil (Fig. 3.72).

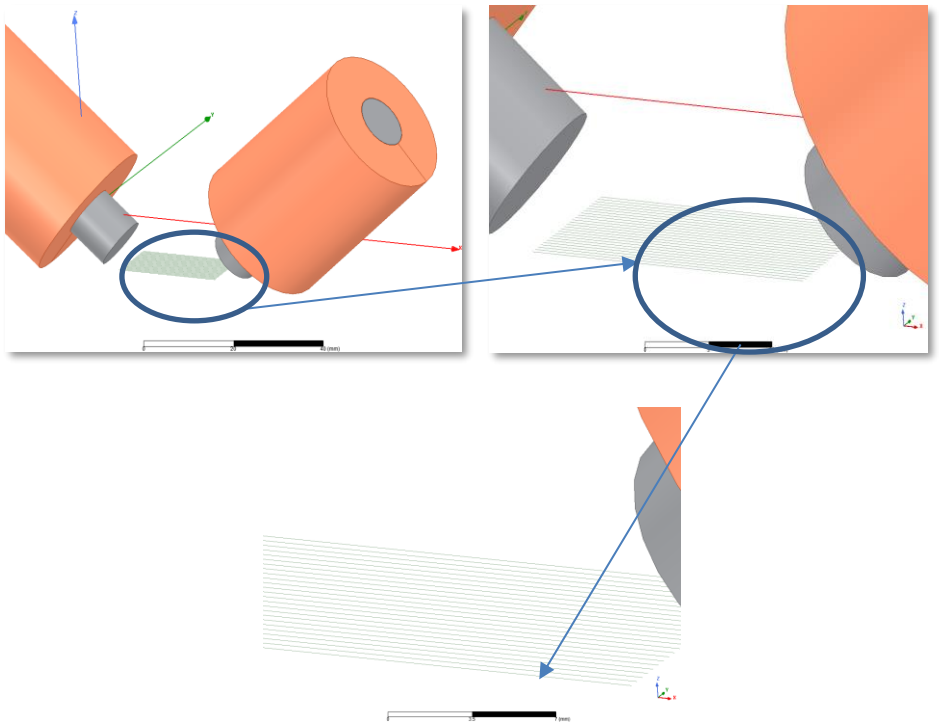

Figure 3.72 Equally spaces lines used to represent a sheet for plotting magnetic field and gradient B

Therefore, it can be observed that the magnetic field between the two coils not only depends on the magnitude of current but also on the direction of current. Fig. 3.75 and Fig. 3.76 highlight the magnetic fields between two coils due to same and opposite polarity with varying current densities. Opposite polarities, (Fig. 3.75) result in higher magnetic field and lower peak drops towards the middle. However, for the case of same polarity (Fig. 3.76) the magnetic field is about 25 percent lower at the extreme ends and this difference increase as the test particle moves away from the coil.

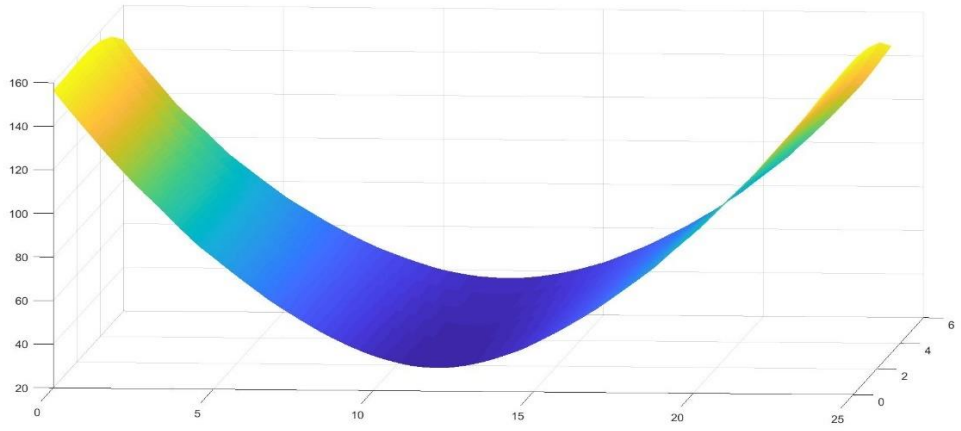

Figure 3.73 Magnetic field on a rectangular plane between two coils with same polarity

X-axis – distance in x direction, Y-axis: Distance in y direction; Z axis: MagB

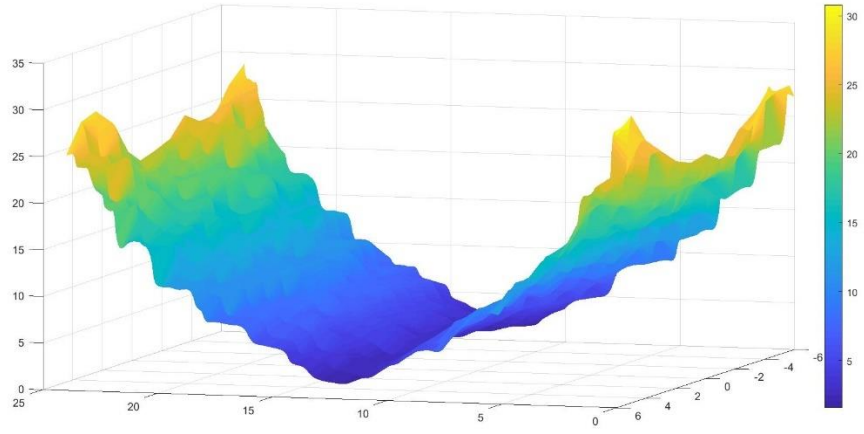

Figure 3.74 Gradient of magnetic field on a rectangular plane between two coils with same polarity

X-axis – distance in x direction, Y-axis: Distance in y direction; Z axis: GradB

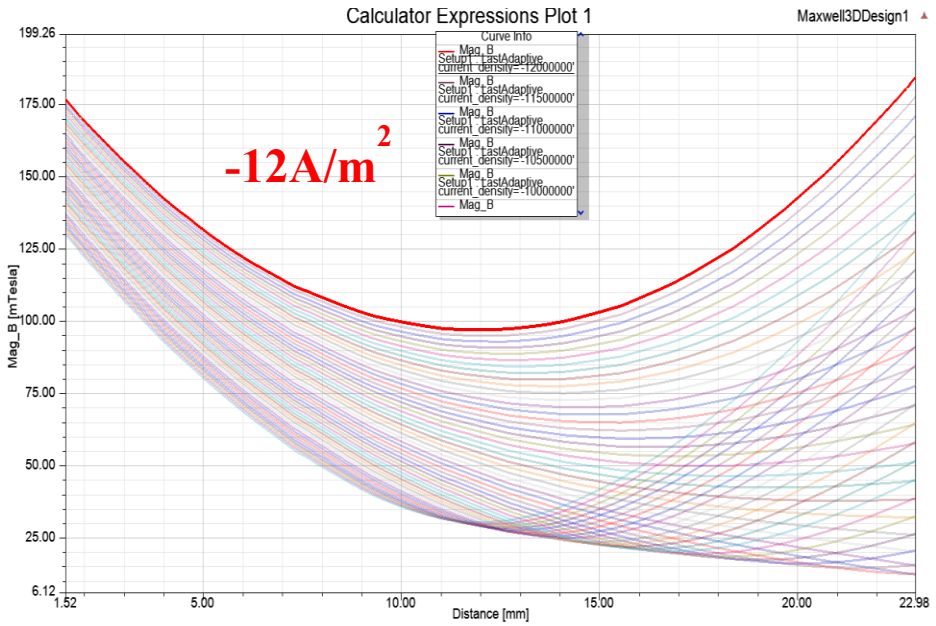

Figure 3.75 Magnetic field between the two coils with varying current density (opposite polarity)

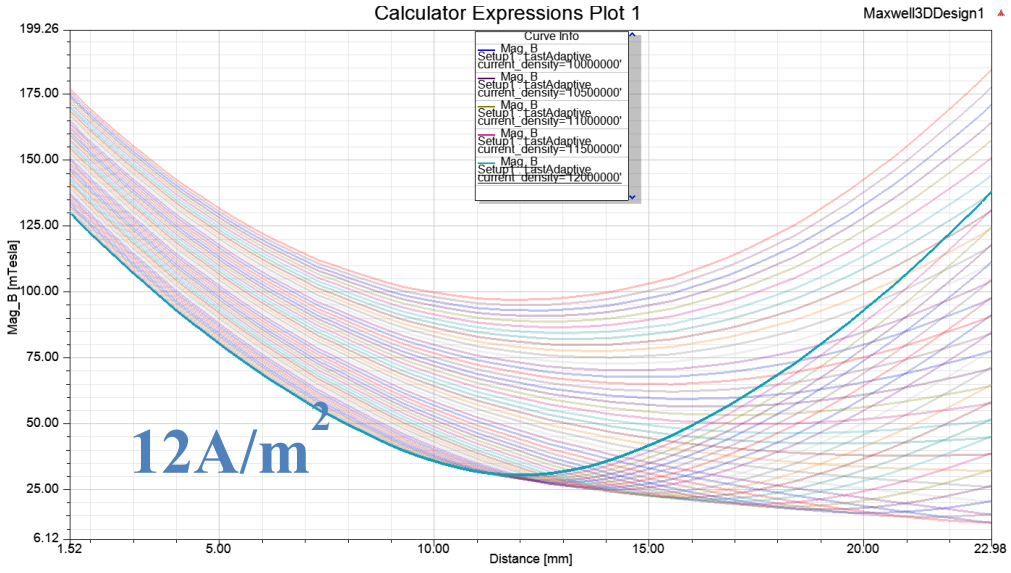

Figure 3.76 Magnetic field between the two coils with varying polarity (similar polarity)

3.2.6.1.1 Transition from Cylindrical to Spherical Test Particles

As we move further with the optimization process, it was realized that due to the small size and sharp edges at flat faces of the test particle, meshing becomes a challenging issue in a cylindrical disk. Moreover, due to its lack of symmetry comparing results at different locations due multiple coils is inefficient. Therefore, a spherical test particle is selected to overcome the limitations due to its symmetrical shape, ease of scalability and no sharp edges. Hence, all finite element analysis from this section onwards are based on a sphere of radius 1mm instead of a cylindrical of radius and height 1.1 mm. It must be noted that both the particles have the same volume and material. However, since all the previous simulations were performed using cylindrical test particles, it is important to compare the force components on both the particles. Fig. 3.77, Fig. 3.78 and Fig. 3.79 illustrate the force comparison between two particles. For this purpose, both the particles are placed at the same vertical location below the axis of the coil and are moved horizontally to a distance of 35 mm. Since the coil and the test particle is symmetric across y axis the forces in the y direction are negligible (μN range). It can be clearly observed that the force components for both the shapes produce similar trends with notable but minor differences.

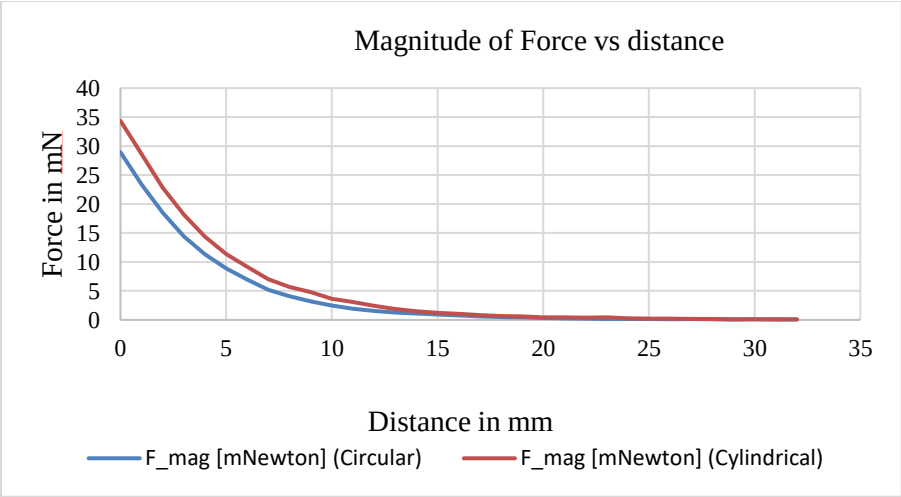

Figure 3.77 Comparison of total force for a cylindrical and a spherical particle with the same volume

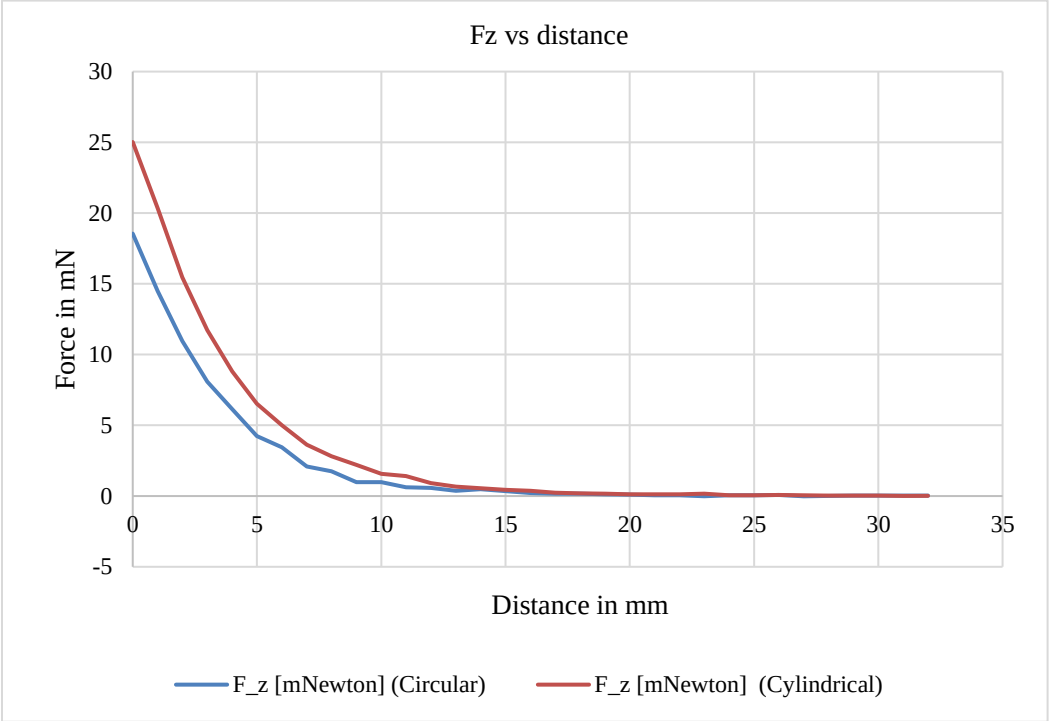

Figure 3.78 Comparison of Fz for a cylindrical and a spherical particle with the same volume

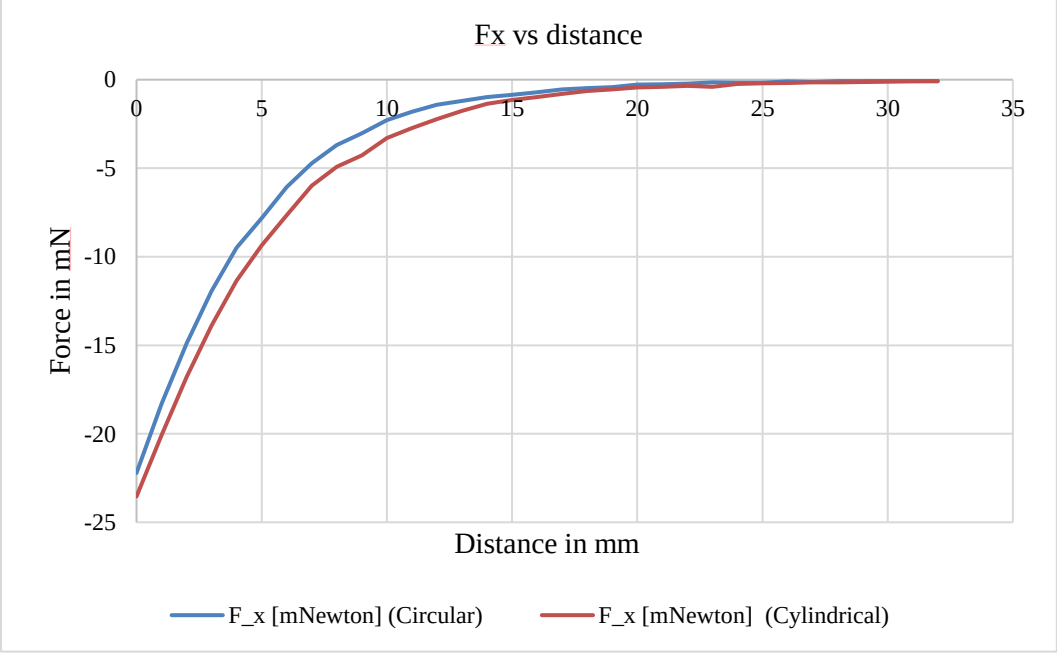

Figure 3.79 Comparison of Fx for a cylindrical and a spherical particle with the same volume

3.2.6.2 Three Coil Setup

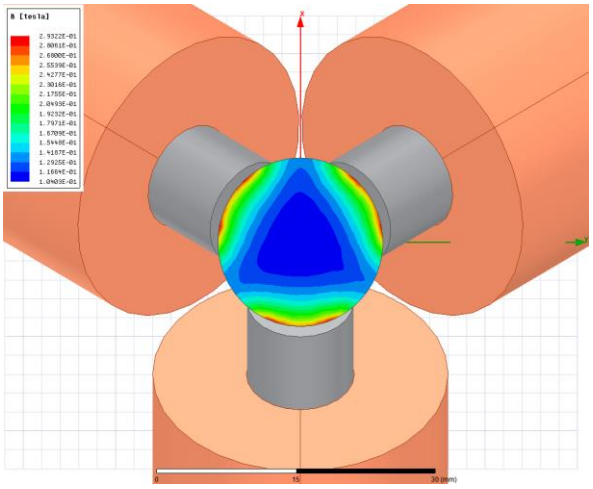

Figure 3.80 Color Plot of magnetic field due to 3 simultaneously activated coils

Fig.3.80 represents the magnetic field contour produced by 3 coils having the same current density and direction. The red and orange areas represent the required magnetic field of about 0.2 -0.3 T. The colored circular disk is 1.5 mm below the last plane of the coil setup cross-section. It can be observed that the blue regions are areas of less than 0.1 T and may result in loss of manipulation/control of iron abrasive particles. The goal of the following sections is to optimize a multi coil design which eliminates/reduces low field points in the magnetic field contour. This can be achieved by either increasing the power supply to the electromagnet or by optimizing the distance between coils. Moreover, it is evident from the above image and Fig. 3.82 that OFF axis optimization of coil dimensions was a crucial step in optimizing dimensions for a single electromagnet. Fig. 3.91 illustrates circular rings representing varying machining gaps.

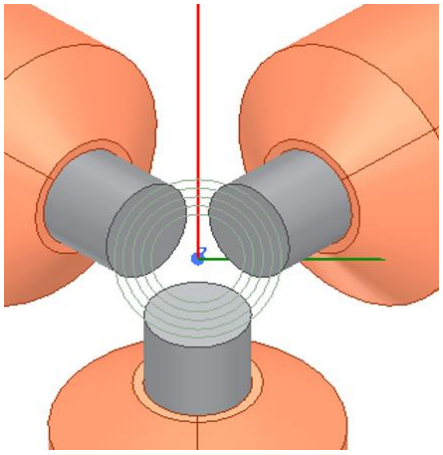

Figure 3.81 Circular rings used to represent varying machining gaps

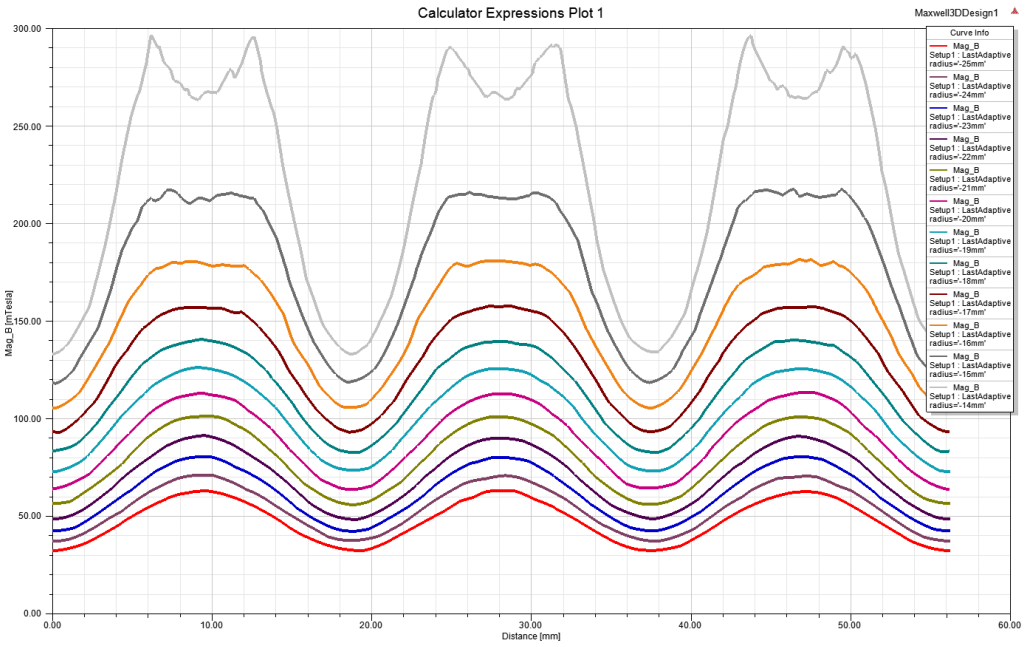

Figure 3.82 Magnetic Field on circular tracks represented in Fig. 3.81

For FEA simulation of a static magnetic field generated by 3 electromagnetic coils, 2 polarity cases are considered. Case I assigns all coils with same polarity and current density, case II assigns alternate polarity to the coils (+-+). It must be noted that it is the nature of polarities that affects the force output

and not the signs of the actual polarity i.e. +-+ configuration is the same as -+-. Hence, to avoid excessive test runs only relevant cases are considered.

a. Case I

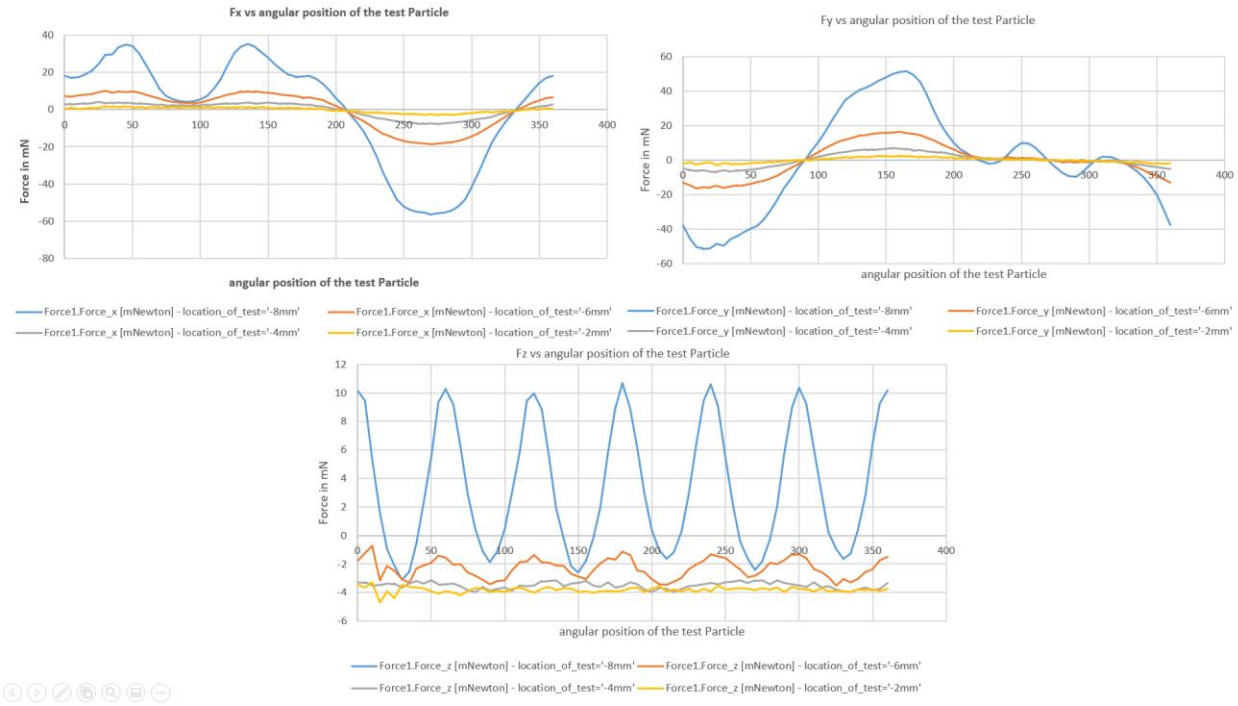

Figure 3.83 Force components on an iron particle on a circular track with variable radii also known as working gap[2] due to 3 coils with same polarity

Fig. 3.83 represents the force components on an iron particle in a 3-coil setup. It can be clearly observed that at 1 mm distance (blue line) highest magnetic forces are experienced. Moreover, one of the most important parameters for multi coil setup optimization is the magnitude of tangential and normal forces.

[2] -8 mm represents a working gap of 1 mm and it increases in the order of 6mm, 4mm and 2 mm. These values are the radii of the circular track followed by the test particle to record the magnetic force. The same notation will be followed for all multi-coil cases.

Fig. 3.84 illustrates that for each working gap/track radius the magnitude of tangential forces is higher than the normal forces. However, it must be noted that the magnitude of magnetic fields is very less as compared to the minimum required magnetic field of about 0.2 T.

A 4-coil setup also produces similar results for same and alternate polarity setting. Therefore, it can be concluded that due to higher force, alternate polarity setting is more favorable. Moreover, since the magnetic field lines travel from north to the south poles, MAPs will form high strength chains in the case of alternate polarity setting.

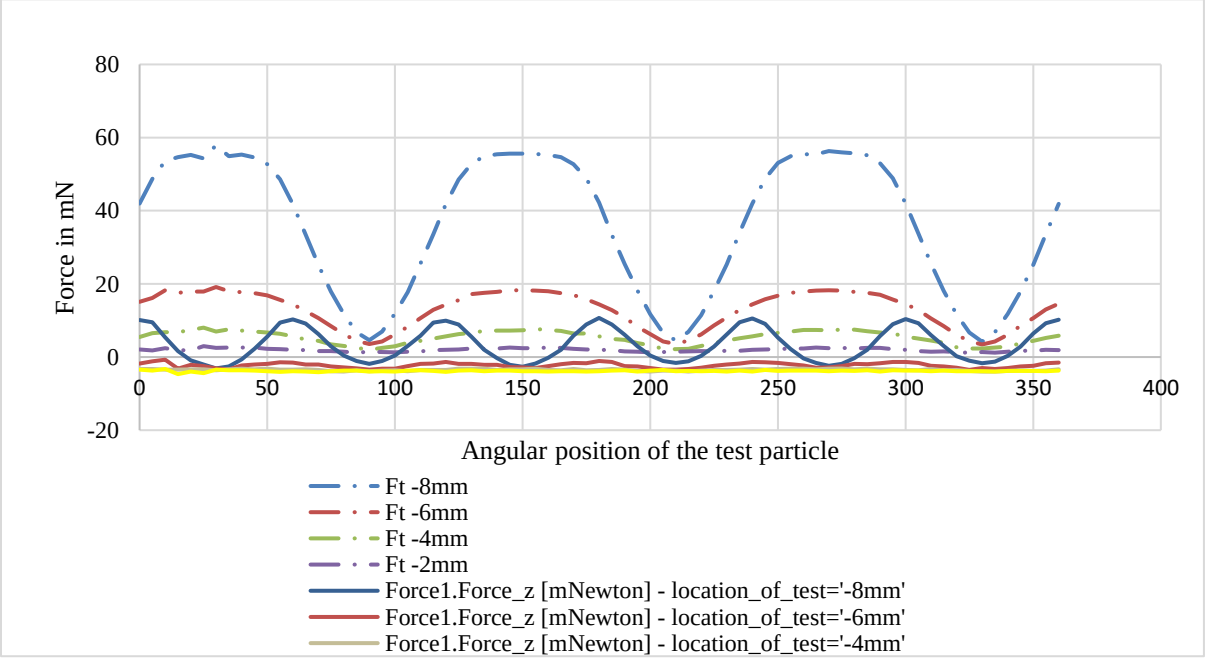

Figure 3.84 Tangential and Normal forces vs angular position of the test Particle (3 coils-same polarity)

As mentioned in sub-section 3.2.2.1 the mirror distance increases with the number of coils. In general, for the optimized dimensions the mirror distance increases by about 5 mm for each new coil addition. Therefore, following are the mirror distance for different coil setups:

1. 3 Coil: 14 mm
2. 4 Coil: 20 mm
3. 5 Coil: 25 mm
4. 6 Coil: 31 mm

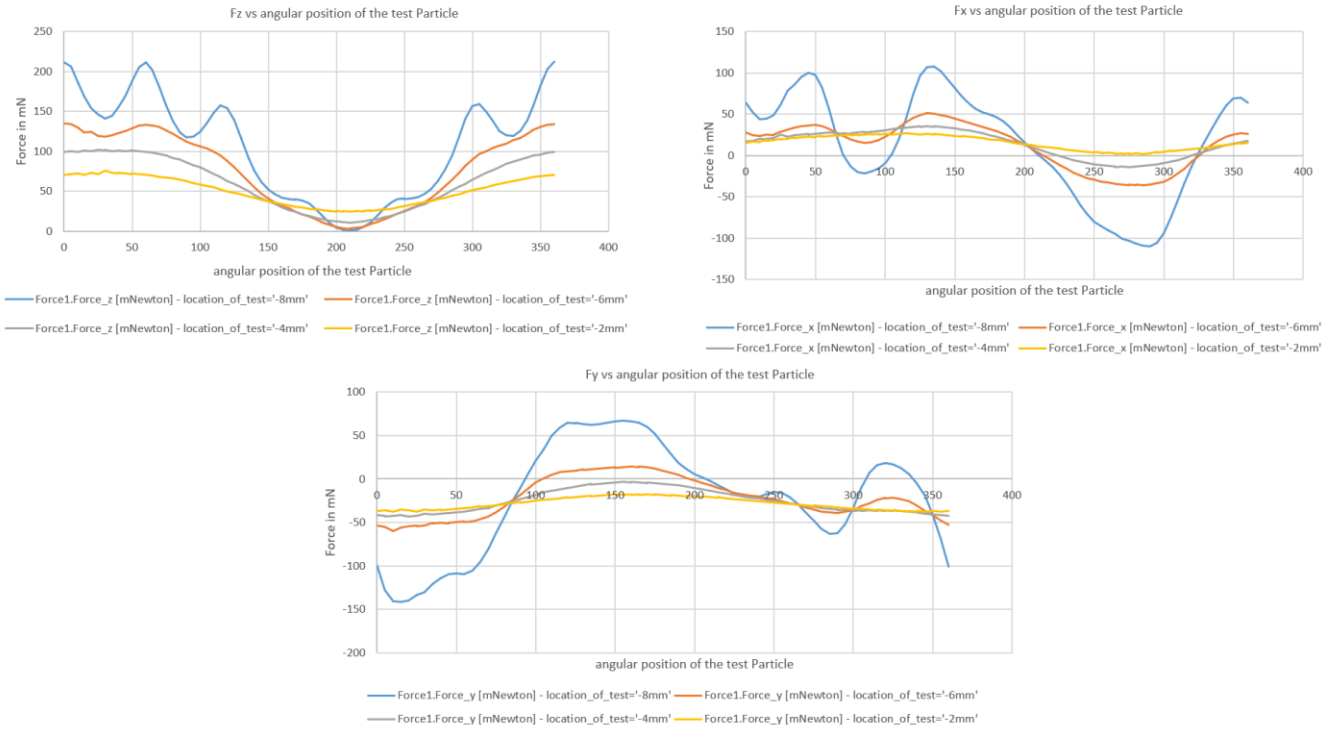

Figure 3.85 Force components on an iron particle on a circular track with variable radii also known as working gap due to 3 coils with alternate polarity setting

3.2.6.3 Four coil Setup

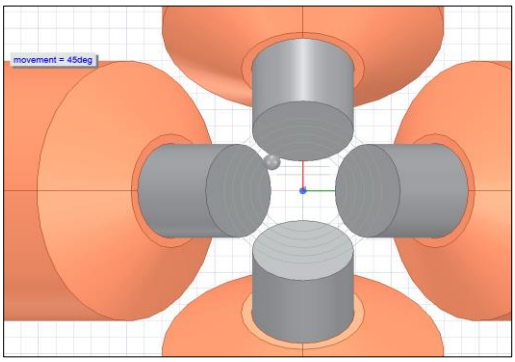

Figure 3.86 Iron particle on circular tracks on a 4-coil setup

A four-coil setup also produces similar results as a 3-coil setup. The test particle experiences a maximum force on the axis of the coil i.e. at 0^o, 90^o, 180^o, and 270^o. Moreover, there is an acceptable drop in total force in approximately +- 20^o sector (approximately uniform force fields). However, approximately 22% of the maximum force drops at locations where the particle is at the center of two adjacent coils. This drop is also a result of cancellation of forces due to equal attractive forces from 2 adjacent coils. Moreover, it can be observed that the normal forces almost remain constant throughout the entire track which is very suitable for precisely controlling the change in depth of indentation. Fig. 3.87 compares the force plots using adaptive meshing and inside selection length-based meshing (0.1 for test and 4mm for core and coil) – for efficient simulations.

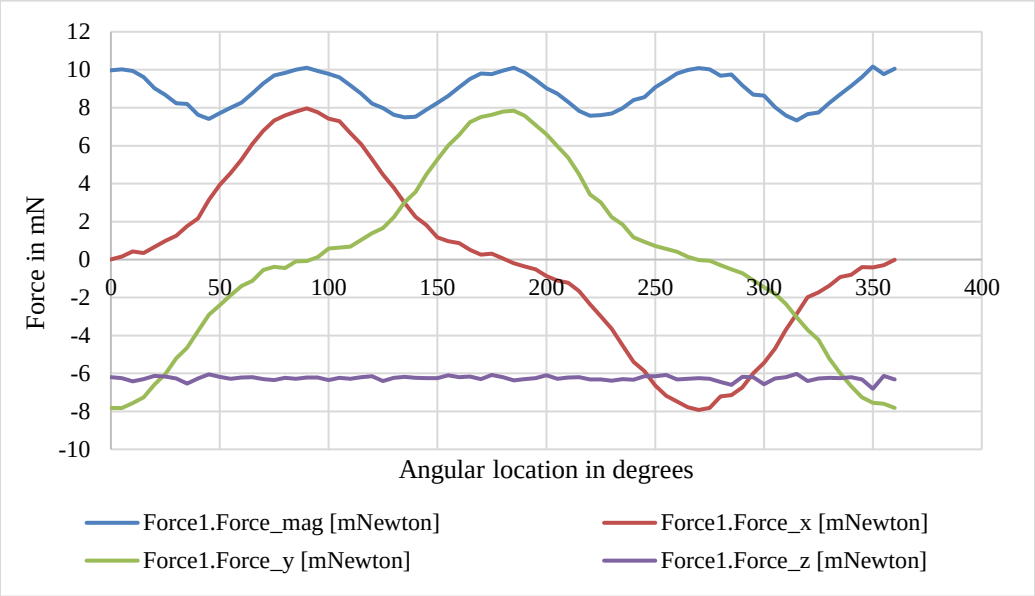

Figure 3.87 Force components on an iron particle on a circular track with variable radii also known as working gap due to 4 coils with same polarity

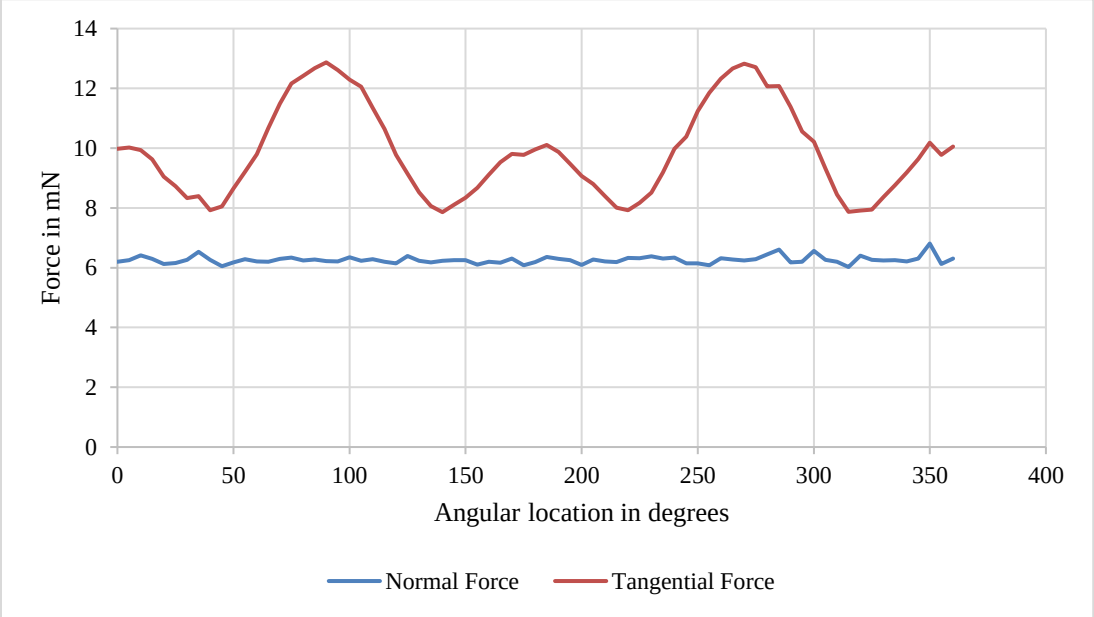

Figure 3.88 Tangential and Normal forces vs angular position of the test Particle (4 coils-same polarity)

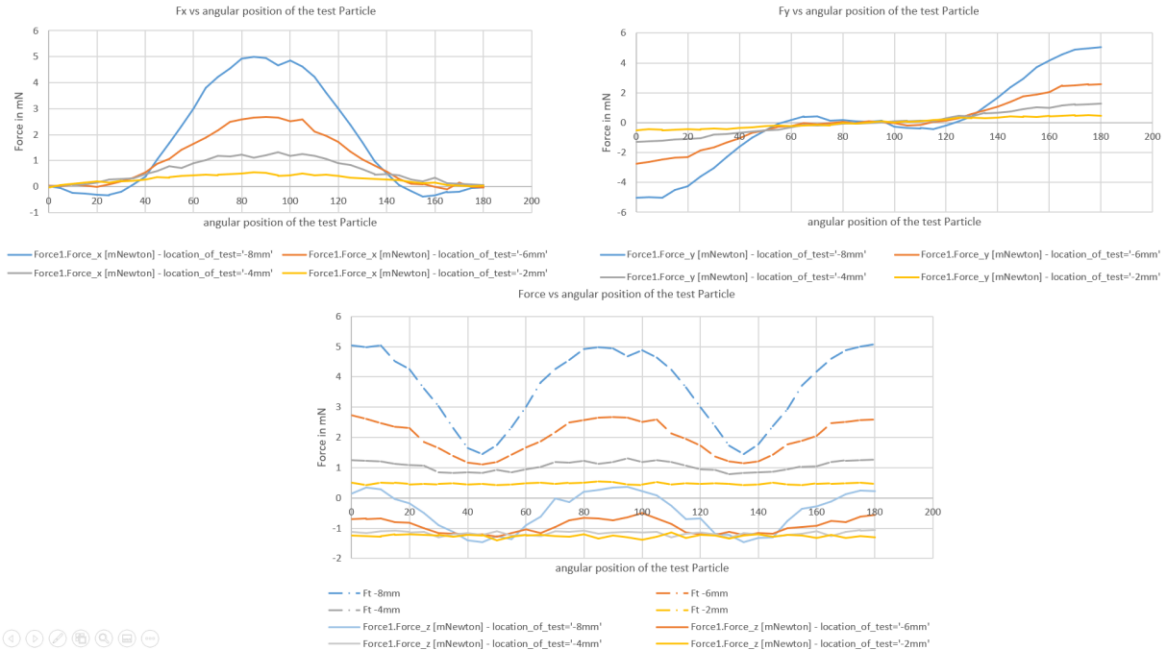

Figure 3.89 Force components on an iron particle on a circular track with variable radii also known as working gap[3] due to 4 coils with same polarity

[3] -8 mm represents a working gap of 1 mm and it increases in the order of 6mm, 4mm and 2 mm. These values are the radii of the circular track followed by the test particle to record the magnetic force. The same notation will be followed for all multi-coil cases.

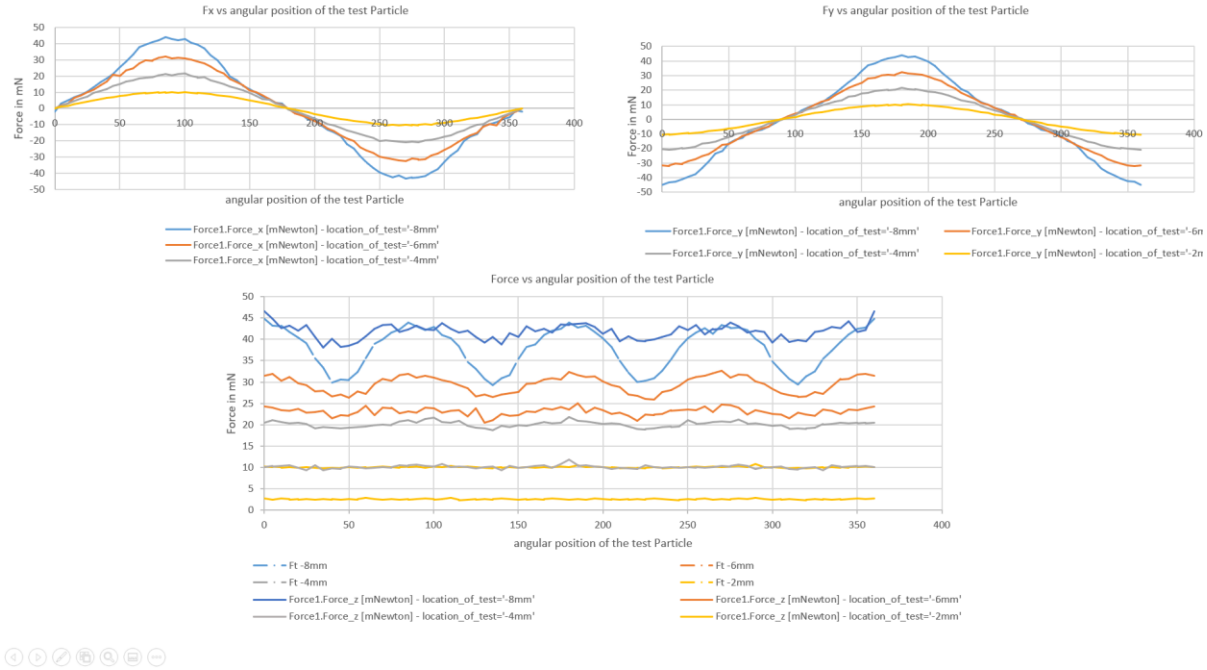

Figure 3.90 Force components on an iron particle on a circular track with variable radii also known as working gap[4] due to 4 coils with alternate polarity

3.2.6.4 Four Coil Taper Setup

The analysis of taper coils is conducted in two stages, first using an arbitrary taper value the coil polarities are tested for the alternate and the same polarity case and then the taper shape is optimized based on space efficiency and magnetic force. Fig. 3.91 and Fig. 3.92 illustrates the forces acting on an iron particle due to taper 4 coil arrangement with alternate polarity setting.

[4] -8 mm represents a working gap of 1 mm and it increases in the order of 6mm, 4mm and 2 mm. These values are the radii of the circular track followed by the test particle to record the magnetic force. The same notation will be followed for all multi-coil cases

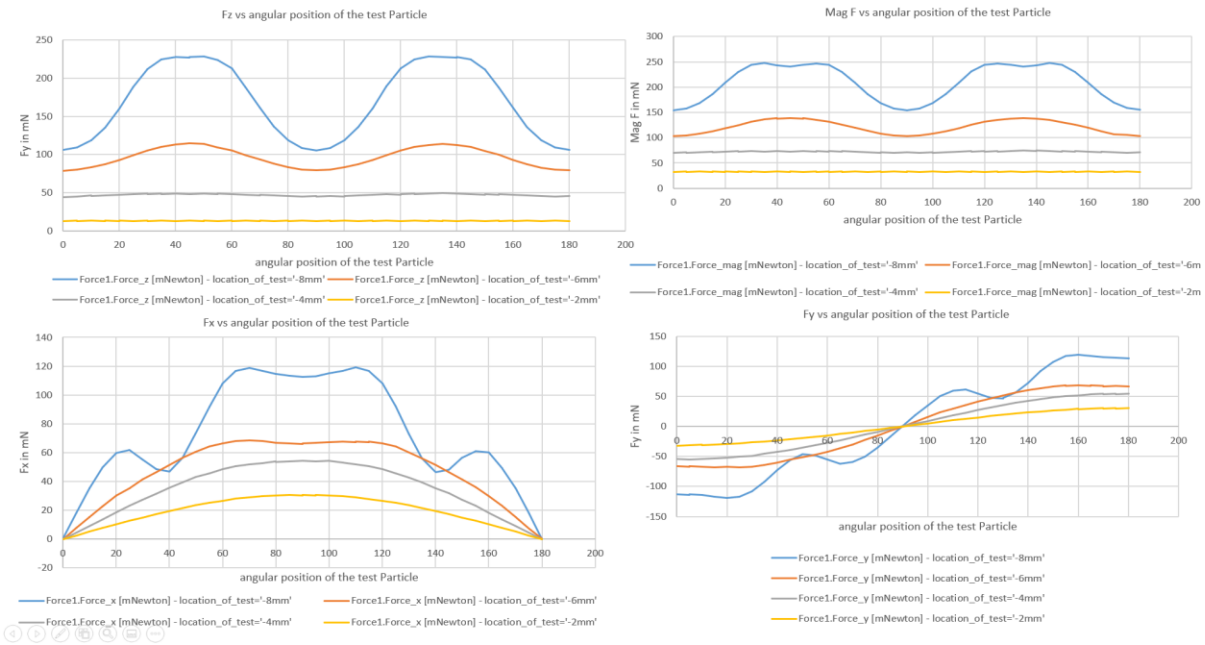

Figure 3.91 Forces acting on an iron particle due to taper 4 coil arrangement with alternate polarity setting – arbitrary Taper

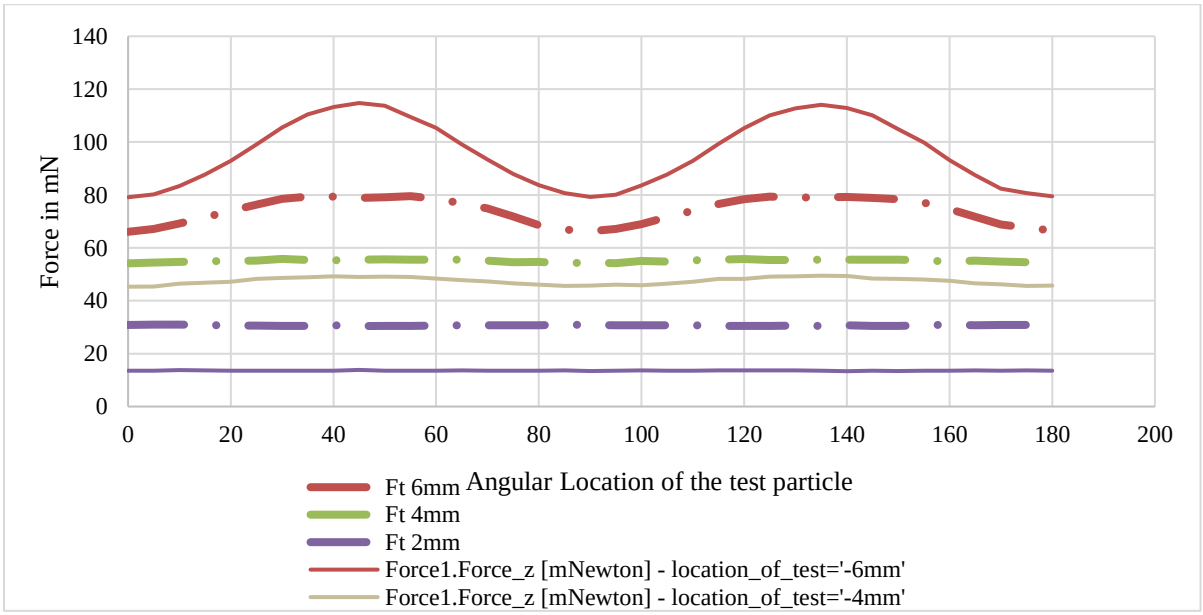

Figure 3.92 Comparison of Normal and Tangential forces for a 4-coil taper setup with alternate polarities

Now, to optimize the taper design different taper dimensions are tested and two of the iterations are discussed in this section, named as configuration 1 and optimized configuration. It must be noted that the optimization is done purely on the basis of space efficiency and magnetic field.

a) Configuration 1:

- Lower radius of the taper section = 12 mm
- Upper radius of the taper section = 15 mm
- Radius of the cylindrical section = 16 mm
- Height of the taper section = 14 mm
- Mirror distance achieved = 15 mm
- Reduction in mirror distance = 5 mm

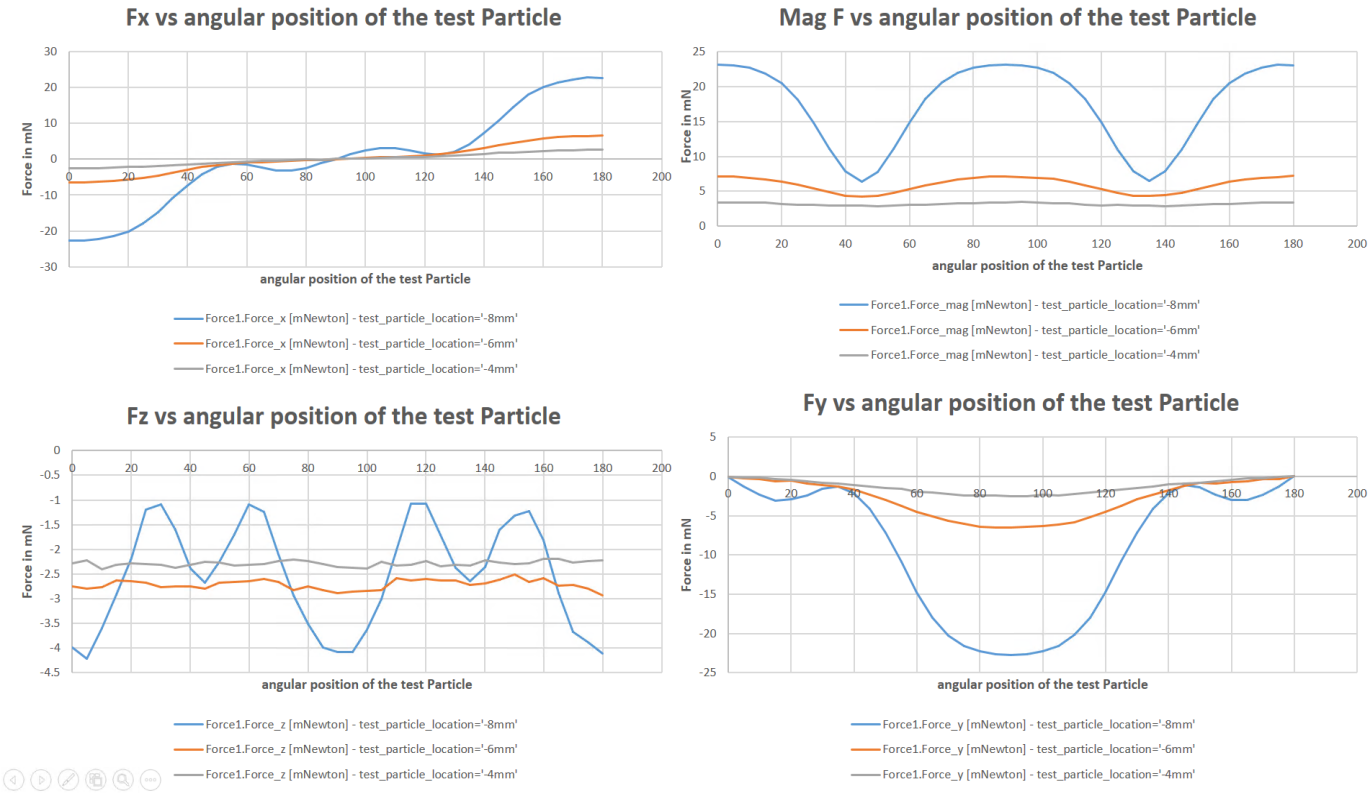

Figure 3.93 Forces acting on an iron particle due to taper 4 coil arrangement with similar polarity setting – Configuration 1

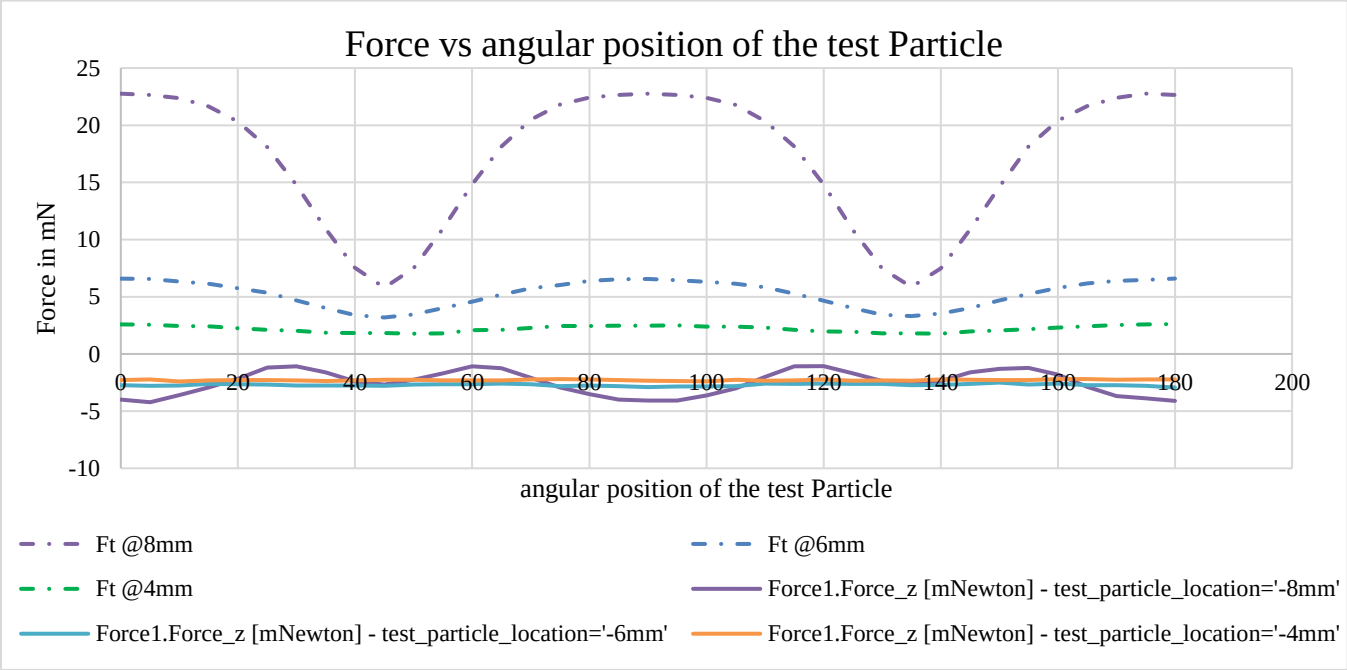

Figure 3.94 Comparison of Tangential and Normal forces acting on an iron particle due to taper 4 coil arrangement with similar polarity setting – Configuration 1

b) Optimized Configuration:

- Lower radius of the taper section = 10 mm
- Upper radius of the taper section = 16 mm
- Radius of the cylindrical section = 16 mm
- Height of the taper section = 10 mm
- Mirror distance achieved = 13 mm
- Reduction in mirror distance = 7 mm

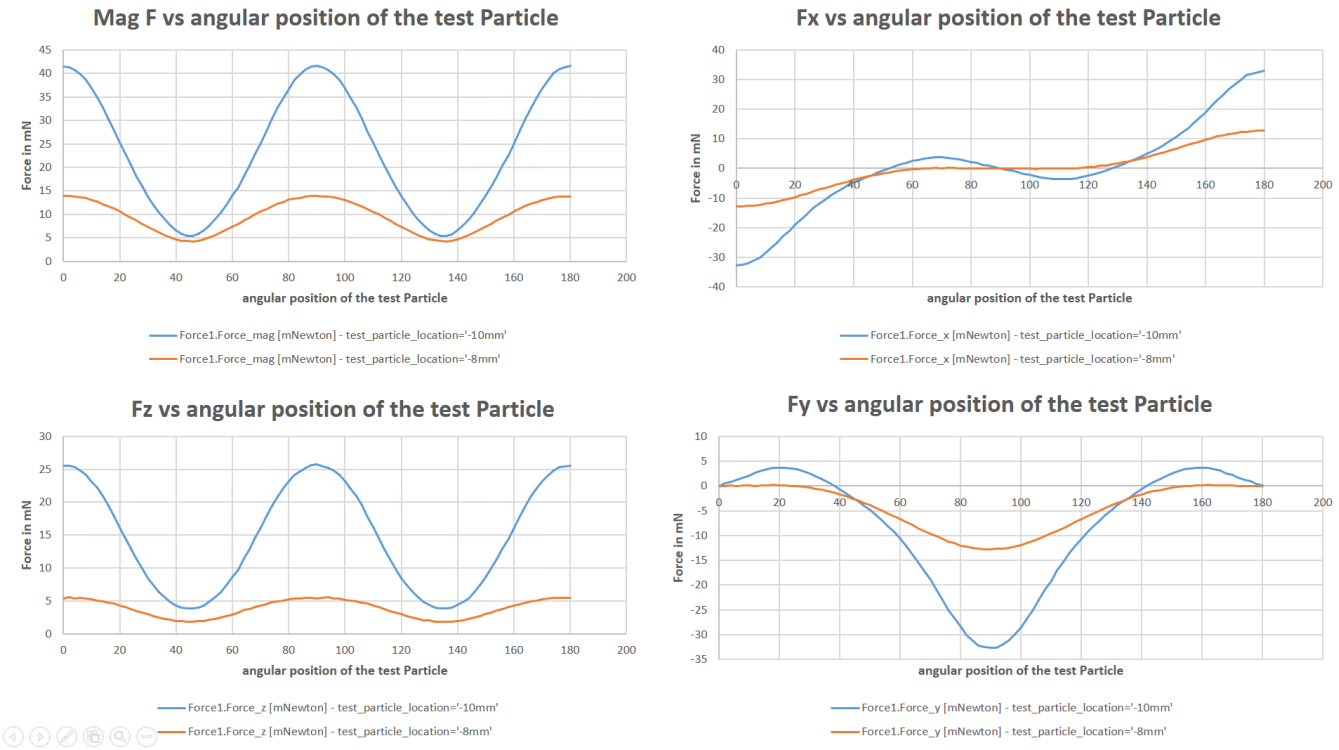

Figure 3.95 Forces acting on an iron particle due to taper 4 coil arrangement with similar polarity setting – optimized Configuration

Now, to study the effect of coil inclination on a multi coil setup, the angle of inclination of the 4 coils were changed to see its effect on the force output. It can be observed from Fig. 3.97 that inclinations in the range of $45^0 \pm 5^0$ give the highest values of force components and higher tangential than normal forces.

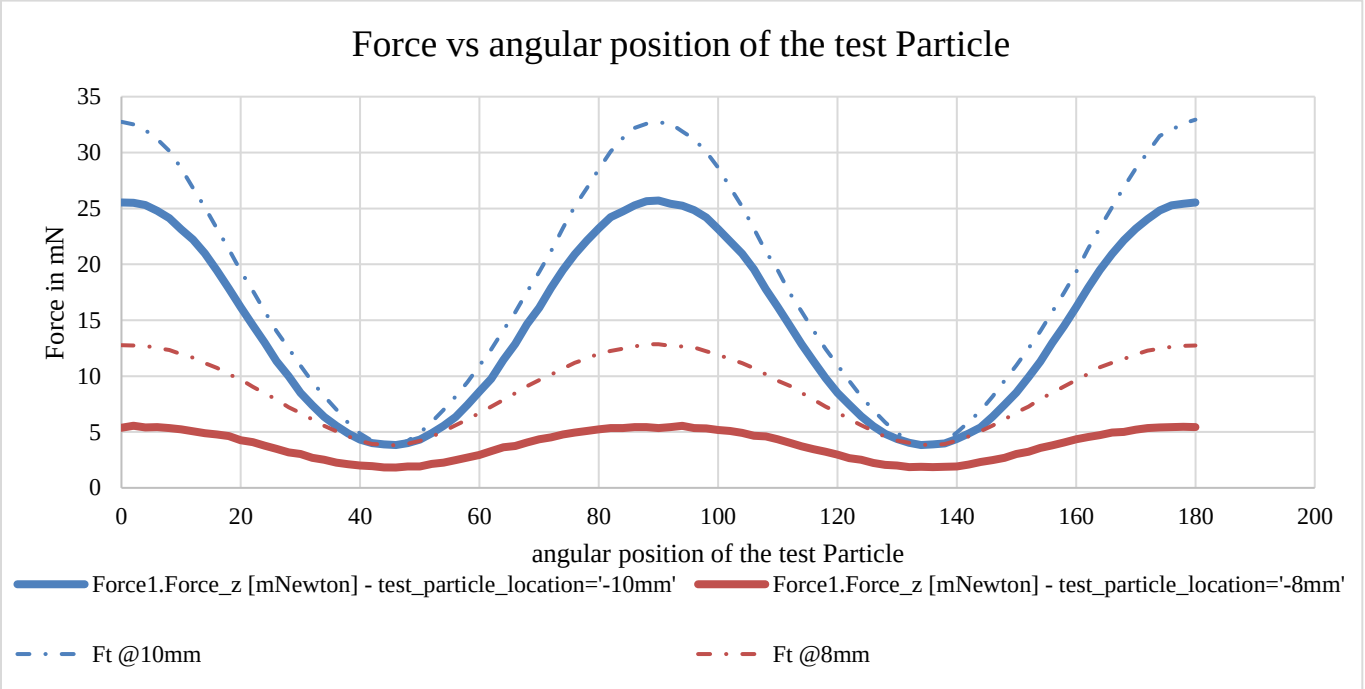

Figure 3.96 Comparison of Tangential and Normal forces acting on an iron particle due to taper 4 coil arrangement with similar polarity setting – Optimized Configuration 1

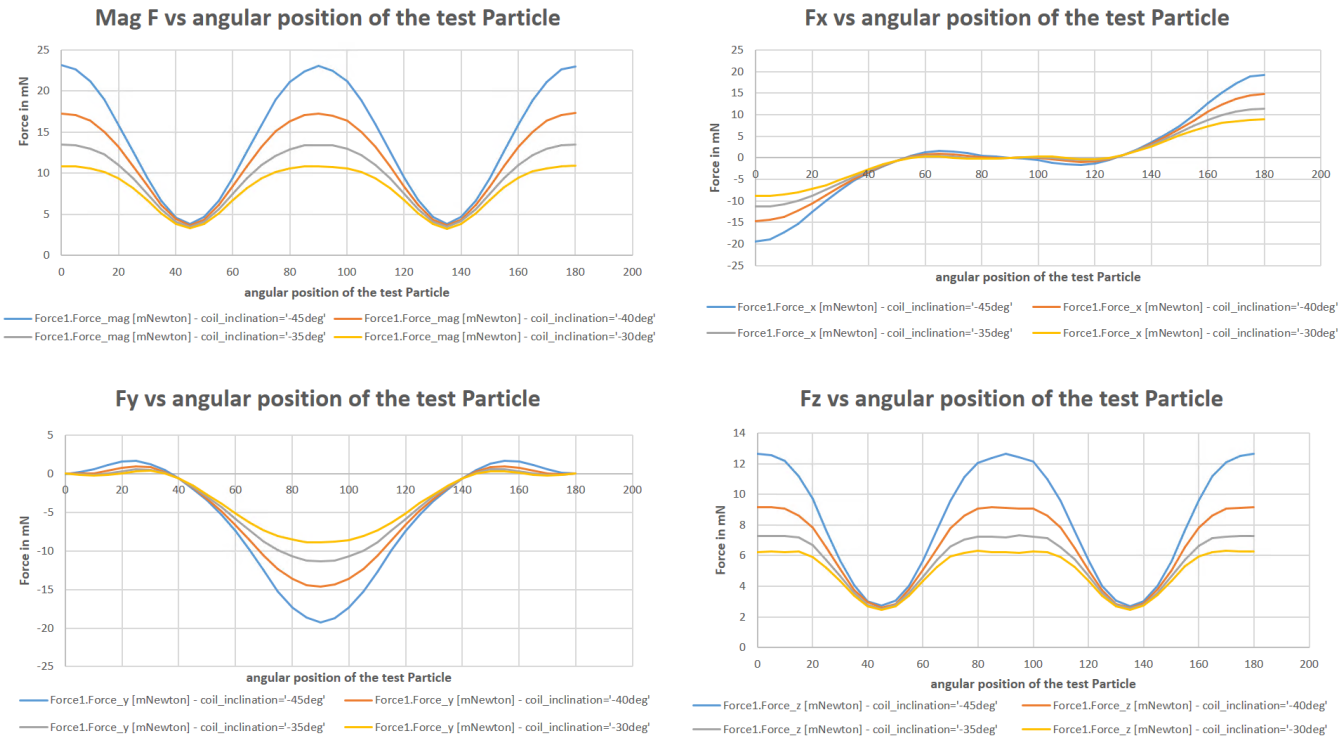

Figure 3.97 Forces acting on an iron particle due to taper 4 coil arrangement with similar polarity setting vs varying inclination angle with the vertical

3.2.6.5 Comparison of number of coils

It can be observed from figure 3.96 that addition of coils results in increase in the mirror distance (5mm for each coil addition). This increases the gap between two adjacent coils and the magnetic flux intensity reduces the force output on the iron particle. However, as discussed in the previous sections taper coils reduce the mirror distance and result in uniform magnetic field and high magnetic flux density. As seen in Fig. 3.98, 6 taper coils produce around 4 times more force than 6 cylindrical coils having the same current density.

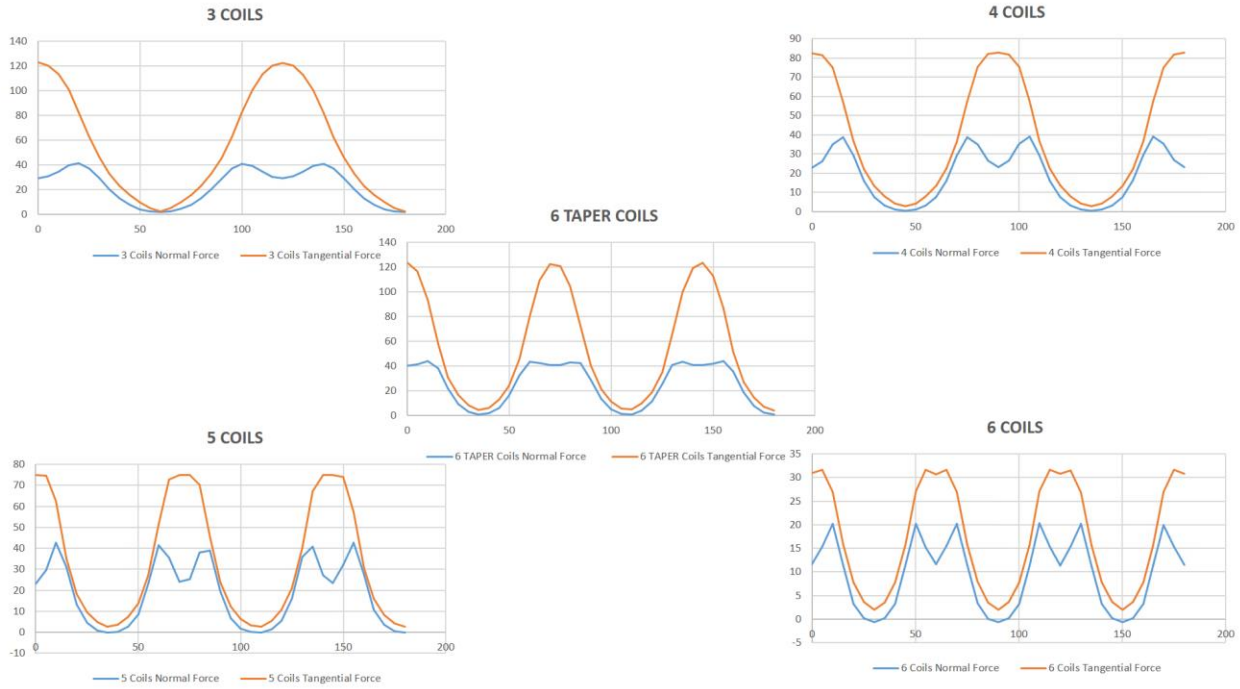

Figure 3.98 Comparison of Normal and Tangential forces for a multi coil setup with all the coils activated simultaneously with the same polarity[5]

3.3 Power required by a single coil

After optimizing the coil dimensions for required magnetic field, the power requirements for a single coil are calculated based on the current density and the maximum safe current capacity (5A). From FEA, it was found that a current density of 12 A/mm^2 is required to produce a magnetic field of about 0.3-0.5 T at the finishing spot (1-1.5 mm from the core tip). It can be observed from table 4 that AWG 22 produces a current density of 12 A/mm^2.

Specifications of AWG 22:

1. Wire diameter (bare copper) = 0.64 mm

[5] X-axis represent the location of the spherical test particle in degrees and the Y axis represents force in mN.

2. Cross sectional area = 0.33 mm^2
3. Diameter of wire with insulation = 0.71 mm
4. DC Resistance per 1000 m = 52 Ω

Power required by a single coil is based on the dimensions of a cylindrical coil, as the dimensions of a taper coil are subject to change based on the number of coils used in the setup. Following are the dimensions of a single cylindrical coil used for power calculations:

Length (l) = 41.4 mm; Inner radius (r_i) = 5.75 mm; Outer radius (r_o) = 16 mm.

Table 4 AWG wire optimization

Ampacity (A)	AWG	Diameter (mm)	Nr	Nz	N	Current density (1.5A)	1.5 A (AWG 21,22,23,24,25,26,27)	Current density (2A)	2 A (AWG 21,22,23,24,25,26)	Current density (3A)	3 A (AWG 21,22,23,24)	Current density (5A)	5A (AWG 21,22)
9	21	0.7239	14.15941	57.19022	809.78	2.862424931	1214.670019	3.816566574	1619.560026	5.724849862	2429.340039	9.541416436	4048.900065
7	22	0.64516	15.88753	64.17013	1019.505	3.603764415	1529.25743	4.80501922	2039.009906	7.20752883	3058.514859	12.01254805	5097.524765
4.7	23	0.57404	17.8559	72.12041	1287.775	4.552049201	1931.662079	6.069398935	2575.549438	9.104098402	3863.324157	NA	NA
3.5	24	0.51504	19.90137	80.38211	1599.714	5.654697021	2399.570681	7.539596028	3199.427575	11.30939404	4799.141362	NA	NA
2.7	25	0.45466	22.54432	91.05705	2052.819	7.256342343	3079.228873	9.675123124	4105.638497	NA	NA	NA	NA
2.2	26	0.40386	25.38008	102.5108	2601.732	9.196648273	3902.597695	12.2621977	5203.463593	NA	NA	NA	NA
1.7	27	0.36	28.47222	115	3274.306	11.57407407	4911.458333	NA	NA	NA	NA	NA	NA

Now, current density (J) required to produce a sufficient magnetic field at 1 mm axial distance from the core tip = 12 A/mm2

$$J = \frac{NI}{l(r_0 - r_i)}$$

$$12 = \frac{N * I}{41.4(16 - 5.75)}$$

Therefore, N*I = 5092.2

Assuming a maximum safe current of 5A, N = 1018. Due to inefficiency in packing, there is a reduction in the total number of turns during manufacturing and this is represented by a fit factor or packing factor (λ) which usually ranges between 0.8 to 0.9. We have considered a packing factor of 0.866 based on manufacturer recommendation.

N = 881 (after incorporating a fit factor of 0.866)

The total number of turns can also be calculated in the following two ways:

Method 1: The total number of turns is a product of the number of turns in the axial direction and the radial direction, which in turn is the total radial/axial coil length divided by the diameter of the copper wire.

Number of turns in the axial direction = Nz = $\frac{l}{d_w} = \frac{41.4}{0.71}$

Number of turns in the radial direction = Nr = $\frac{r_o - r_i}{d_w}$

Total number of turns = N = Nz * Nz = 841

Therefore, N = 728 (after considering packing factor of 0.86)

Method 2: The total number of turns can also be found by dividing the total cross-sectional area of the coil by the cross-sectional area of a single wire.

$$N = \frac{4l(r_o - r_i)}{\pi d_\omega^2}\lambda$$

$$N = \frac{4 * 41.4(16 - 5.75)}{\pi(0.71)^2}0.866$$

$$N = 763$$

$$\lambda = packing\ factor = 0.86$$

To find the resistance offered by the coil, total wire length is required. Length of copper wire per coil is found by multiplying the length of copper wire per layer with the total number of layers in the z-direction/axial direction.

Total length = length of wire per layer * number of layers

$$l = 2\pi\left\{\left(r_i + \frac{\mathrm{d}_\omega}{2}\right) + \left(r_i + \mathrm{d}_\omega + \frac{\mathrm{d}_\omega}{2}\right) + \left(r_i + 2\,\mathrm{d}_\omega + \frac{\mathrm{d}_\omega}{2}\right) + \cdots + \left(r_i + (n-1)\,\mathrm{d}_\omega + \frac{\mathrm{d}_\omega}{2}\right)\right\}$$

$$= 2\pi\left\{n_r\left(r_i + \tfrac{\mathrm{d}_\omega}{2}\right) + (0 + \mathrm{d}_\omega + 2\,\mathrm{d}_\omega \cdots + (n-1)\,\mathrm{d}_\omega)\right\}$$

Using sum of an arithmetic progression:

$$= 2\pi\left\{15\left(5.75 + \frac{0.71}{2}\right) + \frac{15}{2}(0 + (15-1)0.71)\right\} = 1.04\ m$$

Therefore, total length of wire = 1.04*58*0.86 =52 m

Resistance per 1000 m for AWG 22 = 52.8 Ω

Total resistance of wire per coil (R) = 2.7 ohm

Voltage (V) = I * R = 13.5 V

Using a factor of safety of 1.5, V= 20.25 Volts

Power required per coil (P) = V*I Watts = 101.25 W/coil

Alternatively, the length of wire = $l = 2\pi N\left(r_i + \frac{r_0 - r_i}{2}\right)$

$$= 2\pi * 763\left(5.75 + \frac{16 - 5.75}{2}\right)$$

$$= 52\ m$$

3.4 Conclusion

It can be concluded that taper coils provide a better space efficiency as compared to their cylindrical counterparts in terms of creating a uniform force field (without high peaks and dips) in the working gap. However, from a scalability point of view, taper coils pose a challenge as the taper length and taper radius ratio is optimized for a given number of coils. Therefore, we first proceed with a conservative four and six coil taper setup with optimized inclinations and tip geometries. Moreover, the magnetic field strength produced by a taper coil is close to the results obtained from a cylindrical coil. Hence, the advantages of reducing mirror distance by about 5 mm in every case far outweighs the reduction in magnetic field due to loss in number of current carrying conductors. The coil, core tip geometry, inclination angle and the power requirements are all optimized to produce a magnetic field of about 0.3-0.5 T at 1-1.5 mm distance from the core tip.

Chapter 4

Experimental Setup and System Description

4.1 Introduction

To implement the polishing technique a physical system was designed and fabricated while prioritizing portability and flexibility of the process. The primary function of the setup is to generate rotating magnetic fields to manipulate the motion of the Magnetic Abrasive Particles (MAPs) on the surface of the test specimen without using any rotational or translational machinery during the process. The entire system is developed on a multi-level portable platform capable of sustaining shocks, vibrations and shopfloor environments. The system is a combination of electromechanical and mechatronics sub-systems comprising of an FPGA simulator/controller, raspberry pi based secondary control units, power supply, motor drives and auxiliary systems as explained in the following sections.

In a typical MAF process the cutting/chipping action is a resultant of two forces generated due to the gradient of the magnetic field: the normal component and the tangential component. The normal component is responsible for the indentation of the MAPs in the workpiece and is generated due to the force acting on the magnetic particles between opposite magnetic poles. The tangential component of the force is responsible for the final chipping action as it overcomes the yield shear stress of the material. Conventionally, permanent/electromagnets are mounted on rotating machinery such as mills and lathe to create the tangential component and, hence generating a rotating magnetic field. This makes the setup very bulky and almost impossible to be portable.

The current system mainly includes a plurality of magnetic abrasive particles, a stationary electromagnet array configured and arranged to create a rotating magnetic field, a control unit, motor drives, a host PC and a DC power supply. The system may further include frame arms that can be manipulated along multiple axis to change position, orientation, and relative location of individual electromagnets in reference to the workpiece.

The design and optimization of the electromagnet geometry is discussed and validated in chapter 3. The electromagnet includes a ferromagnetic core, and a copper coil wound around the magnetic core. The copper coil is wound in a tapered manner at one end of the core to reduce the distance between adjacent coils and maintain a uniform distribution of magnetic field in the workspace. The coil design is optimized using both analytical and finite element analysis to maximize the gradient of magnetic field on both the axial and off-axial locations. The magnetic field gradient can be significantly magnified by selecting an appropriate core tip shape and core material as the core tip is used to direct and concentrate the magnetic flux lines in the working spot. Moreover, an extended core tip can also result in reduced leakage of magnetic flux. Iron was selected for the core and core tip as it has one of the highest relative permeability (4000) amongst metals.

4.2 System Level Description

Fig. 4.1 is a system level representation of the novel magnetic abrasive polishing apparatus. The system itself has multiple circuit breakers to avoid over current and over voltage situations in conjunction with CSA certified subsystems. The physical setup comprises of 5 sub-systems/levels including an additional/optional control module. The entire system is placed on a multi-level AV cart capable of sustaining shocks, vibrations and harsh environments. The following sections explain the function and capabilities of each sub-system.

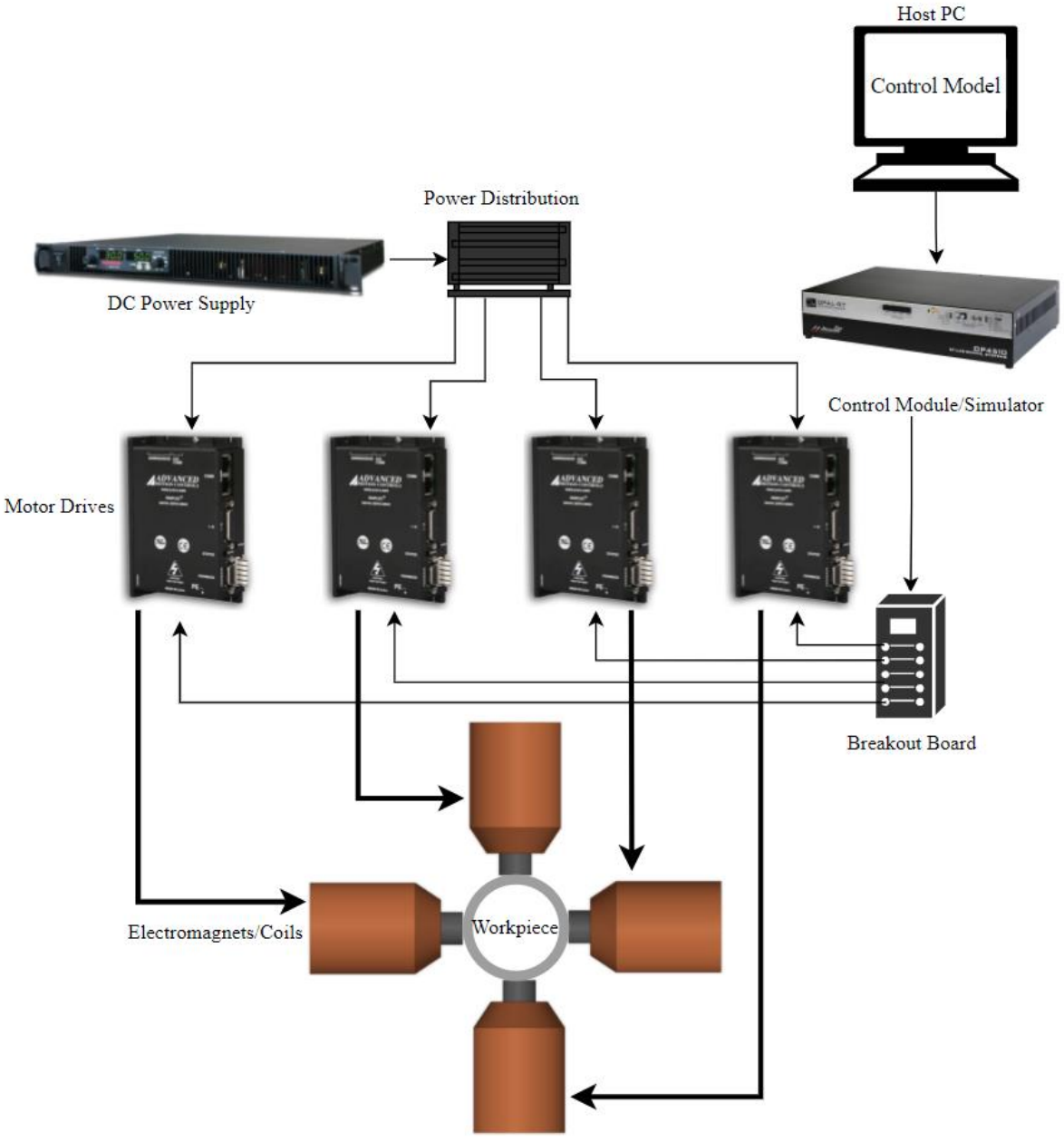

Figure 4.1 Magnetic Field Assisted Abrasive Polishing – System level Diagram

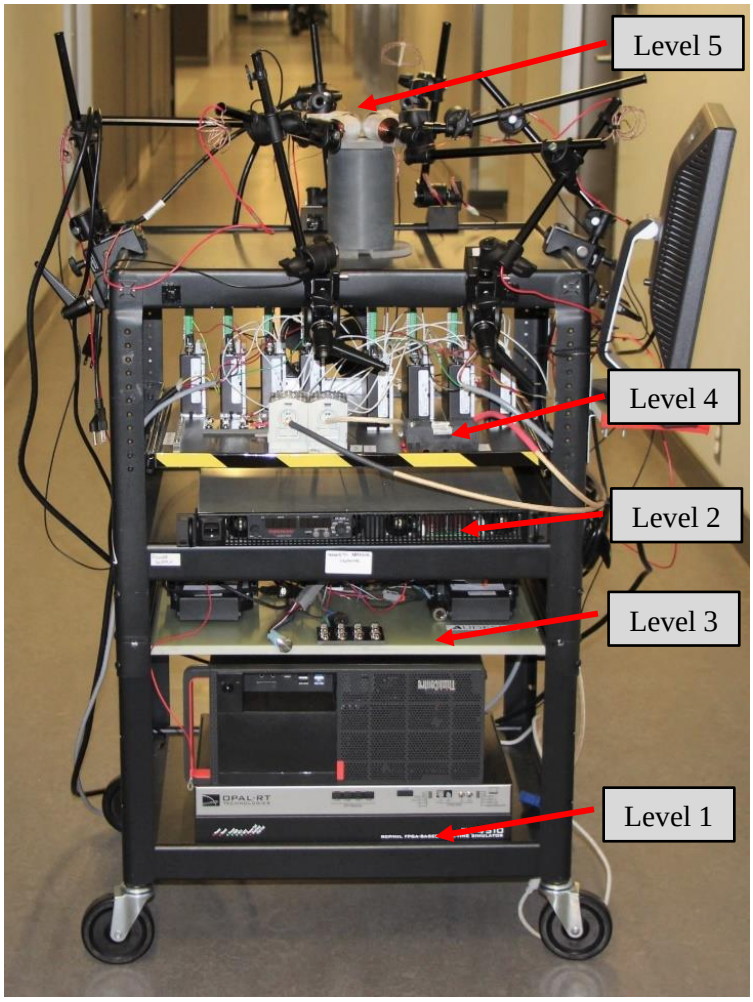

Figure 4.2 Magnetic Field Assisted Abrasive Surface Polishing – Apparatus

4.3 Subsystems

4.3.1 Level 1 – Simulator and Host Computer

Level 1 contains a computer and an FPGA based simulator. The primary function of this stage is to control (via analog/digital signals) the output current waveform produced by the digital servo drives. The host PC is used as an interface between the operator and the apparatus. Different process parameters (frequency, amplitude, and phase difference) can be monitored and changed real time on a GUI

developed on MATLAB Simulink via a display mounted on the apparatus. The simulator is a 3.5 GHz processor with Kintex7 FPGA. It has 32 digital and 16 analog inputs and outputs which can send analog and digital signals to the drives, based on the Simulink signal block connected to each pin. The control model (sub-section 4.4) for the apparatus is an open loop model built in MATLAB Simulink. Once built the control model is loaded and executed onto the simulator which can then operate in stand-alone mode.

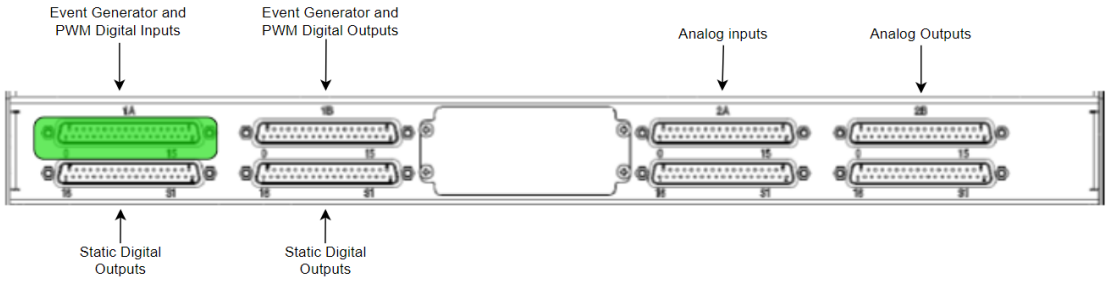

Figure 4.3 I/O ports on primary simulator

4.3.2 Level 2 – Power Supply

The primary function of Level 2 is to provide power to the drives to energize the coils. This is achieved by a programmable 1500 W DC power supply capable of producing 0-50A and 0-30V with a peak-to-peak output ripple of 50 mV. The output from the power supply is sent to the power distribution stage on level 4 via a slow blow 25A fuse (fuse current ratings vary with the number of coils in use). The power supply always maintains a minimum voltage of 20V due to the minimum supply voltage requirements of the digital servo drives. Power is sent to the distribution stage via AWG 8 fiberglass insulated wire and then distributed to the drives and the coils via AWG 22 wires.

4.3.3 Level 3 – Secondary/Auxiliary Control Units and Equipment Cooling

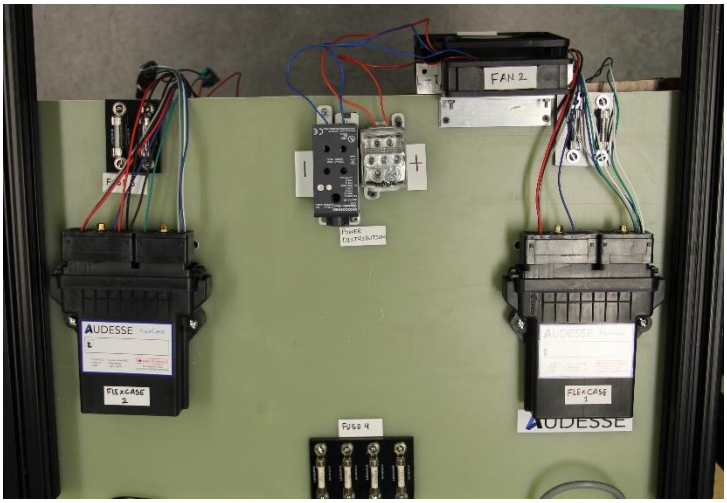

Figure 4.4 Level 3 - Secondary Auxiliary Control Unit

Level 3 is an auxiliary control unit based on two robust (IP67 Resistant) Raspberry Pi controllers and automotive grade microprocessor units. Each standalone unit can be used to power up to 4 coils. Each unit has 28 hardened I/O ports with 10 digital/PWM output (3A) ports. The level can be used in the future to replace the primary simulator, drives and power supply by a single unit. However, this control module can only output digital signals (PWM) as compared to both analog and digital signal capability of the primary simulator. This level is also integrated with two DC equipment cooling fans for both level 3 and level 1.

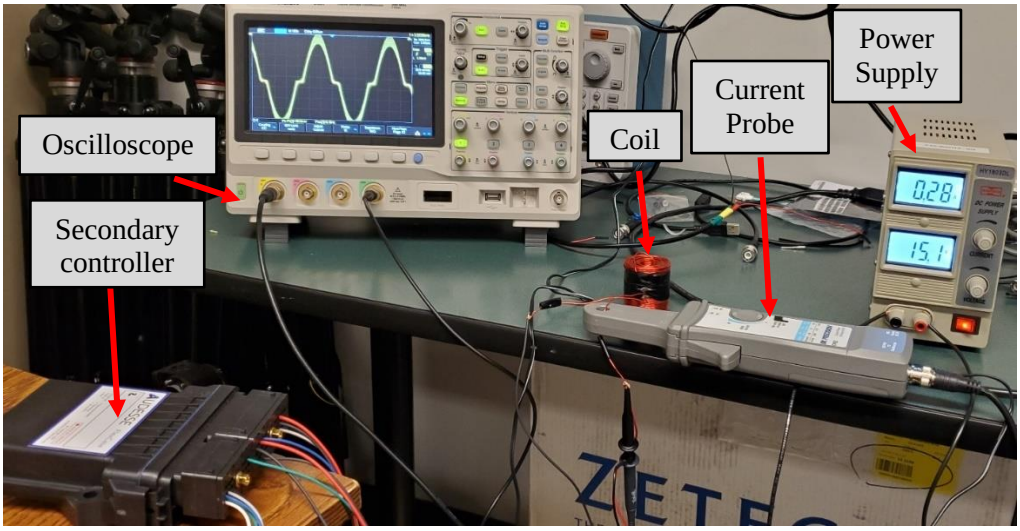

Figure 4.5 Output current waveform generated by a single port on the stand-alone control unit

4.3.4 Level 4 - Power Distribution and Amplifier/Motor Drives

Level 4 of the apparatus distributes DC power from the power supply to up to 8 digital servo drives via single pole power distribution blocks. The sliding shelf design of this stage makes it easy to reconfigure the drives via a USB-RS232 serial port. In order to produce an alternating current from a DC power supply, digital servo motor drives are integrated in the system. The digital servo drives are programmed to generate current waveforms based on the analog/PWM command voltage signals from the simulator/secondary controller. These drives act as invertors to convert DC to AC. In current control mode of servo drives/amplifiers, the input command voltage signal (+/-10V) controls the output current. The drive adjusts the output duty cycle and frequency to maintain the commanded output current. The output current, voltage and analog signal parameters are monitored in DriveWare through a built-in digital oscilloscope. The drives are set to a maximum peak current of 5A (for 5s) and a continuous current of 4.5A. The coils are configured as brushed DC motors in the tuning software (DriveWare). To calibrate the output current with respect to the input analog signals the drives are tuned to current loop coefficients of kp = 15.027 and ki = 0.1 over a range of frequencies less than 150 rad/s. Both the

current and voltage waveforms energizing the coils were measured via a current probe on a digital oscilloscope to confirm accurate reproduction of waveforms generated by the Simulink model. This level also contains the cooling fans for the drives and circuit breakers/slow blow fuses between power supply and power distribution (25A), power distribution and drives (8A); and drives and coils (7.5A). The fuse ratings are changed with change in the total number of coils.

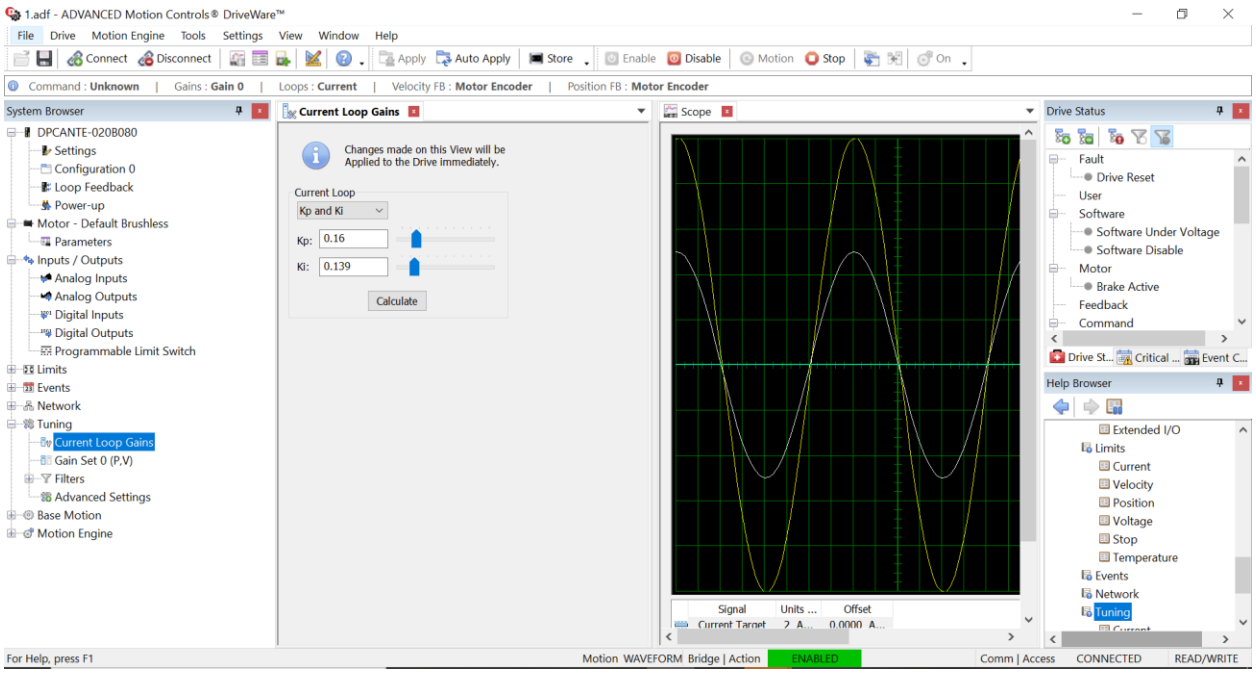

Figure 4.6 Current Loop Tuning of Servo Drives

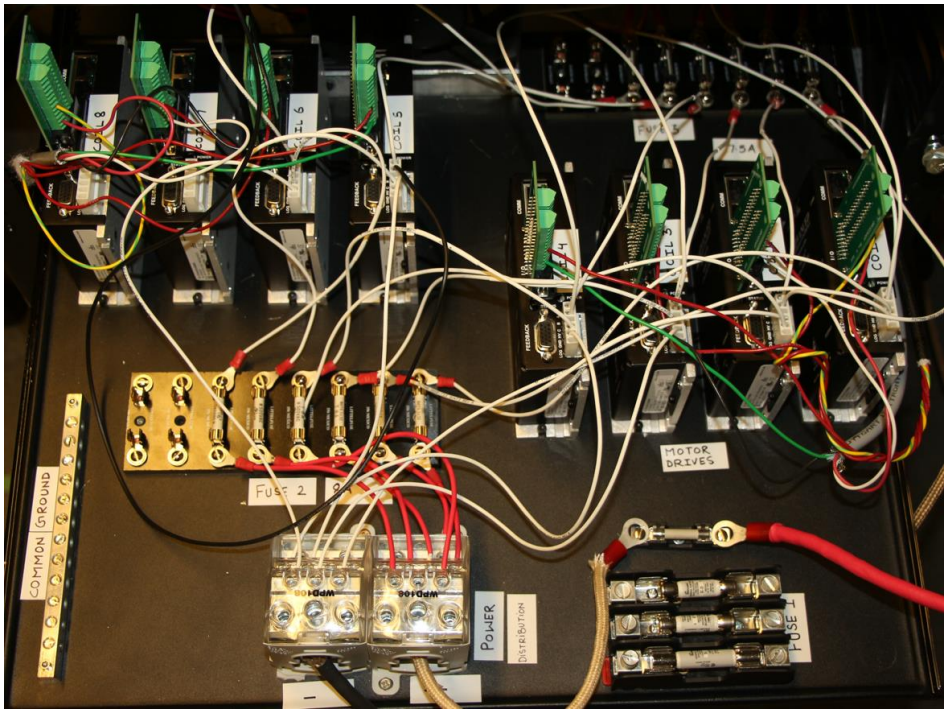

Figure 4.7 Level 4 - Power distribution and drives/amplifiers

4.3.5 Level 5 – Electromagnet Array and Test Jig

4.3.5.1 Electromagnets

An optimized tapered electromagnet shape is designed for maximizing both normal and tangential components of the magnetic field. The process of optimizing the dimensions, shape and orientation of the coils is discussed in detail in chapter 3. The electromagnets used in this research have a pure iron (99.1%) (also known as low carbon magnetic iron) core to amplify the magnetic flux density in the working region. The cores were further heat treated/annealed in a wet hydrogen environment to reduce magnetic aging and stabilize the magnetic behavior.

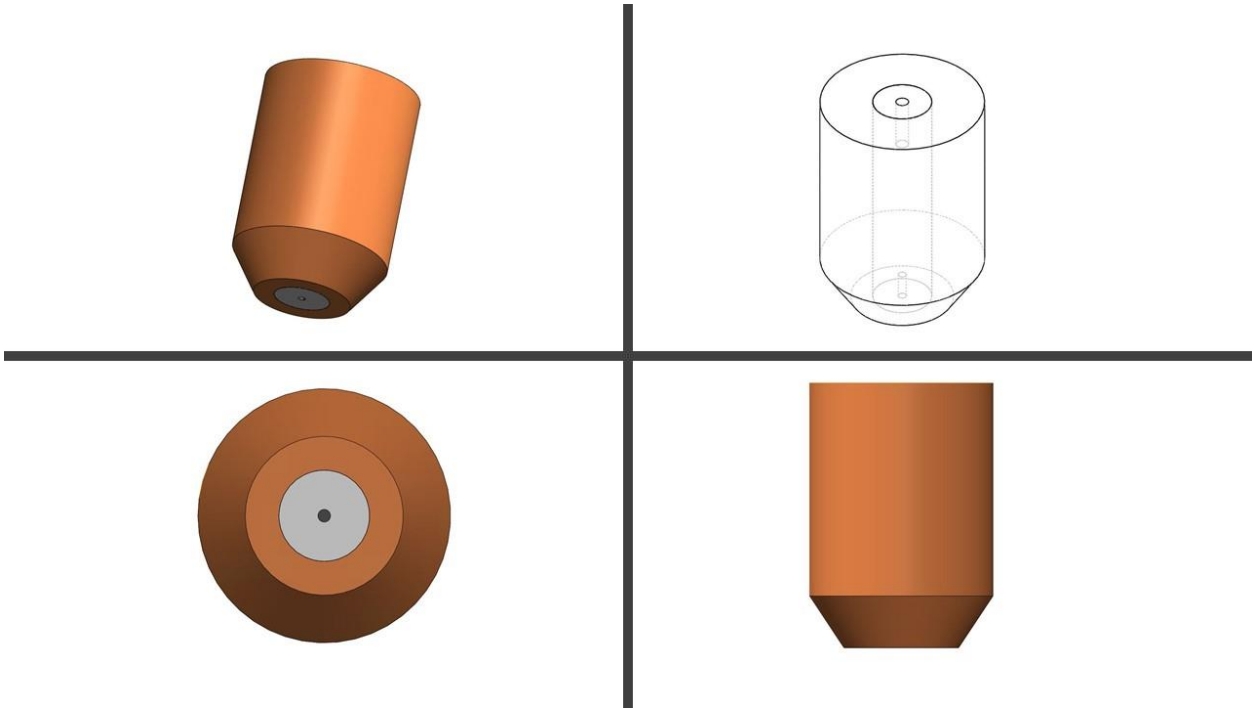

Figure 4.8 Optimized taper coil

The tapered end of the coil allows the user to populate a greater number of coils in the test rig as compared to purely cylindrical coils and hence generating a more uniform magnetic field. In order to avoid coil slip at the taper end during and after the winding process, a thin layer of (0.127mm) polyester film insulation (Fig. 4.9) was added between each axial layer for structural integrity. Furthermore, each coil is manufactured with a k-type thermocouple attached to the inner winding to measure the real time temperature of the coils.

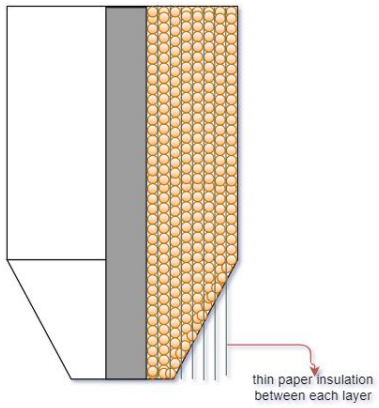

Figure 4.9 Cross-Section view of the Tapered Electromagnet

The tapered end of the coil is also equipped with a modular tip arrangement. Eleven different shapes (Fig. 4.11) of core tips were machined from pure iron to direct the magnetic flux lines based on the shape and size of the test specimen.

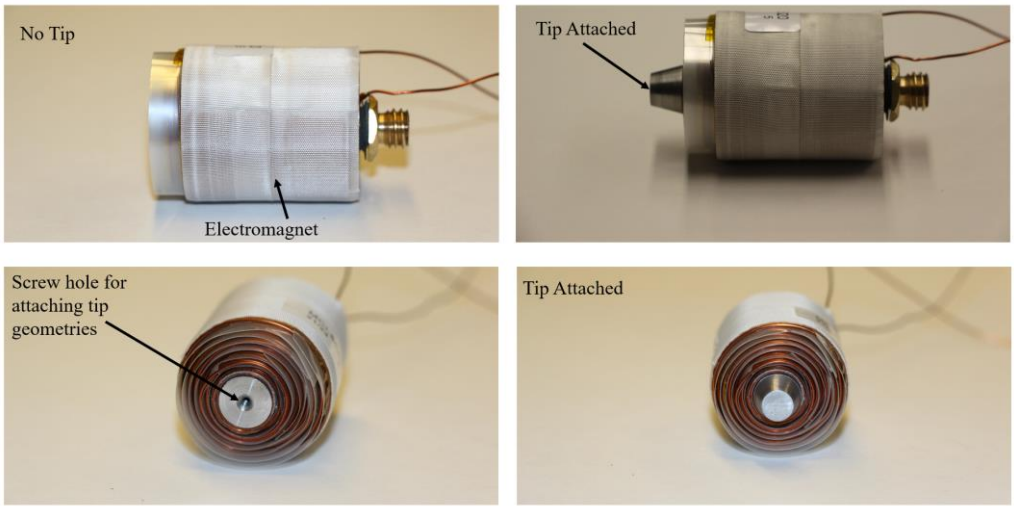

Figure 4.10 Optimized Novel Taper Electromagnet with and without core tip

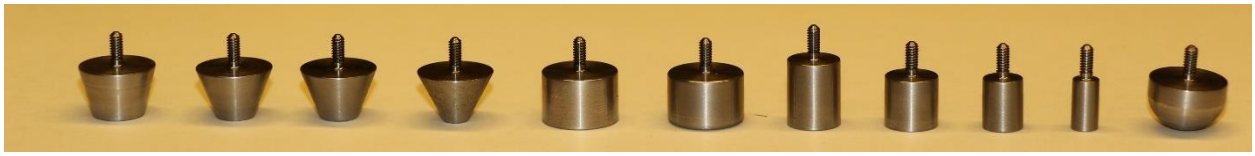

Figure 4.11 Pure iron core tip shapes

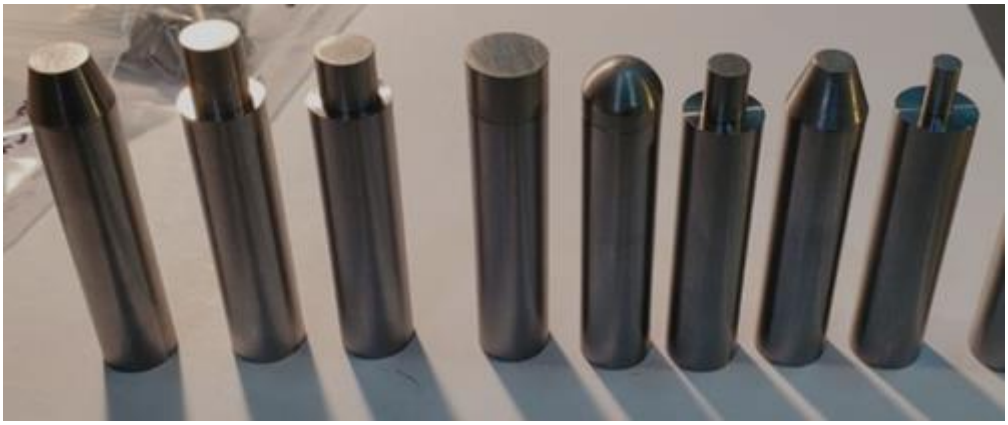

Figure 4.12 Machined core tips attached to pure iron machined cores – before winding

4.3.5.2 Test Jig

The angular inclination and position of each coil relative to other coils and the workpiece are critical parameters to generate a rotating magnetic field. To position the coils at any location and orientation, each coil is mounted/screwed via custom machined brass adapters on triple articulated double sectioned aluminum arms which can be aligned at multiple angles and orientations with a maximum reach of 23.8″. Different test rigs were designed to setup cylindrical and flat sheet specimens for accurate positioning of both the coils and the specimens and to isolate vibrations due to adjacent coils.

For cylindrical specimens, two different water jet acrylic cut outs were designed to hold the coils at 90^0 and 60^0 angular separations for 4 and 6 coils respectively. A 3D and actual representation of coil arrangement for a cylindrical test specimen is shown in Fig. 4.14 and Fig. 4.15. The coils are secured on slots to avoid vibrations at high frequency and to facilitate accurate horizontal positioning.

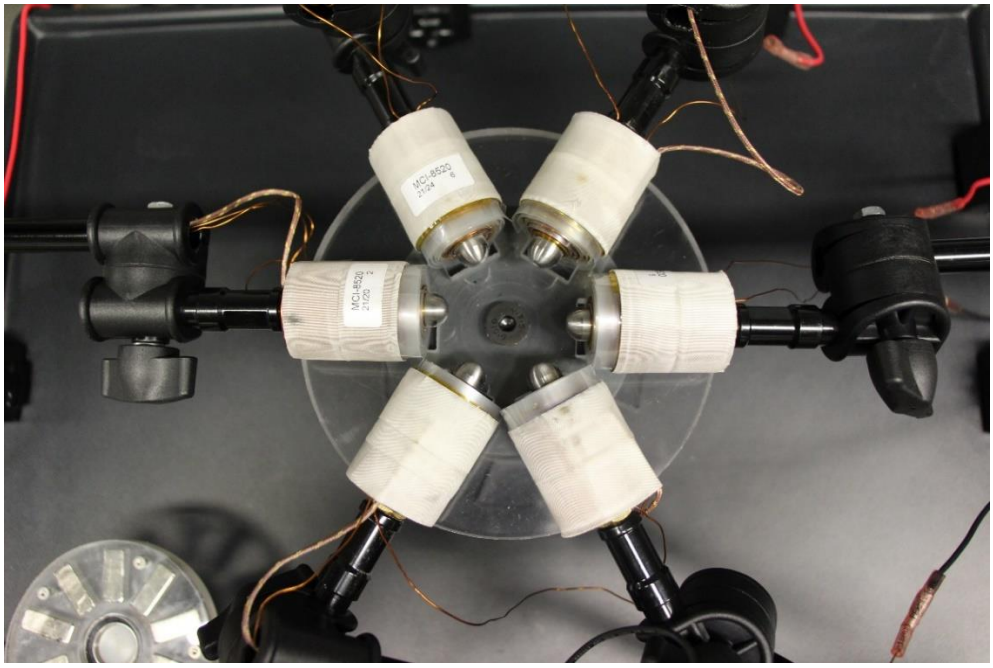

Figure 4.13 Electromagnets arranged for a cylindrical test specimen – top view

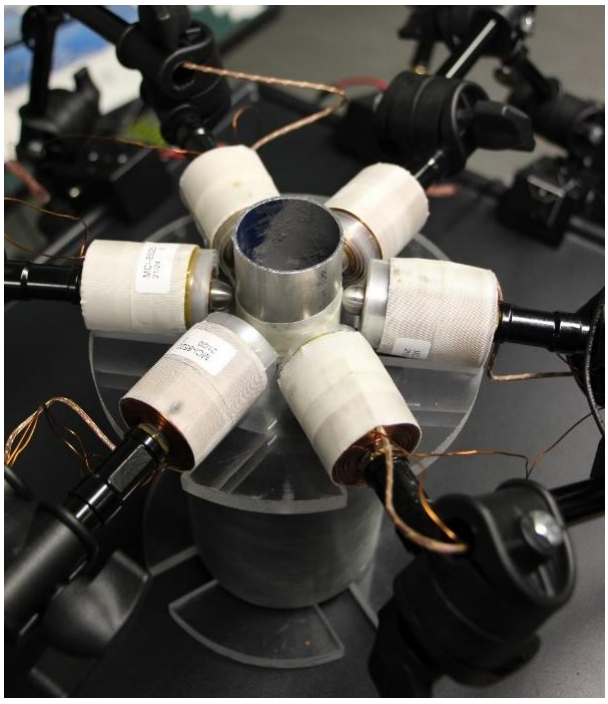

Figure 4.14 Electromagnets arranged for a cylindrical test specimen – side view

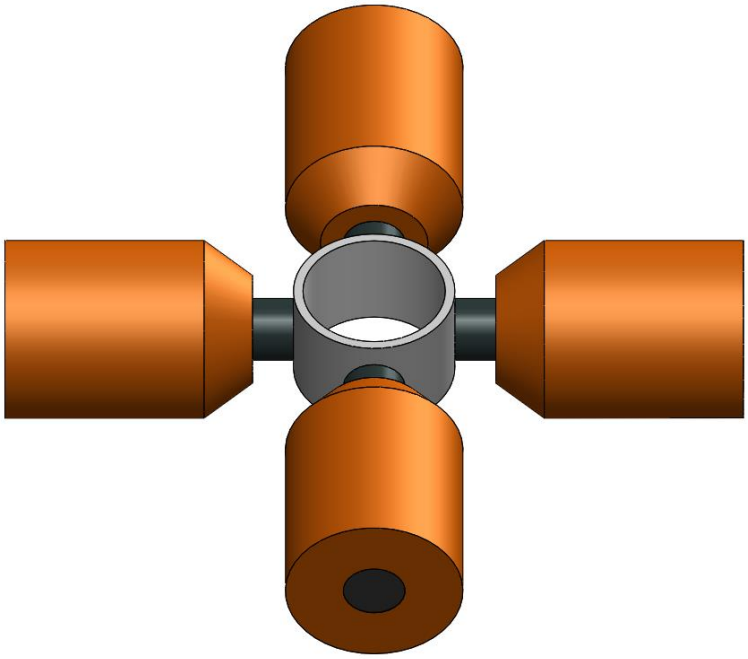

Figure 4.15 3D visualization of electromagnets arranged for a cylindrical test specimen

For flat sheet specimens, a jig was designed to position 4 or 6 coils (depending on the application) at any angular and linear position. Fig. 4.16 illustrates the arrangement of coils for a flat sheet specimen.

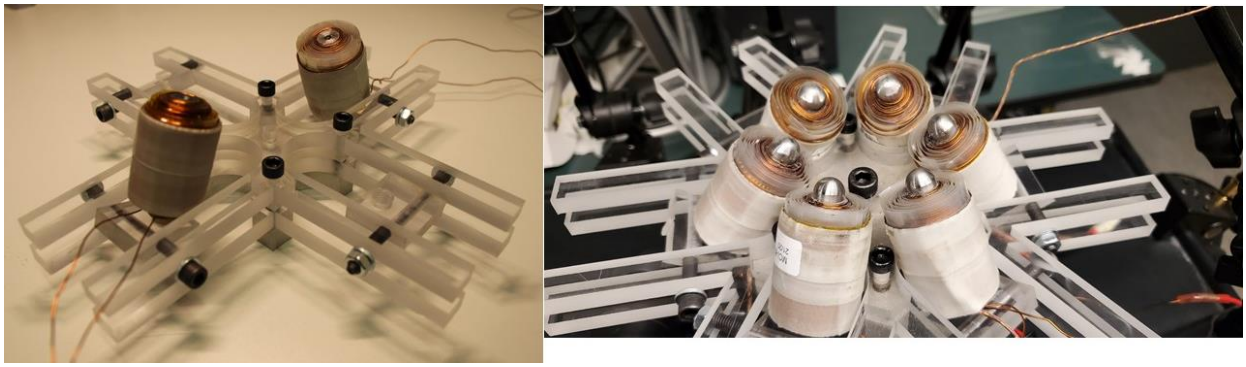

(a) (b)

Figure 4.16 Arrangement of four (a) and six (b) coils for flat sheet specimens

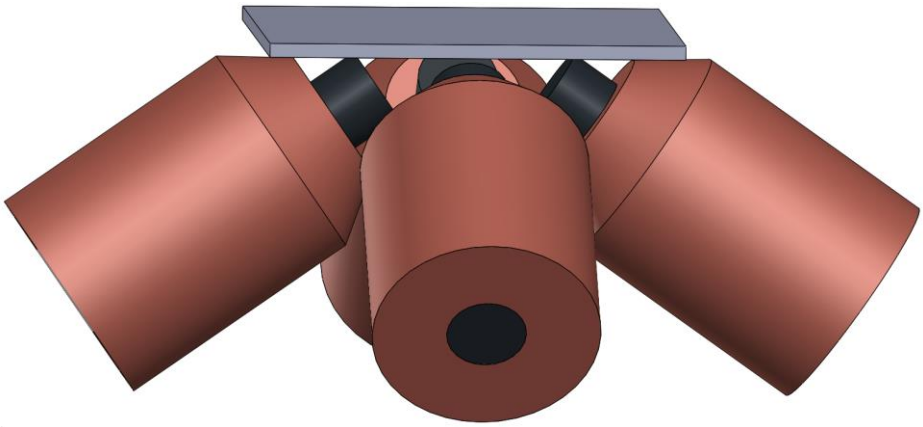

Figure 4.17 3D visualization of electromagnets arranged for a flat sheet test specimen

For flat sheet experimental trials, the test jig also comprises of an aluminum frame for holding the test specimen and DC fans for heat dissipation of coils. The aluminum frame is a table with center punched acrylic top. The cut out in the center of the acrylic sheet is used to place the specimen. Another epoxy sealed acrylic box is placed on the specimen to provide safety against the carcinogenic nature of the abrasive particles (CAS # 1344-28-1; CAS# 409-21-2).

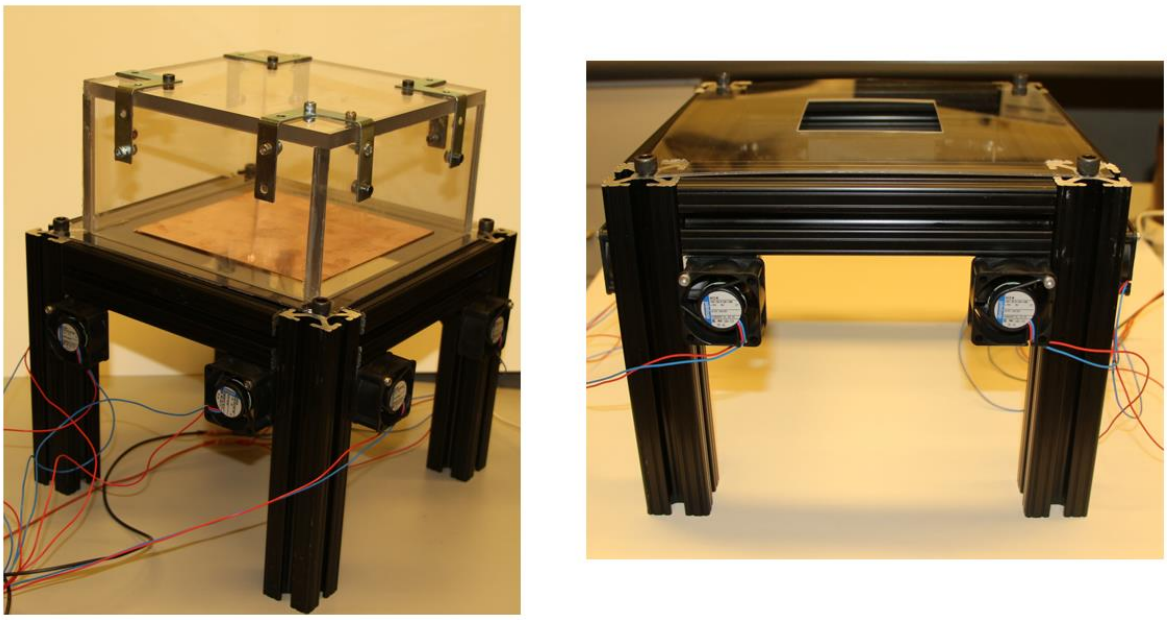

Figure 4.18 Test Platform for flat sheet specimens with cooling fans and protection cover

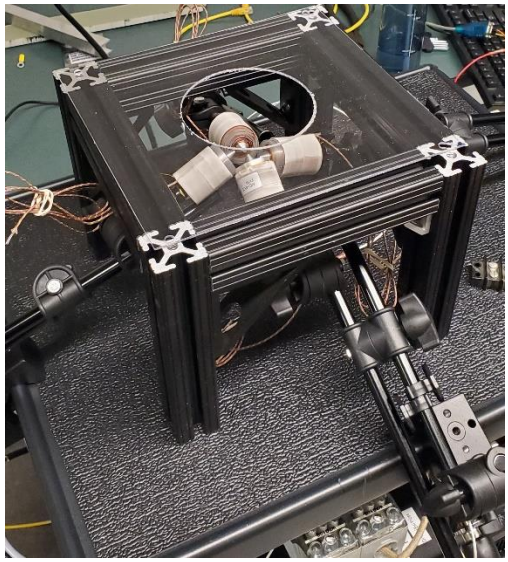

Figure 4.19 Coils directed towards the flat sheet test platform.

For cylindrical specimens, protection against abrasive powder is provided by placing a plastic cap on the open side of the specimen. The modular nature of the system allows the operator to change the core tip shapes, angle and location of the coils at any instant.

4.4 Control Model

A control model is required to produce and alter the characteristics of a Rotating Magnetic Field, which forms the principle of operation of the novel polishing system. Rotating Magnetic Fields (RMF) are the foundation of operation of electric motors. The current system exploits this principle by implementing RMF to manipulate the motion of the MAPs on the surface of a workpiece. RMF cannot be generated by stationary permanent magnets or a single-phase electromagnet. To generate an RMF by stationary electromagnets, poly-phase alternating currents are used to energize more than 1 pair of windings [29]. The angular velocity of the RMF is determined by the frequency of the alternating current. A minimum of two windings/coils are required to produce an RMF, however, for the purpose of polishing, a minimum of four coils are required to produce the desired motion of the MAPs, as explained in chapter

3. All coils are energized by a sine wave. The following equations represents the current waveforms energizing a 4 coils setup [30]:

$$I_1 = I_M \sin\omega t$$

$$I_2 = I_M \sin(\omega t + 90)$$

$$I_3 = I_M \sin(\omega t + 180)$$

$$I_4 = I_M \sin(\omega t + 270)$$

Where I_n represents the current through $coil_n$ and ω is the frequency of the sine wave. Each adjacent coil has a phase difference of 360/n, where n is the number of even coils. The control model is an open loop system in Simulink that generates analog sine waves for individual coils. The frequency and the amplitude of the sine wave is identical for all coils. Once built, the Simulink model can be loaded and executed on the simulator, which then sends analog voltage signals emulating the sine waves generated by the Simulink model. The SC console block in Simulink is responsible for providing inputs/outputs to the main control logic and SM Master contains the model.

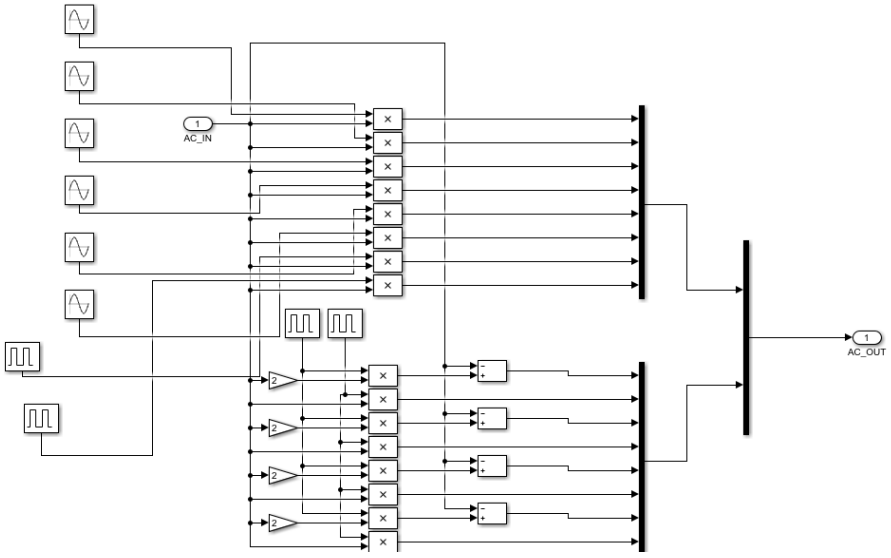

Figure 4.20 Simulink control model

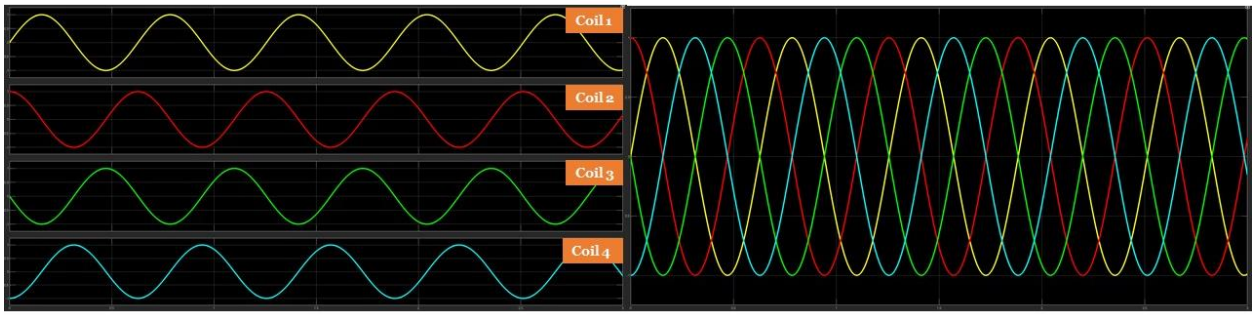

(a) (b)

Figure 4.21 (a) individual and (b) overlapped current waveforms to generate a rotating magnetic field with 4 coils

For implementing the secondary/auxiliary control unit, Pulse Width Modulation (PWM) is implemented in Simulink as the controller can only output Digital PWM signals and not analog signals. PWM is a square wave signal that repeats itself at a certain frequency and varying duty cycle [31]. A duty cycle of 50% for a 100V signal means in each cycle the signal is off for half of the time and on for the other half. Hence, the effective voltage is the average of the PWM signal i.e., 50 V. Therefore, by varying the duty cycle from 0 to 100 % different amplitudes of the signal/output voltage can be produced. Fig. 4.22 illustrates the manipulation of duty cycle to create an average sine wave. The switching frequency of the duty cycle is tuned to track the refence signal.

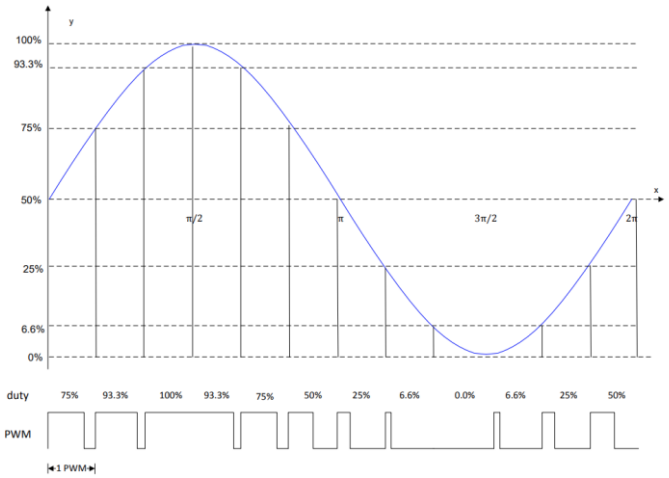

Figure 4.22 Pulse Width Modulation [32]

The control model is built in Simulink and the .elf file is flashed to the target using S32DS for standalone utilization of this module. However, it must be noted that for the experimental implementations only the analog control model was used in the primary simulator.

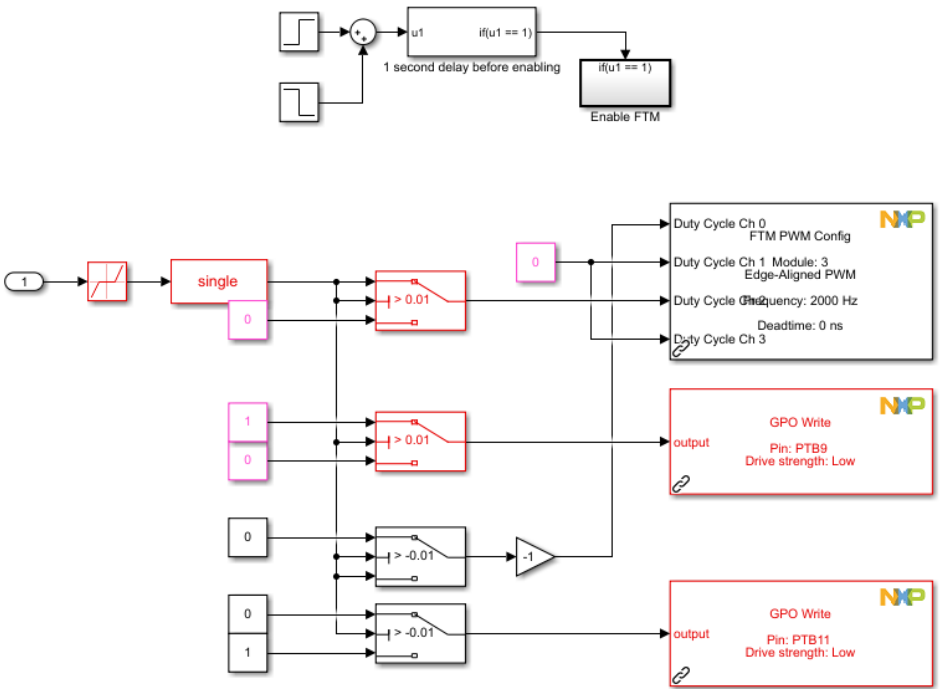

Figure 4.23 Simulink model for secondary control unit

Chapter 5
Experimental Results

This chapter introduces the experimental trials performed to validate the performance and effectiveness of the optimized coil geometry, coil array orientation and implementation of the polishing technique on different specimen types. This chapter is divided into two sections, the first section includes the design validation and characteristics of the novel tapered electromagnet, and the second section illustrates the implementation and characterization of the polishing technique on cylindrical and flat sheet specimens.

5.1 Evaluation of Electromagnet Characteristics and Performance

Due to the non-linear nature of magnetic field most researchers usually incline towards finite element analysis to evaluate and optimize electromagnet geometries [33]. However, it is very crucial to validate the analysis of any FEA software (Ansys Maxwell) with experimental results.

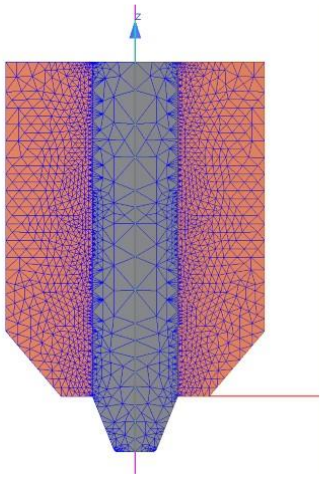

Figure 5.1 Finite Element Model of the Novel Tapered Electromagnet

The magnetic field was calculated using 2D (cylindrical coordinates) and 3D FEA models in Ansys Maxwell. The electromagnets are optimized for magnetic field on both axial and off axial locations. To validate the results obtained from the finite element modelling, the magnetic field of a single electromagnet was experimentally measured. To achieve this, a Lakeshore Cryotronics 421 Gauss meter with both normal and tangential probes was used. The gauss meter can measure magnetic fields ranging from 300 mG to 300 kG with a resolution of 0.01 kG for both DC and AC (rms) magnetic fields. Fig. 5.2 illustrates the experimental setup used to measure the magnetic field values on the tip and axis of the optimized taper electromagnet. Furthermore, to accurately position the gauss probe, a micromanipulator arm was utilized.

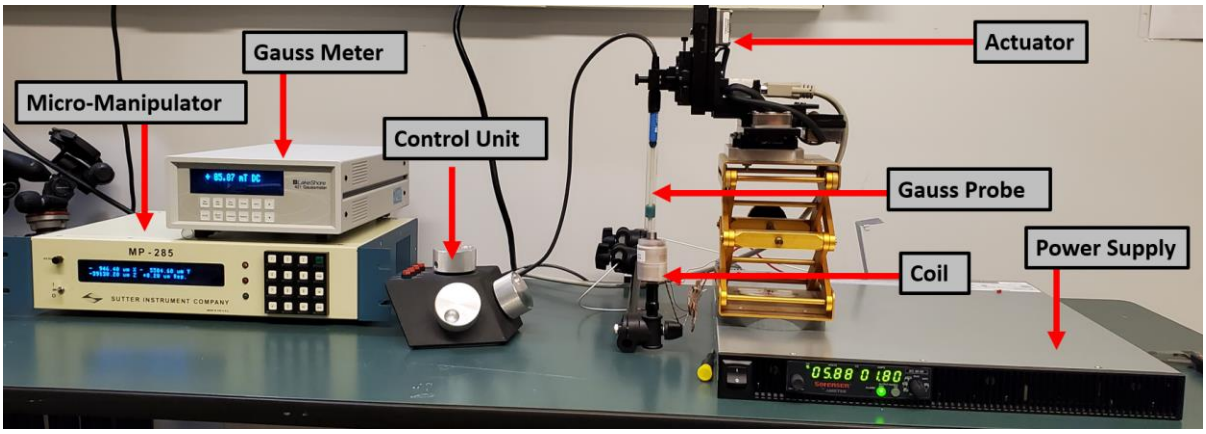

Figure 5.2 Experimental Measurement of Magnetic Field

It can be observed from Fig. 5.3 that the finite element results from Ansys Maxwell match with an average error of under 8% with the experimental values. Hence, it can be confirmed that the finite element models can be used to measure the magnetic field at any point in the 3D space.

The field measurements were also performed on different core tip shapes to understand the flux concentration capabilities of each shape. Fig. 5.4 and Fig. 5.5 summarizes the net magnetic field in z direction produced by different core tip shapes at different current/voltage levels. It was observed that

geometries with small and sharp edges produce the highest ON-axis magnetic fields, however, the magnetic field drops significantly at off axis locations due to the presence of sharp edges. A spherical core tip shape, however, performed in the most optimal way by maintaining uniform magnetic field at all points on the tip. Off axis field measurements of two core tip shapes were studied to understand the drop in magnetic field in the radial direction. Fig. 5.6 and Fig. 5.7 illustrate the off-axis field values for conical 3 and small cylindrical 3mm core tip shapes.

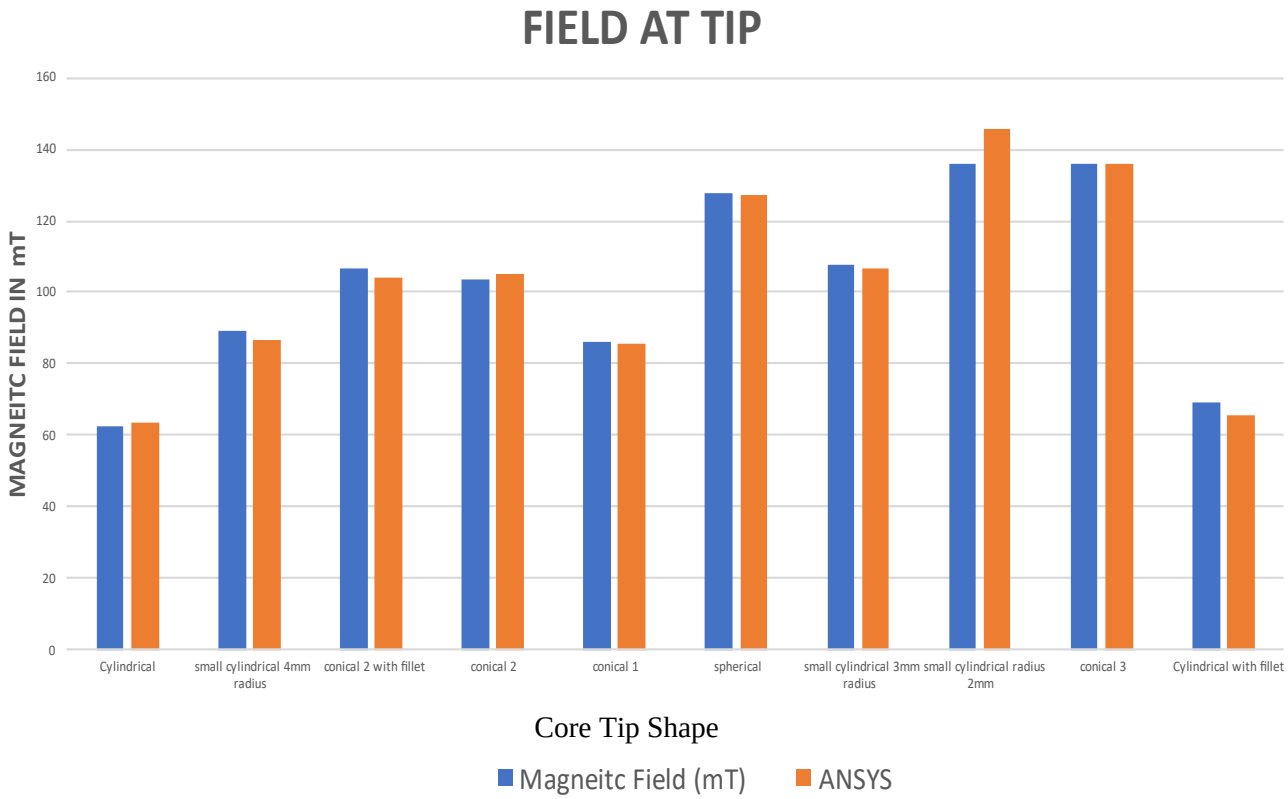

Figure 5.3 FEA and experimental comparison of magnetic field produced by different core tip shapes 5V

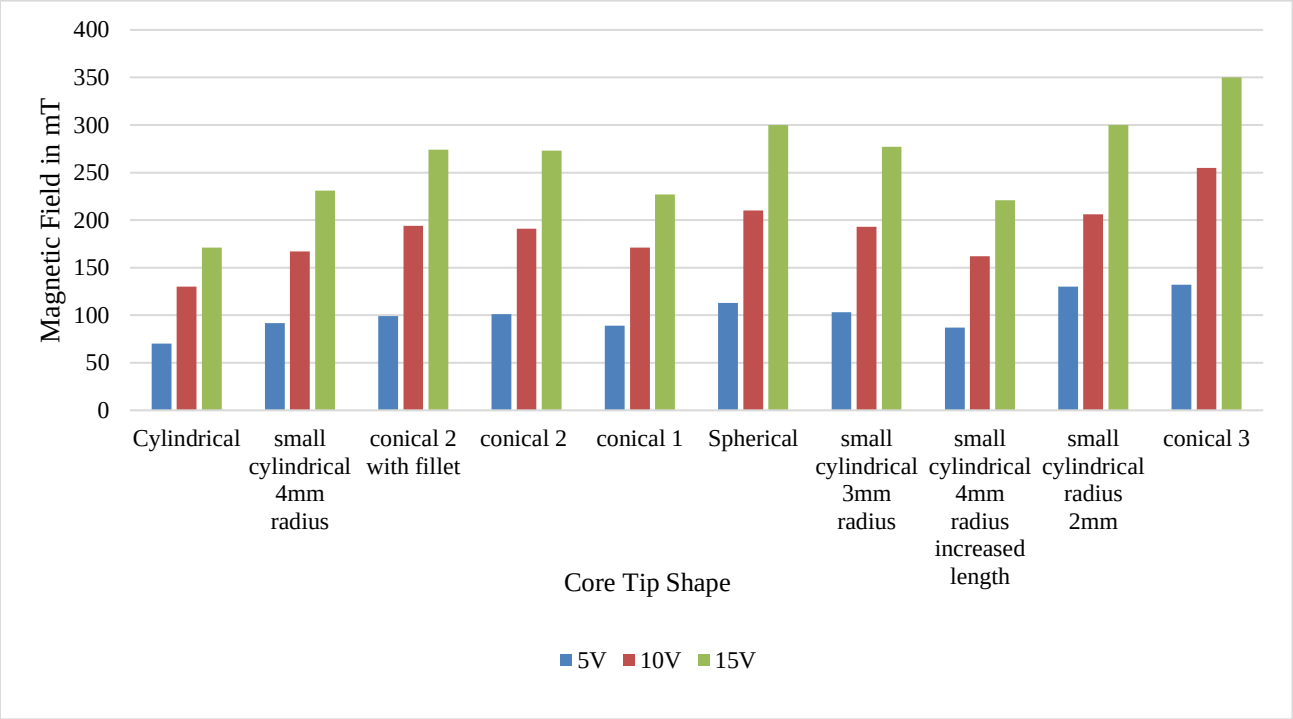

Figure 5.4 Effect of voltage levels on the magnetic field produced by different core tip shapes

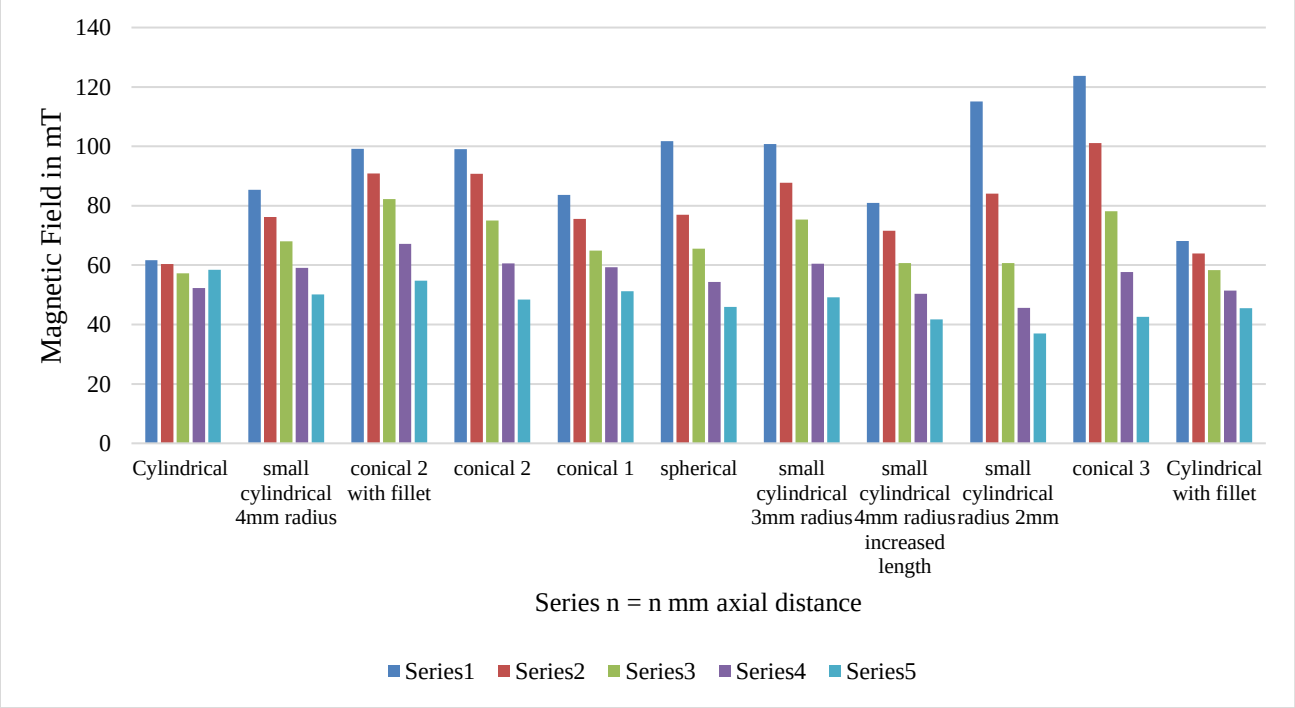

Figure 5.5 Magnetic Field on the axis of optimized taper coil - 5V

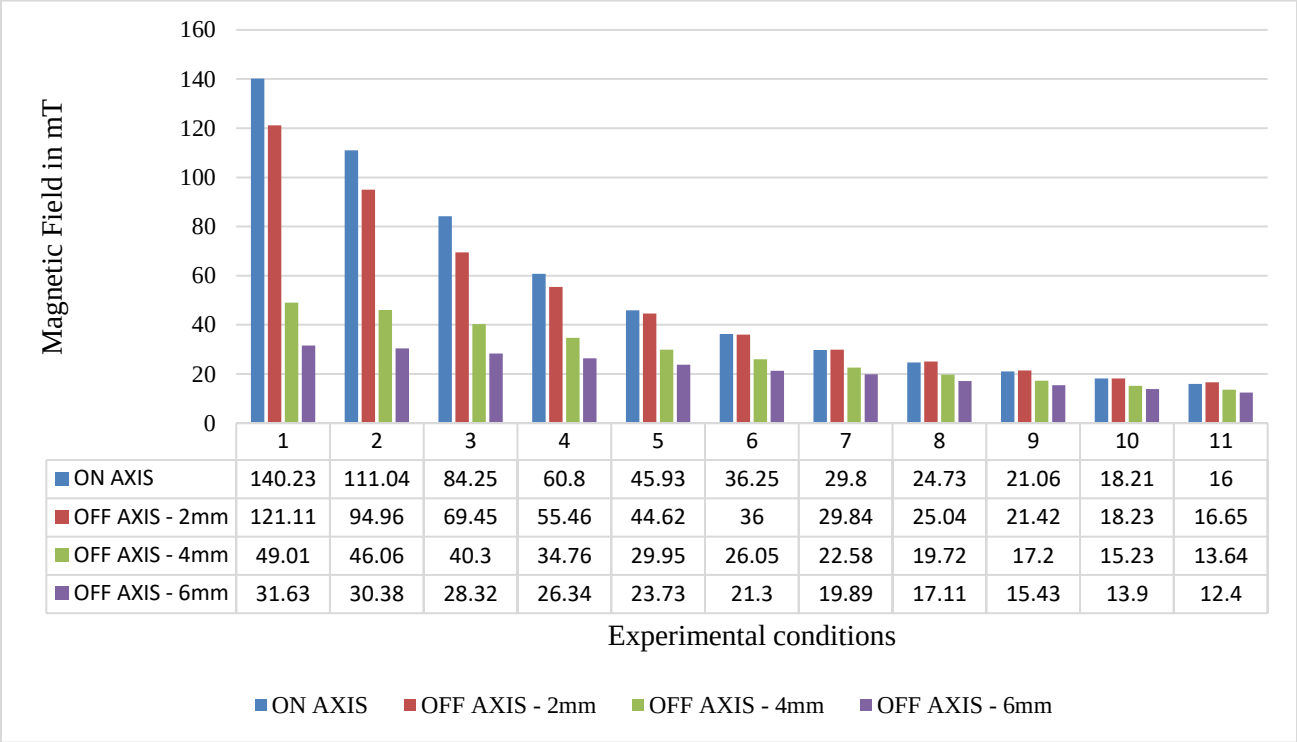

	1	2	3	4	5	6	7	8	9	10	11
ON AXIS	140.23	111.04	84.25	60.8	45.93	36.25	29.8	24.73	21.06	18.21	16
OFF AXIS - 2mm	121.11	94.96	69.45	55.46	44.62	36	29.84	25.04	21.42	18.23	16.65
OFF AXIS - 4mm	49.01	46.06	40.3	34.76	29.95	26.05	22.58	19.72	17.2	15.23	13.64
OFF AXIS - 6mm	31.63	30.38	28.32	26.34	23.73	21.3	19.89	17.11	15.43	13.9	12.4

Figure 5.6 Off-axis magnetic fields due to conical 3 tip shape - 5V

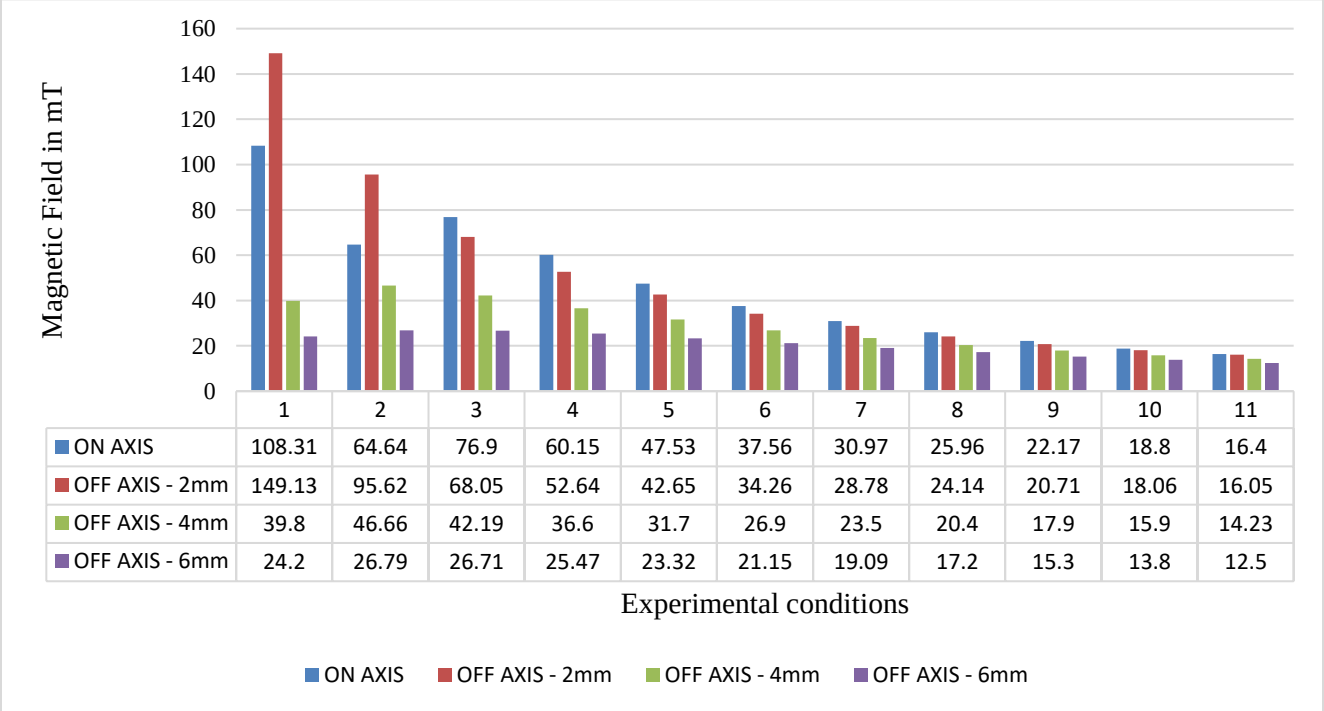

	1	2	3	4	5	6	7	8	9	10	11
ON AXIS	108.31	64.64	76.9	60.15	47.53	37.56	30.97	25.96	22.17	18.8	16.4
OFF AXIS - 2mm	149.13	95.62	68.05	52.64	42.65	34.26	28.78	24.14	20.71	18.06	16.05
OFF AXIS - 4mm	39.8	46.66	42.19	36.6	31.7	26.9	23.5	20.4	17.9	15.9	14.23
OFF AXIS - 6mm	24.2	26.79	26.71	25.47	23.32	21.15	19.09	17.2	15.3	13.8	12.5

Figure 5.7 Off-axis magnetic fields due to small cylindrical 3 tip shape - 5V

5.1.1 Experimental Measurement of Force

Since the force due to an electromagnet is directly proportional to the gradient of the magnetic field, it is equally important to validate the finite element force results with experimental values. A simple setup was created to measure the force using a precise weight scale. A pure iron cylindrical sample (6.4g; 11.51mm diameter, 7.95 mm length) was placed on a weight scale and force was then applied using an electromagnet placed coaxially with the iron specimen. The axial distance between sample and the core tip shape was varied using a micromanipulator. The finite element model was also modified to calculate the force on a 2D model of the same pure iron sample. Fig. 5.8 illustrates the setup for force measurement with a weight scale.

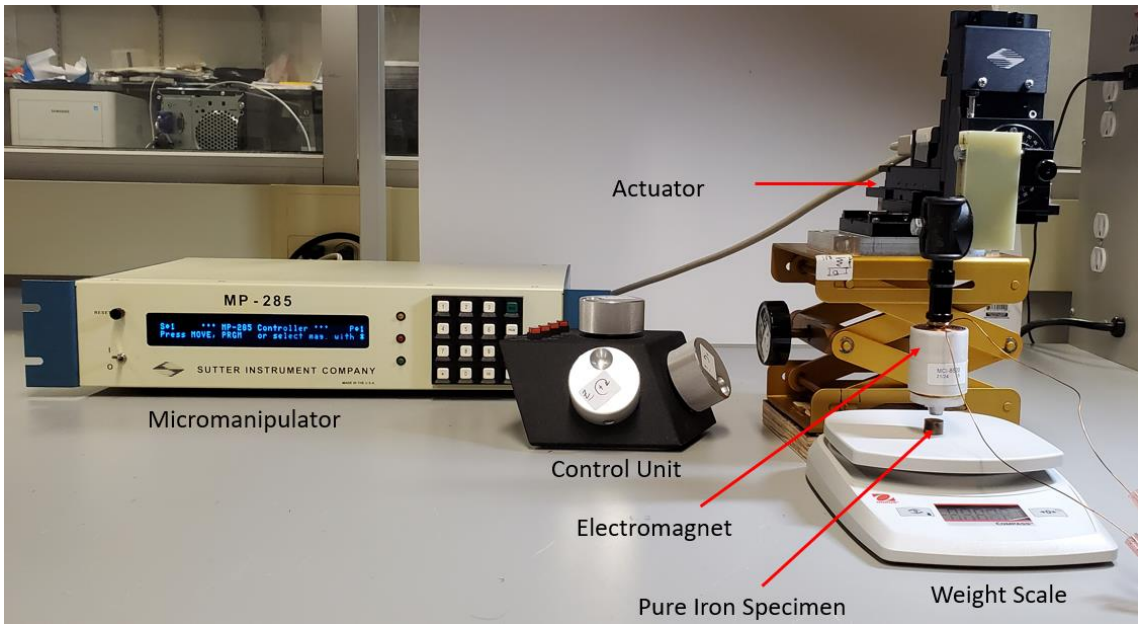

Figure 5.8 Experimental measurement of Lorentz force using a weight scale

It can be observed from Fig. 5.10 that the experimental measurements of force match closely with finite element models with an average error of 10%. The force measurements were also confirmed by a force and torque measurement sensor/load cell. It must be noted that the key objective of these experiments is to validate the results and efficiency of the finite element models. Once validated, the finite element

models are used for calculation of force and field at any point in the 3D space. Due to the attracting nature of magnetic force, the iron samples were only subjected to low current values. Fig. 5.9 illustrates the setup used for load cell measurements of force due the optimized electromagnet geometry.

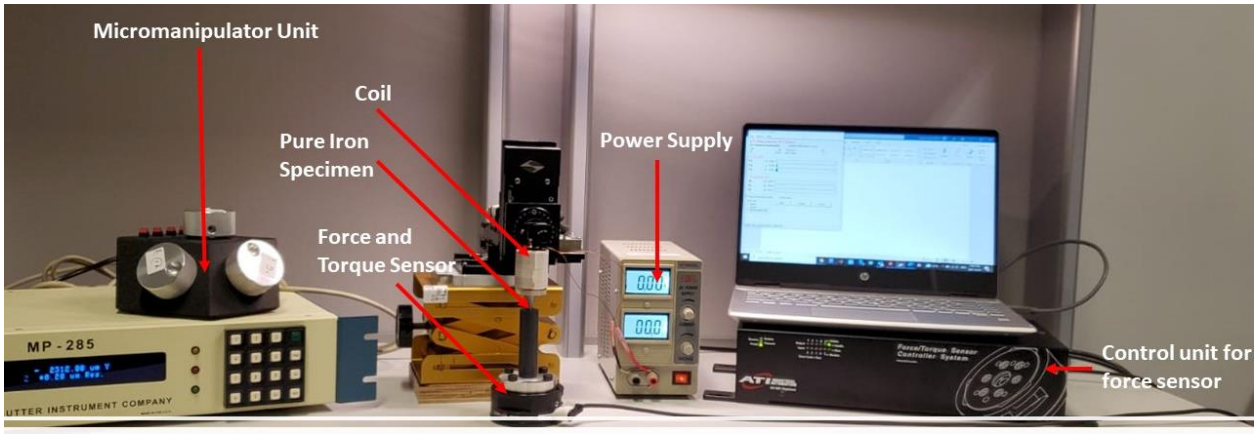

Figure 5.9 Experimental Measurement of Force using a Force and Torque Sensor

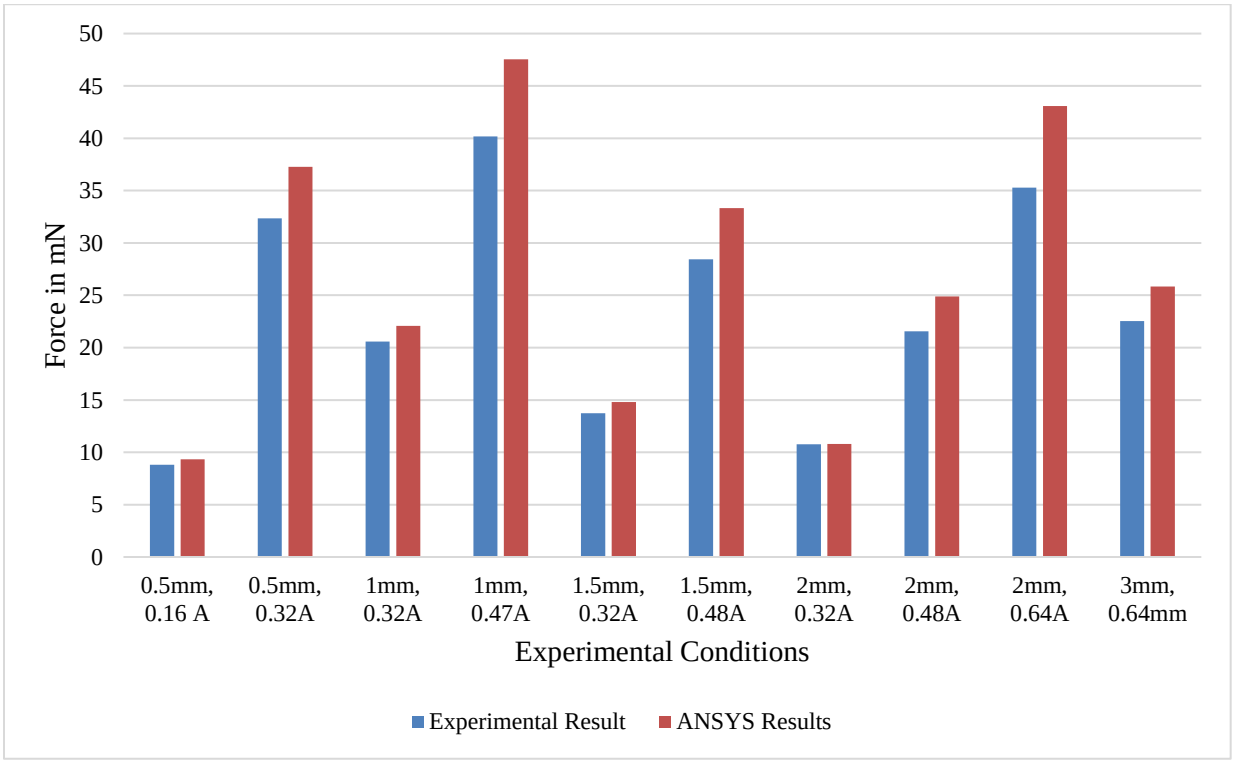

Figure 5.10 Experimental and FEA comparison of force

5.1.2 Temperature Measurement

The temperature of the coils is a limiting factor to the run time of the polishing apparatus. To operate the system in a safe temperature envelope, a Data Acquisition (DAQ) system was used to measure the temperature at various current amplitudes and frequencies. All coils are manufactured with a K type thermocouple attached to the outer surface of the windings. These thermocouples have a voltage variation of 41.276 µV/° C and provide an analog output proportional to the temperature of the coils. A data acquisition device with built in Cold Junction Compensation (CJC) was used to collect differential thermocouple measurements. CJC is required to compensate for additional thermal EMFs generated by thermocouple connection wires to the DAQ terminal block. It must be noted that the software (TracerDAQ) applies NIST linearization coefficient to linearize accurate temperature readings. Temperature measurements were recorded at 2.5hz data rate for 10 minutes or less to avoid permanent damage to the windings. The coils were energized using a combination of current and frequency as plotted in Fig. 5.12 to Fig. 5.16.

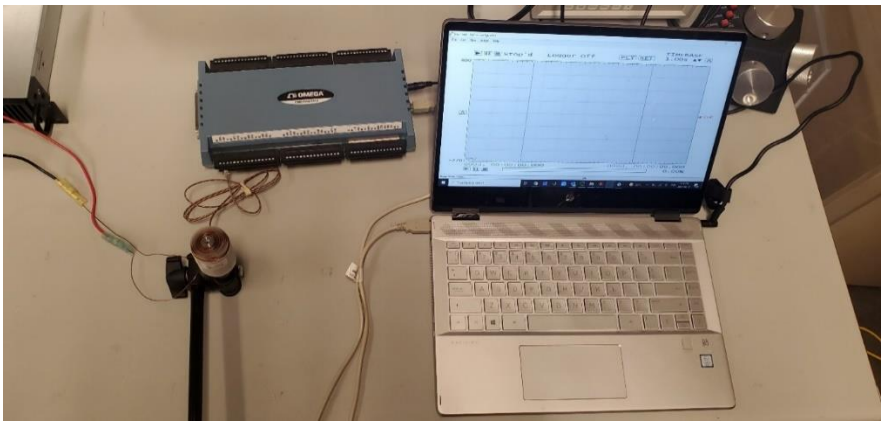

Figure 5.11 Coil temperature measurement setup

It was observed that the coils can safely operate under 3A without cooling and 4.5 A with cooling at an air flow of at least 7 cfm. 8 DC equipment cooling fans were integrated in the test platform to extend the cycle time of the system and hence assist in higher material removal rate.

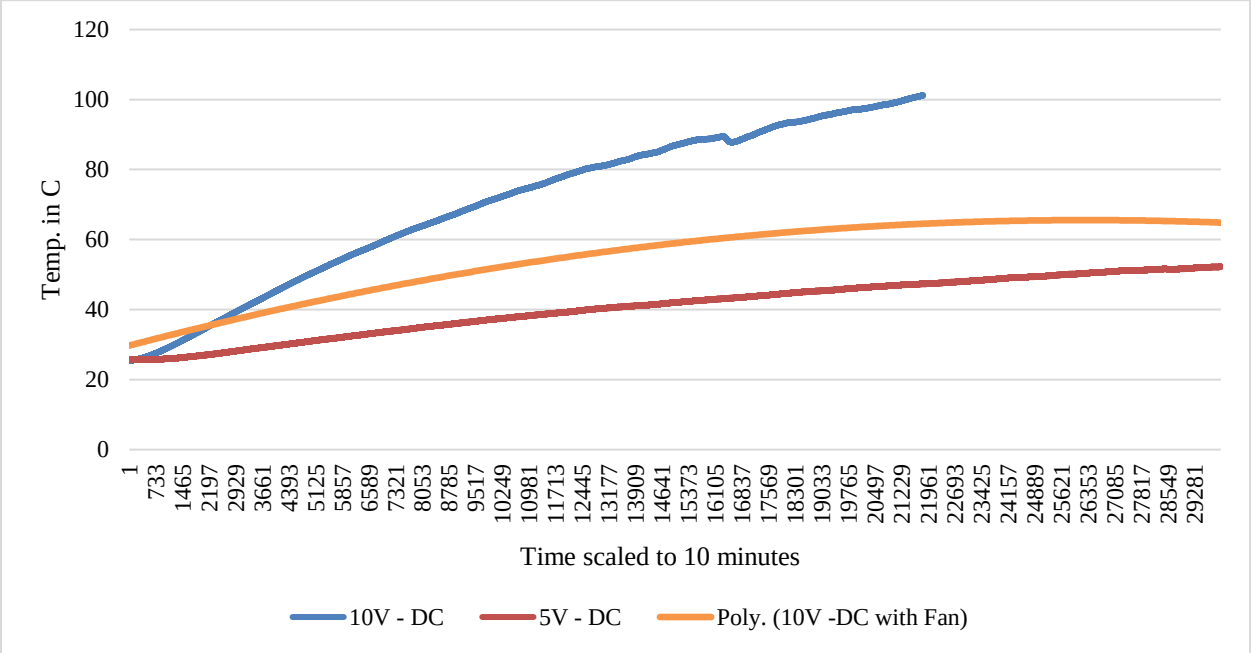

Figure 5.12 DC Temperature Measurements

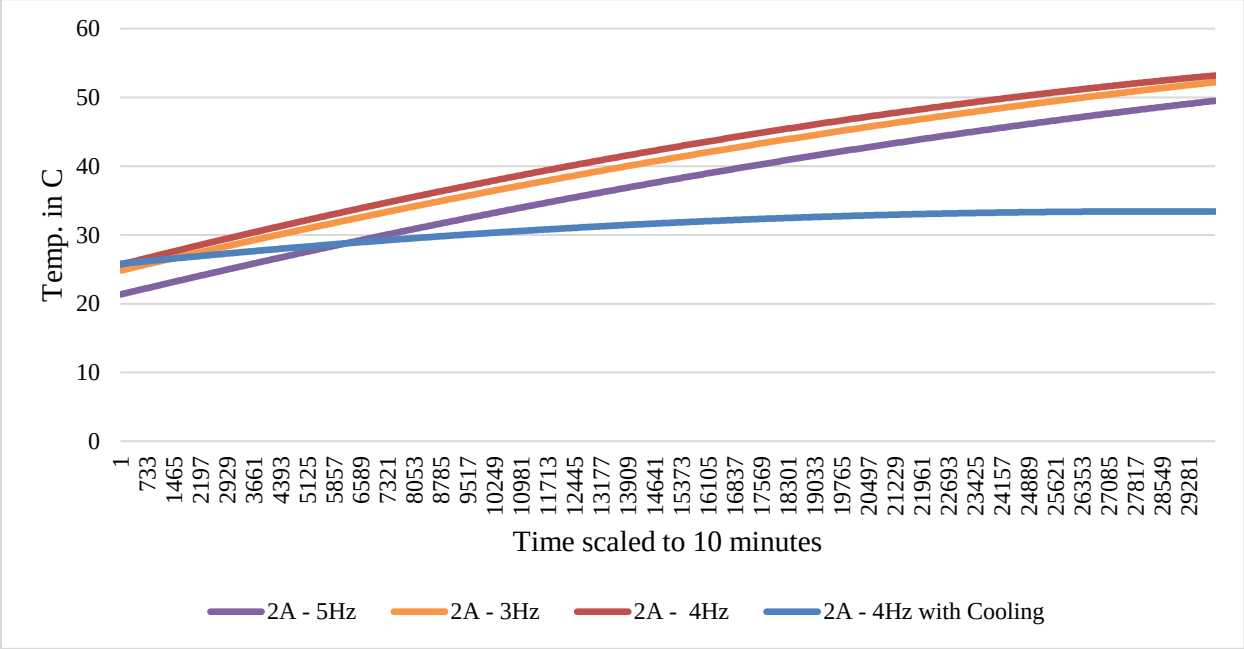

Figure 5.13 Temperature measurements at 2A

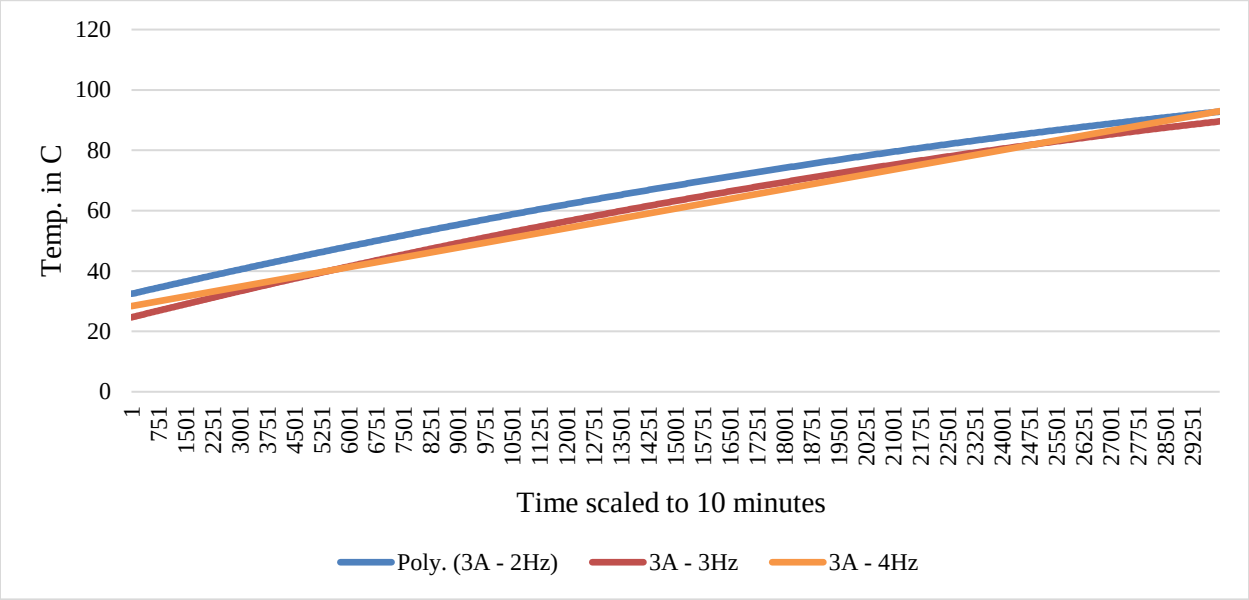

Figure 5.14 Temperature measurements at 3A

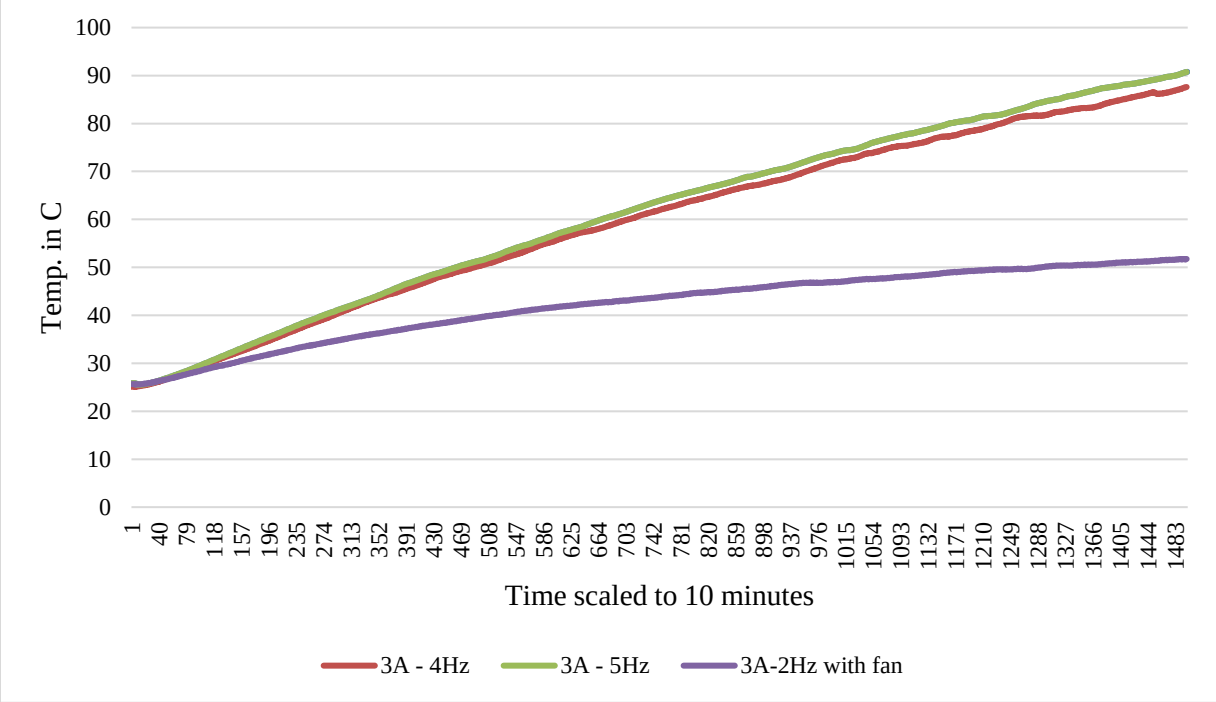

Figure 5.15 Temperature measurements at 3A

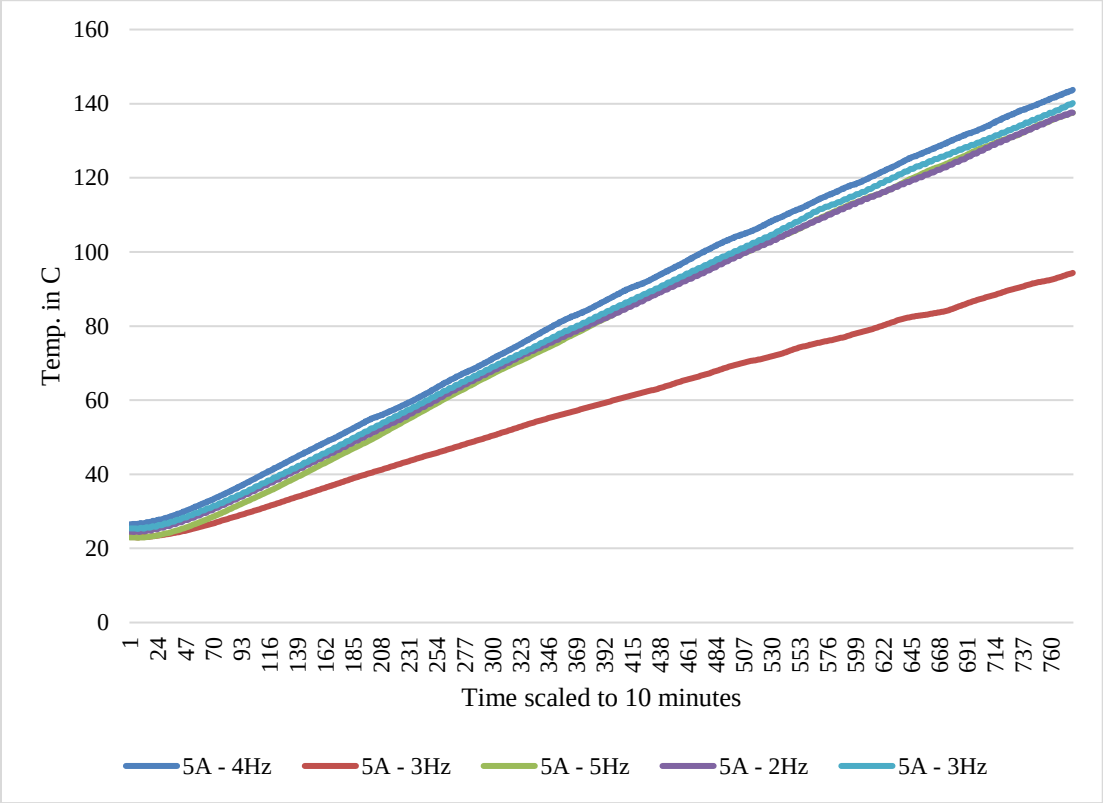

Figure 5.16 Temperature measurements at 5A

5.1.3 Evaluation of Particle Motion Through Steel Balls

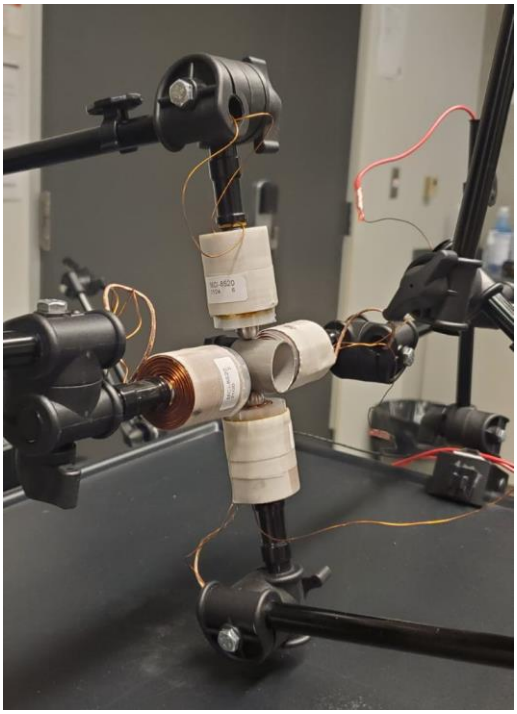

Figure 5.17 Horizontal orientation of a cylindrical specimen/workpiece

After confirming the performance of individual coils and calibrating the setup for various mechatronics sub-systems, various coil arrangements were implemented on a cylindrical specimen to observe the motion of particles under a rotating magnetic field. Cylindrical specimens were selected to avoid complexity. In cylindrical specimens, the coils are always horizontal/in the same plane and in physical contact with the outer surface of the specimen at equal angles. Flat sheet specimens, however, require adding a tilt to each coil and furthermore the distance between each coil can also be varied depending on the size of the specimen. To correctly visualize the motion of the particles, small steel balls of different diameters (2mm, 3mm and 4mm) were subjected to RMF. It was observed that the steel balls exhibit a circular motion on the inside surface of the specimen when 6 coils are implemented, and a diamond motion is exhibited when 4 coils were used. Circular motion is desirable to achieve uniform

material removal, as the diamond motion will only result in spot reduction of material at the tip of the cores. In addition, it was also observed that the 2mm steel ball tracked better circular motion as compared to 3mm and 4mm steel balls. The above observations were made with slow-motion videos recordings.

5.2 Implementation of Magnetic Field Assisted Abrasive Polishing

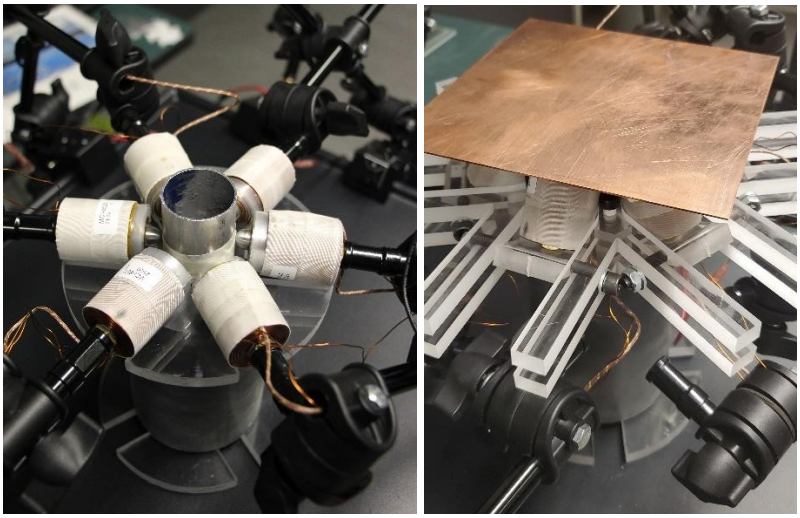

(a) (b)

Figure 5.18 Implementation of the polishing technique on (a) cylindrical specimen and (b) flat sheet specimens

After testing the performance of the system and sub-systems, the apparatus was implemented on a variety of specimens sizes and shapes. The polishing technique was implemented on aluminum specimens by primarily controlling three input variables: cycle time, frequency and current. Magnetic Abrasive Particles were synthesized using a variable ratio of iron powder to abrasive powder during an individual test run. Six different types of abrasive particles and a 325-mesh size of iron particles were used. The quantity of the iron powder was varied from a minimum of 30% to 55% using an accurate

weight scale. The following tables illustrates the different types of abrasives and specimens used in the experimental trials.

Figure 5.19 Abrasive Powder

Table 5 Abrasive powder types

Abrasive	**Size (microns)**	**Grit Size**
Aluminum Oxide	100	120 (smooth)
Aluminum Oxide	85	150 (smooth)
Aluminum Oxide	35	320 (extra smooth)
Diamond	20	500 (polished)
Silicon Carbide	100	120 (smooth)
Silicon Carbide	165	80 (rough)

Table 6 Specimen Characteristics

Material	Shape	Thickness	OD	ID	Yield Strength (psi)	Hardness
Multipurpose 6061 Aluminum	Sheet	0.080"	NA	NA	35,000	Brinell 95
Multipurpose 6061 Aluminum	Sheet	0.040"	NA	NA	35,000	Brinell 95
Multipurpose 6061 Aluminum	Round Tube	0.049"	2"	1.902"	35,000	Brinell 95
Multipurpose 6061 Aluminum	Round Tube	0.035"	1"	0.93"	35,000	Brinell 95
Multipurpose 6061 Aluminum	Round Tube	0.049"	1 1/2"	1.402"	35,000	Brinell 95

To evaluate the performance of the polishing technique, the surface roughness of the specimens was measured under a laser confocal microscope before and after polishing. The microscope used for this application is a 3D Laser Scanning Microscope – VK-250. Laser microscopes can perform non-contact profile, roughness, and film thickness measurements with nanometer-level resolution on any material or shape. The microscope combines white light with a laser light to collect both optical images and high-resolution surface details of the specimens [34] . Flat sheet specimens can be directly placed under the microscope, however, to scan a cylindrical specimen, small pieces of the polished part must be

placed under the lens to avoid damage to the lens due to contact with the curved surface. These pieces are prepared by cutting the specimen under a sheet metal foot shear. The change in surface roughness was measured by using the following equation:

$$\frac{r_o - r_a}{r_o} * 100$$

Where r_o is the initial surface roughness and r_a is the final average surface roughness after the polishing process has been implemented. The surface roughness of cylindrical aluminum samples (1.5" OD| 1.402" ID) reduced by a maximum of 93% (1.478 µm to 0.1017 µm) during a 45-minute cycle time. For flat sheet aluminum specimens, the surface roughness reduced by 54% (1.478 µm to 0.67 µm) during a 30-minute cycle time. Fig. 5.20 and Fig. 5.21 illustrate how the uneven contours on the samples were removed by the motion of the MAPs inside a cylindrical aluminum sample (1.5" OD| 1.402" ID). A uniform material removal was achieved due to autorotation of the cylindrical test specimen under the application of RMF with a clearance gap between the core tip shapes and the specimen outer surface. It must be noted that all surface roughness evaluations were performed for samples subjected to RMF generated by 6 coils.

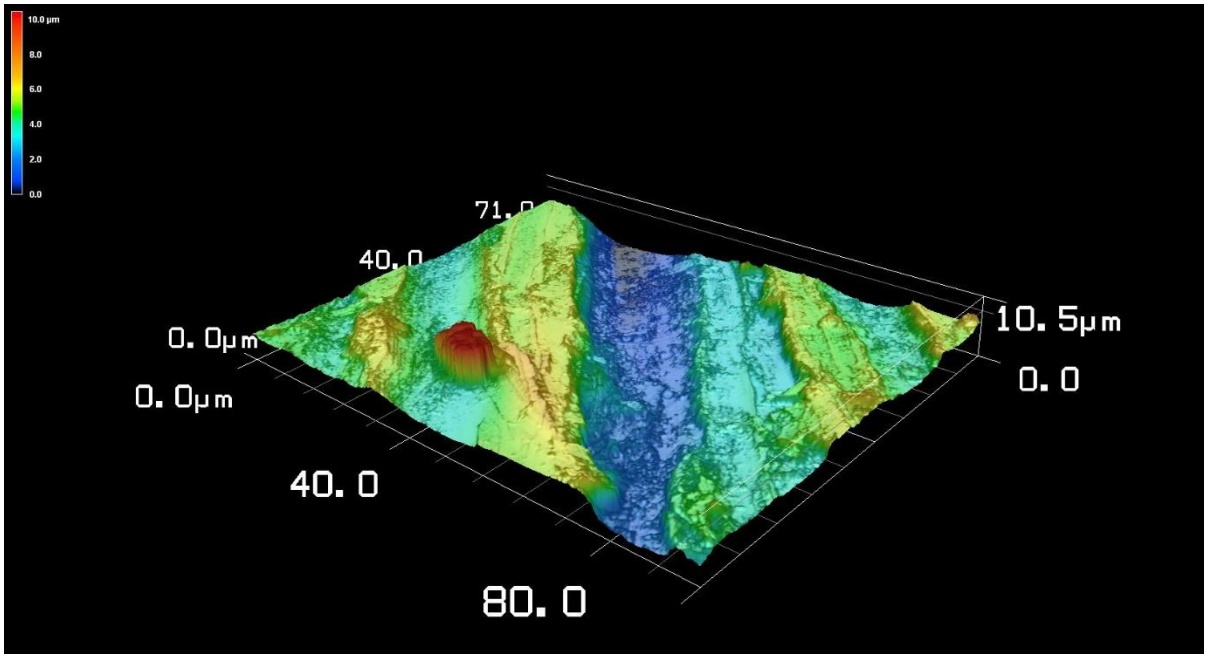

Figure 5.20 3D surface contour before polishing

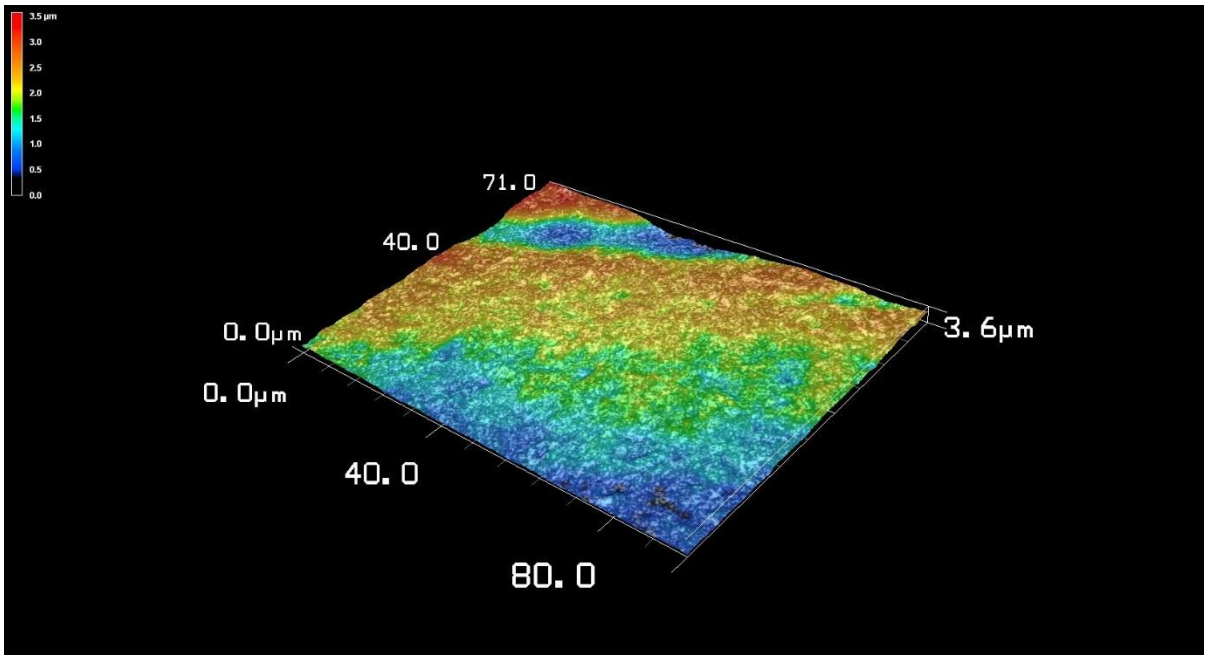

Figure 5.21 3D surface contour after polishing

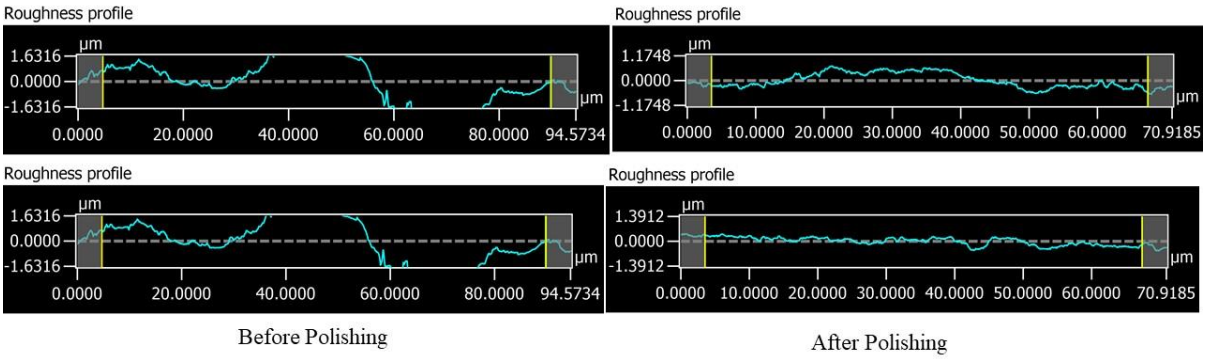

Before Polishing

After Polishing

Figure 5.22 Line surface profile before and after polishing

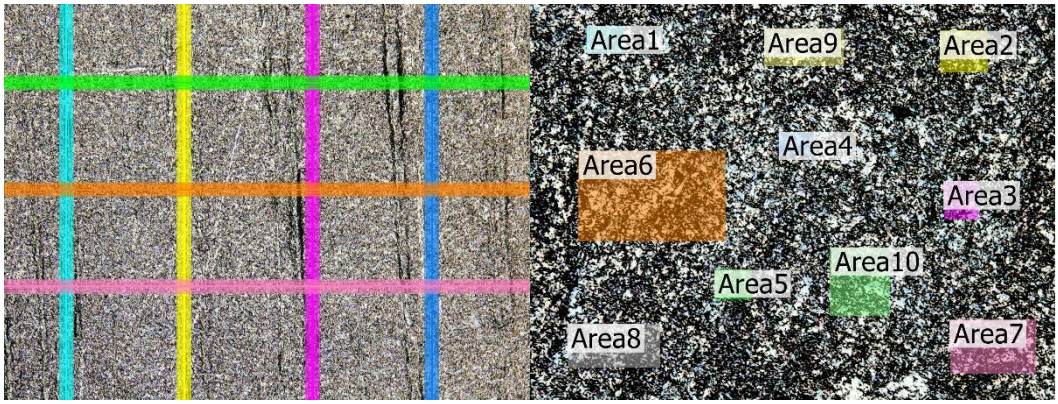

(a) (b)

Figure 5.23 Line (a) and area (b) measurement of surface roughness

To evaluate the reduction in surface roughness after polishing, a 150X lens was used to measure both line and area surface roughness at various locations (Fig. 5.23). Fig. 5.22 illustrates the surface profile of the specimen after polishing. It can be observed that the line surface profile is uniform and in the vicinities of an average surface roughness of 0.2 μm.

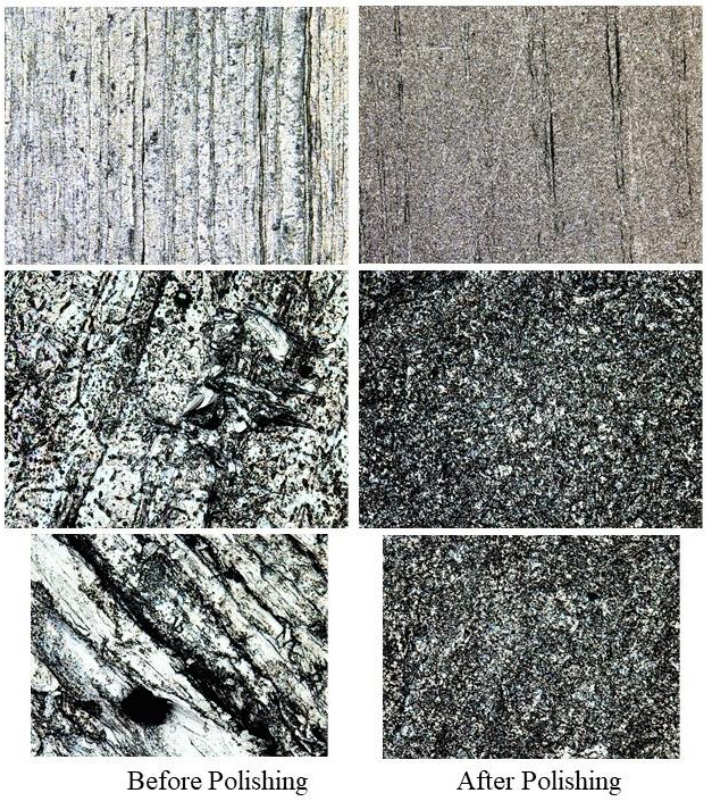

Figure 5.24 Optical microscope images of cylindrical aluminum specimens before and after polishing

Chapter 6
Conclusion and Future Work

6.1 Conclusion

The focus of this thesis was on the design, optimization, fabrication, integration, testing, implementation, and validation of Magnetic Field Assisted Abrasive Polishing using Stationary Electromagnets. A novel optimized electromagnet geometry was designed, fabricated and investigated for performance. This thesis contributed to the development of a novel polishing technique not only by addressing some of the current limitations in non-conventional finishing systems, but also by opening the way as a disruptive technology in the advent of new post processing trends in manufacturing. A full-scale prototype was designed for this purpose to reduce the average surface roughness of test specimens without the implementation of any rotating/translating machinery. This chapter summarizes the main conclusions and some of the future work proposed as a continuation to this thesis.

The system and technique developed in this thesis does not require any machinery to impart rotational or translational motion to the non-magnetic workpiece or the electromagnets to generate dynamic/rotating magnetic fields. The sub-systems are entirely stationary and developed on a wheeled platform that can be promptly transported to a suitable location.

A novel electromagnet geometry is designed and fabricated. The copper winding electromagnets are wound in a tapered shape to reduce the distance between adjacent electromagnets and introduce a greater number of electromagnets into the array as compared to conventional cylindrical electromagnets. The interchangeable/modular nature of pure iron core tip shapes allow the operator to direct the magnetic field lines based on the workpiece shape and material.

An open loop control model is configured to send analog and digital voltage command signals to the motor drives based on the stored executable instructions. The commands can be configured to alter the magnitude and speed of the rotating magnetic field. The control unit is further coupled with motor drives to adjust the magnetic flux density produced by each electromagnet by sending current waveforms emulating the voltage signals received from the control unit. Wherein the current waveforms are capable of altering at least one attribute comprising: strength of the magnetic field, rotation rate of the magnetic field, or direction of the magnetic field. MAPs follow the flux lines generated by a rotating magnetic field and comprise of two components: a magnetic component and an abrasive component. The magnetic component can be for example a powder of a magnetic material such as iron and the abrasive component can be the powder of a desired abrasive, such as diamond, silicon carbide (SiC) and aluminum oxide. The diameter of both the components can be varied based on the application and final surface roughness required. The results show that the motion of the MAPs appear to be valid and were therefore implemented on various test specimens.

Overall, it was established that the newly developed system could potentially eliminate the requirement of rotating machinery in conventional Magnetic Abrasive Finishing. Therefore, the work described in this thesis shows how a stationary electromagnet array can potentially overcome the limitations of conventional magnetic abrasive finishing and other precision polishing techniques.

6.2 Recommendations and Future Work

The investigations described in this dissertation are intended to establish the framework for further optimization of process parameters pertinent to the mechatronic modules integrated in the developed surface polishing system. The intended vision for this system would be to achieve a commercially ready and user-friendly polishing apparatus that addresses the emerging need for post processing of machined

and additively manufacturing parts with controlled surface roughness and material removal rates. To achieve this goal, further research into hardware and software development should be performed. The following topics are recommended for future research endeavors:

- The surface roughness results discussed in chapter 5 were performed only on a limited number of specimens due to low availability of the laser scanning confocal microscope and COVID restrictions. Future research can focus on implementing the discussed technique on a variety of material types and shapes. This would enable the researcher to develop an accurate prediction model for the final surface roughness/change in surface roughness of the workpiece.

- Adding to the first point, secondary process parameters, such as core tip shape, angle of inclination, material hardness, relative distance and working gap can also be incorporated in the predictive model for a more comprehensive evaluation and accurate results.

- A future research endeavor can also replace the power supply, simulator, motor drives and the power distribution stage by a single robust unit called the auxiliary control unit as discussed in chapter 4 to develop a more robust and small size apparatus.

- The current control models are open loop in nature and implement no feedback. Since the end result of this technique (surface roughness measured under a laser confocal microscope) cannot be a real time feedback, hall sensors and motion feedback cameras can be used to develop and tune an adaptive control model in the future.

References

[1] H. Greenslet, "System and method of magnetic abrasive surface processing". US Patent US9579766B2, 28 February 2012.

[2] H. Y. Pei-Ying Wu, "Material Removal Mechanism of Additively Manufactured Components Finished using Magnetic Abrasive Finishing," *Procedia Manufacturing,* vol. 26, pp. 394-402, 2018.

[3] M. B. K. Thamir Al-Dulaimi, "A stationary apparatus of magnetic abrasive finishing using a rotating magnetic field," *Microsystem Technologies,* vol. 23, no. 11, 2017.

[4] L.-D. Y. H.-M. C. Ching-Tien Lin, "Study of magnetic abrasive finishing in free-form surface," *The International Journal of Advanced Manufacturing Technology,* vol. 34, no. 1, pp. 122-130, 2007.

[5] T. Al-Dulaimi, "Design and Implementation of a Stationary Magnetic Abrasive Finishing Apparatus," 2018.

[6] N. S. K. P. D. A. S. KanishT C, "Experimental Investigations on Magnetic Field Assisted Abrasive Finishing of SS 316L," *Procedia Manufacturing,* vol. 30, pp. 276-283, 2019.

[7] J. A. C. a. H. W. Zhang, "Surface quality and material removal in magnetic abrasive finishing of selective laser melted 316L stainless steel," *Journal of Manufacturing Processes,* vol. 45, pp. 710-719, 2019.

[8] K. H. A. C.-N. S. M. H. G. C. W. K. K. L. J. W. H. S. R. K. Jiang Guo, "Novel rotating-vibrating magnetic abrasive polishing method for double-layered internal surface finishing," *Journal of Materials Processing Technology,* vol. 264, pp. 422-437, 2019.

[9] R. S. M. &. P. M. Pandey, "Magnetic abrasive finishing of hardened AISI 52100 steel," *The International Journal of Advanced Manufacturing Technology ,* vol. 55, p. 501–515, December 2010.

[10] D. K. S. .. V. K. J. .. V. Raghuram, "Experimental investigations into forces acting during a magnetic," *The International Journal of Advanced Manufacturing Technology,* vol. 30, no. 7-8, pp. 652-662, 2006.

[11] B. H. S. C. Y. C. &. Z. Y. ZhengHao Yu, "Study on the inner surface finishing of irregular spatial elbow pipe by the centerline reconstruction," *The International Journal of Advanced Manufacturing Technology ,* vol. 93, p. 3085–3093, 2017.

[12] T. E. H. a. K. T. SHINMURA, "The development of magnetic-abrasive finishing and its equipment by applying a rotating magnetic field," *Bulletin of JSME,* vol. 29, pp. 4437-4443, 1986.

[13] A. a. V. K. J. Sidpara, "Analysis of forces on the freeform surface in magnetorheological fluid based finishing process," *International Journal of Machine Tools and Manufacture,* vol. 69, pp. 1-10, 2013.

[14] C. Y. S. H. H. ,. J. H. S. a. S. D. M. Lida Heng, "Development of a New Ultra-High-Precision Magnetic Abrasive Finishing for Wire Material Using a Rotating Magnetic Field," *Materials,* vol. 12, no. 2, p. 312, 2019.

[15] K.-L. W. J.-H. J. Y.-H. T. &. B.-H. Y. Yi-Hsun Lee, "Two-dimensional vibration-assisted magnetic abrasive finishing of stainless steel SUS304," *The International Journal of Advanced Manufacturing Technology,* vol. 69, no. December 2013, p. 2723–2733, 2013.

[16] T. S. Hitomi Yamaguchi, "Study of the surface modification resulting from an internal magnetic abrasive finishing process," *WEAR,* pp. 246-255, 1999.

[17] D. T. S. a. H. Y. Wang, ""Study of magnetic field assisted mechanochemical polishing process for inner surface of Si3N4 ceramic components: finishing characteristics under wet finishing using distilled water," *International Journal of Machine Tools and Manufacture,* vol. 44, no. 14, pp. 1547-1553, 2004.

[18] Y. M. a. D. C. J. A. E. Umenei, "Analytic Solution for Variations of Magnetic Fields in Closed Circuits: Examination of Deviations From the “Standard” Ampere’s Law Equation," *IEEE TRANSACTIONS ON MAGNETICS,* vol. 47, no. 4, 2011.

[19] T. A. Lipo, "Magnetic Circuits," in *Introduction to AC Machine Design,* Wiley-IEEE Press, 2018, pp. 1-50.

[20] D. P. D. a. P. J. W. B. ©. S.-b. L. P. D. a. J. B. Dr. Sen-ben Liao, " Physics 8.02 Electricity and Magnetism at MIT," 2004.

[21] D. E. a. J. N. S. Mapother, "The axial variation of the magnetic field in solenoids of finite thickness," Engineering Experiment Station. University of Illinois at Urbana-Champaign, 1955.

[22] S. Yang and J. C. Ordonez, "Concurrent Solenoid Design Optimization From Thermal and Electromagnetic Standpoints," *IEEE Transactions on Applied Superconductivity,* vol. 26, no. 4, pp. 1-5, 2016.

[23] S. Y. a. J. C. Ordonez, "Concurrent Solenoid Design Optimization From Thermal and Electromagnetic Standpoints," *IEEE TRANSACTIONS ON APPLIED SUPERCONDUCTIVITY,* vol. 26, no. 4, 2016.

[24] J. OD, Electricity and magnetism, New York: Appleton-Century-crofts, 1966.

[25] R. S. a. P. M. P. Mulik, "Experimental investigations and modeling of finishing force and torque in ultrasonic assisted magnetic abrasive finishing," *Journal of manufacturing science and engineering,* vol. 134, no. 5, 2012.

[26] O. B. Abbott JJ, "Optimization of coreless electromagnets to maximize field generation for magnetic manipulation systems," *IEEE Magnetics Letters,* vol. 9, pp. 1-4, 2017.

[27] M. C. a. A. D. Moshe Stern, "Configuration and Design of Electromagnets for Rapid and Precise Manipulation of Magnetic Beads in Biosensing Applications," *Micromachines,* vol. 10, no. 11, p. 784, 2019.

[28] S. Tumanski, "Induction coil sensors—A review," *Measurement Science and Technology, 18(3), R31.*, vol. 18, no. 3, p. R31, 2007.

[29] F. D. Graham, Audels Engineers and Mechanics Guide, 1921.

[30] H.-U. S. Y. B. Kyo-Beum Lee, "Basic Control of AC Motor Drives," in *Control of Power Electronic Converters and Systems*, Elsevier Inc. , 2018, pp. 301-329.

[31] S. C. P. S. a. C. V. K. Hausmair, "Aliasing-free digital pulse-width modulation for burst-mode RF transmitters," *IEEE Transactions on Circuits and Systems I: Regular Papers,* vol. 60, no. 2, pp. 415-427, 2013.

[32] CharlesTsai, "Sine Wave Generation Using PWM With Hercules™ N2HET," May 2015. [Online]. Available: https://www.ti.com/lit/an/spna217/spna217.pdf?ts=1626531360621&ref_url=https%253A%252F%252Fwww.google.com%252F#:~:text=By%20time%2Dvarying%20the%20duty,digitized%20over%2012%20sample%20points. [Accessed 5 January 2021].

[33] L. N. Mulay, Magnetic susceptibility, New York: Interscience Publishers , 1963.

[34] "Profile-analyzing Laser Microscope," Keyence, [Online]. Available: https://www.keyence.com/landing/microscope/lp_vk250_micro.jsp. [Accessed April 2021].